OPEN ACCESS

Topical Review

Nano- and microparticles at fluid and biological interfaces

S Dasgupta[1,2,4], T Auth[3] and G Gompper[3]

[1] Mechanobiology Institute, National University of Singapore, Singapore 117411, Singapore
[2] Institut Curie, CNRS, UMR 168, 75005 Paris, France
[3] Theoretical Soft Matter and Biophysics, Institute of Complex Systems and Institute for Advanced Simulation, Forschungszentrum Jülich, 52425 Jülich, Germany
[4] Present address: Department of Physics, University of Toronto, Toronto, Ontario M5S1A7, Canada

E-mail: sabyadg.softbio@gmail.com, t.auth@fz-juelich.de and g.gompper@fz-juelich.de

CrossMark

Abstract

Systems with interfaces are abundant in both technological applications and biology. While a fluid interface separates two fluids, membranes separate the inside of vesicles from the outside, the interior of biological cells from the environment, and compartmentalize cells into organelles. The physical properties of interfaces are characterized by interface tension, those of membranes are characterized by bending and stretching elasticity. Amphiphilic molecules like surfactants that are added to a system with two immiscible fluids decrease the interface tension and induce a bending rigidity. Lipid bilayer membranes of vesicles can be stretched or compressed by osmotic pressure; in biological cells, also the presence of a cytoskeleton can induce membrane tension. If the thickness of the interface or the membrane is small compared with its lateral extension, both can be described using two-dimensional mathematical surfaces embedded in three-dimensional space. We review recent work on the interaction of particles with interfaces and membranes. This can be micrometer-sized particles at interfaces that stabilise emulsions or form colloidosomes, as well as typically nanometer-sized particles at membranes, such as viruses, parasites, and engineered drug delivery systems. In both cases, we first discuss the interaction of single particles with interfaces and membranes, e.g. particles in external fields, non-spherical particles, and particles at curved interfaces, followed by interface-mediated interaction between two particles, many-particle interactions, interface and membrane curvature-induced phenomena, and applications.

Keywords: membranes, nanoparticles, capillary interactions, lipid bilayers, emulsions, viruses, interfaces

(Some figures may appear in colour only in the online journal)

1. Introduction

Interfaces are present in all systems with two or more phases. This can be interfaces between fluid and gas phases, but also interfaces between immiscible fluids, such as oil and water, and interfaces between fluid and solid phases. Popular applications for particles at interfaces are Pickering emulsions and bijels [1–5]. Already in the early 20th century, particles have been found to assemble at interfaces and to stabilize emulsions [1, 3]. The stabilization depends on particle size, shape, softness, and surface heterogeneities, e.g. generated by functionalization.

Membranes are ubiquitous in biological cells. While the plasma membrane encloses the entire cell, membranes

also compartmentalize cells and thereby define organelles. Transmembrane transport is essential for the communication both inside a cell as well as of cells with their environment [6, 7]. The interaction of particles and pathogens with biological membranes—and therefore also their cellular uptake and intracellular transport—crucially depends on the particle size, shape, softness, and surface functionalization.

Nowadays a whole zoo of micro- and nanoparticles can be fabricated from various materials, with engineered shapes and surface functionalizations. The particles can be used for applications in food science [8–10], cosmetics [8, 9, 11], as antimicrobials [12, 13], and in nanomedicine [14–16]; therefore systematic studies and a careful consideration of potentially toxic effects are required [17–21]. Figure 1 shows examples for oblate, bullet-shaped, pill-shaped, and dumbbell-shaped microparticles that are made from a polymeric material. Figure 2 shows cube-like, rod-like, irregularly-shaped, and spindle-like metal and metal-oxide nanoparticles. All these particles can also be considered as model systems for 'particles' found in nature. For example, the malaria parasite is micrometer-sized and has an egg-like shape [22, 23]. Milk contains casein micelles with sizes below 100 nm that stabilize fat globules [24]. Viruses resemble roundish, filament-like, and bullet shapes with sizes below 100 nm [25–27]; in particular, the filamentous Ebola and Marburg viruses are of much interest due to their enhanced virulence that leads to high mortality rates [28, 29].

Fluid interfaces are rough on the molecular scale and can be analytically well described by a hyperbolic tangent-shaped density profile [31, 33], see figure 3. However, the typical interface width is much smaller than the sizes of the particles that we consider. In order to study the interaction of particles with interfaces, the interface can therefore be thought of as mathematical surface with its physical properties characterized by an interface tension.

Lipid-bilayer membranes often consist of many components, e.g. different lipids and cholesterol, and biological membranes usually also contain membrane proteins. This can lead to phase separation within the membrane, as shown in figure 4. The typical thickness of a lipid bilayer membrane is $d \approx 4$ nm and cannot be neglected for small nanoparticles with sizes of few nanometers. For nanoparticles with radii of 10 nm and above, the membrane can be described as mathematical surface with curvature-elastic properties.

The possiblity to model both fluid interfaces and biological interfaces (membranes) using mathematical surfaces is our motivation for discussing particles at interfaces and at membranes in a single review article. For biological interfaces, we will focus on sufficiently large particles for which a continuum model is not only feasible, but also more appropriate than an atomistic model. The deformation energy of the surface can then be calculated using the Helfrich Hamiltonian [34],

$$\mathcal{H} = \int_S \mathrm{d}S \left[\gamma + 2\kappa(H - c_0)^2 + \bar{\kappa} K \right]. \quad (1)$$

Here, the interface conformation is characterized by the two principal curvatures at each point of the interface, c_1 and c_2, that enter the Hamiltonian via the mean curvature $H = (c_1 + c_2)/2$

and the Gaussian curvature $K = c_1 c_2$. The total deformation energy is obtained by integration over the entire interface area S. Tension γ, bending rigidity κ, spontaneous curvature c_0, and Gaussian saddle splay modulus $\bar{\kappa}$ describe the mechanical and elastic properties of the interface. Equation (1) applies to biological interfaces if the bending energy contribution dominates, and to fluid interfaces if the energy is given only by the tension term.

For spherical particles at planar fluid interfaces, the particle size, the interface tensions between the particles and the two phases, as well as the interface tension between both phases characterize the system. If the interface tensions between the particles and both phases are identical, the particles attach to the interface because their presence reduces direct contact between both phases without any additional costs for the contact of the particles with the fluids. For high-tension interfaces and micrometer-sized particles, such as for silica particles at oil–water interfaces, the attachment energy gain can be as high as $10^7 \, k_B T$ [41]. Therefore, such particles are irreversibly adsorbed to the interface. If the interface tensions of the particles with both fluids differ, the attachment energies of the particles can be strongly reduced.

For particles attached to membranes, the membrane elastic properties in equation (1) and the adhesion energy between particles and membranes

$$\mathcal{E}_{\mathrm{ad}} = -w \int_{S_{\mathrm{ad}}} \mathrm{d}S \quad (2)$$

characterize the system. Here, S_{ad} is the membrane area adhered to the particle, and the adhesion strength w for the contact interaction can be mediated by van der Waals forces, by electrostatic interactions, and by specific adhesion (receptor-ligand bonds). For small spherical particles attached to nearly planar membranes and weak adhesion strengths, wrapping may not be energetically favourable, while for spherical particles with a radius of 50 nm and for a high adhesion strength $w = 0.2 \, k_B T \, \mathrm{nm}^{-2}$ the energy gain through wrapping can be as high as $5000 \, k_B T$. Particle shape can strongly alter the attachment energy.

Table 1 provides an overview of typical attachment energies of spherical particles to interfaces and membranes. For particles at interfaces, we assume that they have equal interface tensions with both fluid phases and that they are therefore half immersed in each phase. For particles at membranes, we assume that they are attached to a membrane with half of their surface area and that there is no deformation energy cost for the membrane surrounding the particles[5].

Interface deformations induced by particles lead to interface-mediated interactions and self-assembly; many-particle systems minimize the deformation energies also with respect to the particle positions. For example, capillary forces between micrometer-sized ellipsoidal particles increase with increasing aspect ratio and the energy gain at particle contact can be as high as 10^4–$10^5 \, k_B T$ already for ellipsoid aspect ratios of 2–3 [43, 45]. Membrane-mediated binding energies of few

---

[5] Our estimates are based on the overview of adhesion strengths provided in [42].
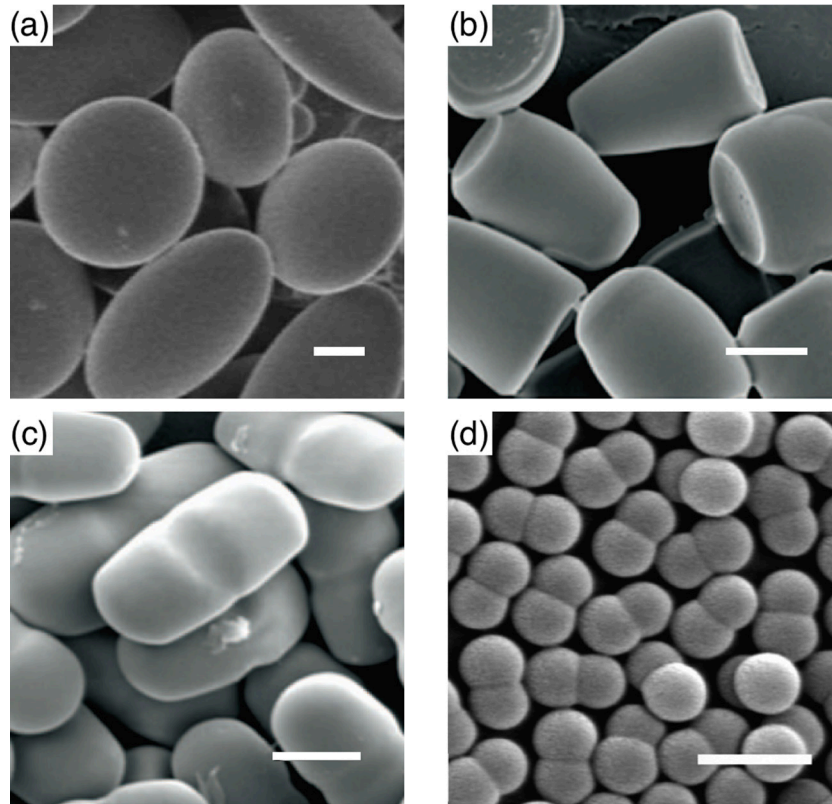
Figure 1. Examples for microparticles: (a) oblate, disk-shaped, (b) bullet-shaped, and (c) pill-shaped polymeric particles. The length of the scale bars corresponds to 2 μm. Adapted with permission from [25]. Copyright © 2007 National Academy of Sciences. (d) Dumbbell-shaped polymeric particles. The length of the scale bar corresponds to 0.5 μm. Adapted with permission from [26]. Copyright © 2010 American Chemical Society.

$k_\mathrm{B}T$ have been calculated for spherical particles at membranes [44, 46, 47][6]. Table 2 provides an overview of interface-mediated and membrane-mediated bond energies for particles at contact.

Structures on the micrometer scale can readily be observed using light microscopy. In order to access the nanometer scale, more sophisticated techniques, such as electron microscopy or super-resolution microscopy, have to be employed [49–54]. Whereas Ramsden and Pickering have reported on particle-stabilised emulsions already in the early 20th century [1, 3], images of nanoparticles, such as bacteriophages, have only been reported in 1940s, soon after electron microscopy has become available [55]. Since the very early studies of particles at fluid and biological interfaces, observation techniques and abilities to engineer particles have continuously advanced. Besides these experimental developments, also mesoscopic and atomistic modeling and computer simulation techniques and speed have rapidly developed. Both allows the characterization of particles at interfaces with increasing accuracy; this review article provides an overview of recent achievements. For both fluid and biological interfaces, we will discuss similar aspects: attachment to the interface, mechanisms for deforming the interface, particle orientation at the interface for nonspherical particles, long-range and short-range interactions, many-particle interactions,

and applications. Many concepts can easily be transferred between systems with fluid and with biological interfaces. We stress this parallelity by the analogous structure of the sections for both systems. Section 2 is devoted to particles at fluid interfaces, section 3 to particles at biological membranes. The overview of the experimental studies of self-assembly of microparticles at fluid interfaces may not only benefit scientists investigating such systems, but also those interested in nanoparticles at biological membranes, where systems are less accessible experimentally and fewer studies are therefore available.

2. Particles at fluid interfaces

Particles adsorb at fluid interfaces because they reduce the interface area and thereby also the total interface energy. Here, we have to account for the interface energies between the three phases, liquid ℓ, vapor (or a second liquid) v, and solid s. The system can be characterized by the three interface tensions γ_{sv}, $\gamma_{\ell v}$, and $\gamma_{s\ell}$, see figure 5. The force balance at the contact line, where the liquid-vapor interface is located at the particle, is given by the Young–Dupré equation,

$$\gamma_{sv} = \gamma_{\ell v} \cos \theta_\mathrm{c} + \gamma_{s\ell}, \qquad (3)$$

which defines the contact angle θ_c, see figure 5. The energy difference to bring a spherical particle with radius a from the bulk phase to the interface is the trapping energy [56]

---

[6] Contrary to particles, for spherical-cap inclusions at membranes only metastable bound states have been reported [48].
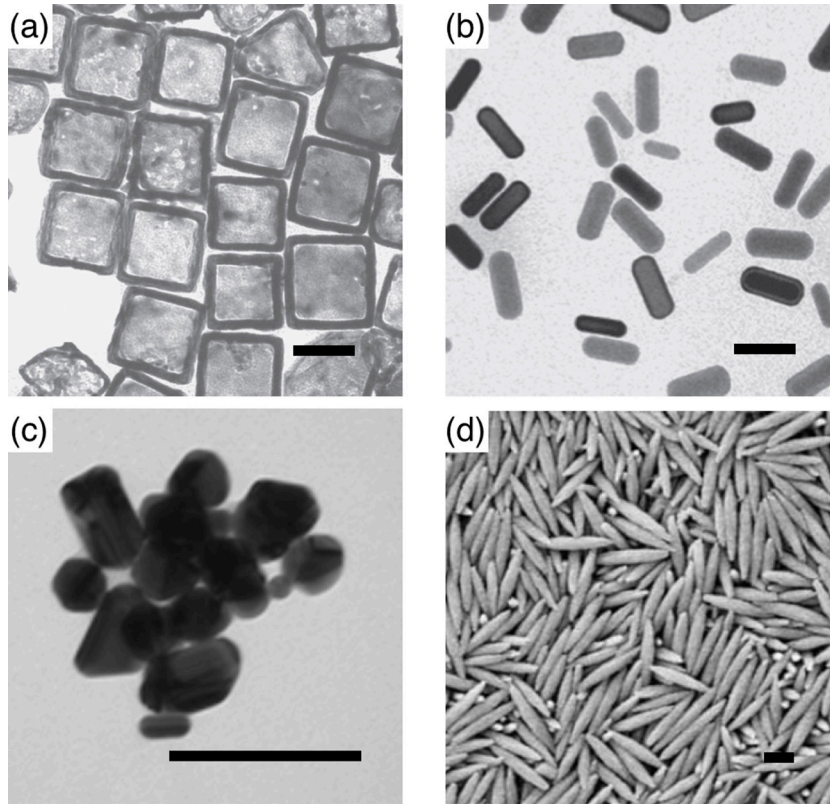
Figure 2. Examples for nanoparticles: (a) Cube-like and (b) rod-like gold nanoparticles. The length of the scale bars corresponds to 50 nm. Adapted with permission from Macmillan Publishers Ltd: *Nat. Nanotechnol.* ([27]), copyright © 2011. (c) Silver nanoparticles with irregular shapes. Adapted with permission from [19]. OA CC BY 4.0. (d) Hematite nanospindles. The length of the scale bar corresponds to 200 nm. Reprinted with permission from [30]—Published by The Royal Society of Chemistry. CC BY 3.0.
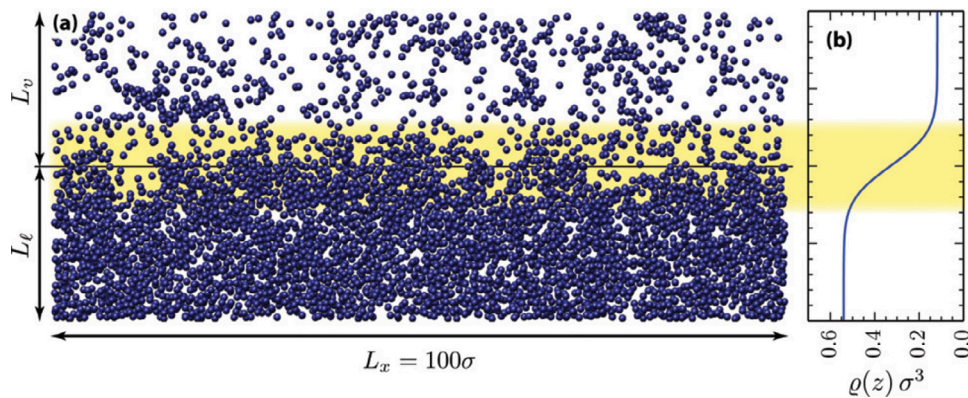
Figure 3. Simulation snapshot of the liquid-vapour interface for a Lennard-Jones fluid with pair potential $V(r) = 4\epsilon[(r/\sigma)^{-12} - (r/\sigma)^{-6}]$ at $T/\epsilon = 1.15$. (a) A vertical slice of width 3.5σ and height 40σ is shown with the interface region highlighted. (b) Corresponding mean density profile $\varrho(z)$. Reproduced with permission from [31]. © EPLA. All rights reserved.

$$\Delta E = \pi a^2 \gamma_{\ell v}(1 - |\cos\theta_c|)^2 + \tau l_c, \tag{4}$$

where τ is an effective line tension and l_c is the length of the contact line. For micrometer-sized particles, the contribution of the line tension is negligible; the trapping energy is proportional to the liquid-vapor interface tension $\gamma_{\ell v}$ and decreases with decreasing contact angle, see figure 6.

For small particles with sizes below one micrometer line tension becomes relevant [57], for large particles with sizes of several micrometers gravity has to be taken into account

[58–60]. The Eötvös or Bond number compares the contributions of interface tension and gravity to the total energy,

$$\text{Eo} = \text{Bo} = \frac{\Delta\rho g L^2}{\gamma_{\ell v}}, \tag{5}$$

where $\Delta\rho$ is the density difference of the two phases, g is the gravitational acceleration, and L is a characteristic length of the particle. Similarly, the energies due to line tension and surface tension are compared using the dimensionless number
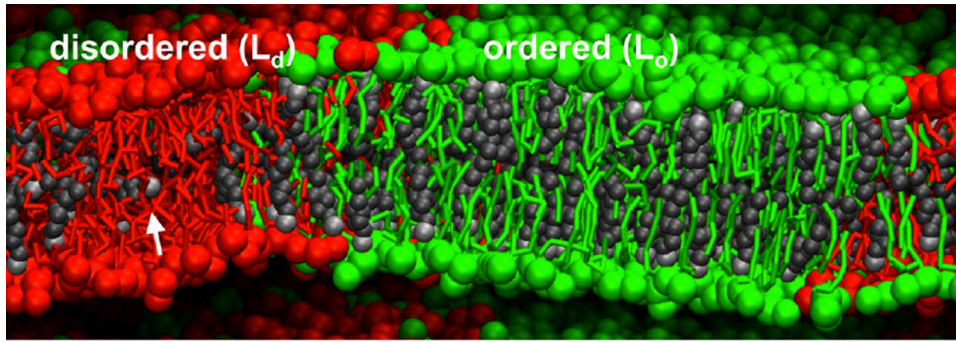
Figure 4. Structural and dynamic properties of the membrane domains. Side view of the planar diC$_{16}$-PC/diC$_{18:2}$-PC/cholesterol 0.42:0.28:0.3 system, revealing the molecular organization in both the L_o and L_d phases. The white arrow points to a cholesterol oriented in between the monolayer leaflets. Reprinted with permission from [32]. Copyright © 2008 National Academy of Sciences.

Table 1. Estimated attachment energies E_A (i) for spherical particles of radius r_p attached to an oil–water interface with a typical interface tension $\gamma = 28$ mN m$^{-1} \approx 6.75$ k$_B$T nm^{-2} [35], assuming that the interface tensions of the particle with both phases are identical and (ii) for spherical particles that are half-wrapped by a membrane with bending rigidity $\kappa \approx 2\,10^{-19}$J ≈ 50 k$_B$T [36, 37]. We use the particle-membrane adhesion strength $w \approx 0.2$ k$_B$T nm^{-2} between DMPC and silica ($w = 0.5 - 1$ mJ m$^{-2} = 0.12$–0.24 k$_B$T nm^{-2} is reported in [38]), the adhesion strength $w \approx 7 \cdot 10^{-3}$ k$_B$T nm^{-2} for receptor-ligand bond-mediated interaction ($w = 0.03$ mJ m$^{-2} = 7 \cdot 10^{-3}$ k$_B$T nm^{-2} is reported in [39]), and the adhesion strength $w \approx 2.5 \cdot 10^{-6}$ k$_B$T nm^{-2} between DOPC/DOPG and glass ($w = 10^{-5}$ mJ m$^{-2} = 2.4 \cdot 10^{-6}$ k$_B$T nm^{-2} is reported in [40]). The particle-membrane interaction is only attractive beyond a threshold particle radius.

System	r_p	E_A
Oil–water interface	10 nm	$-2 \cdot 10^3$ k$_B$T
Oil–water interface	1 μm	$-2 \cdot 10^7$ k$_B$T
DMPC-silica	10 nm	375 k$_B$T
DMPC-silica	20 nm	-375 k$_B$T
DMPC-silica	50 nm	-5650 k$_B$T
Receptor-ligand	50 nm	410 k$_B$T
Receptor-ligand	100 nm	-250 k$_B$T
DOPC/DOPG-glass	1 μm	600 k$_B$T
DOPC/DOPG-glass	5 μm	-160 k$_B$T

Table 2. Estimated interface-mediated and membrane-mediated bond energies E_b for particles at contact for (i) micrometer-sized spherical particles and ellipsoidal particles with aspect ratio b/a and $a = 1$ μm at planar oil–water interfaces with interface tension $\gamma = 28$ mN m$^{-1} \approx 6.75$ k$_B$T nm^{-2} [35] and for (ii) spherical particles with radius 500 nm attached to a vesicle with membrane bending rigidity $\kappa \approx 2 \cdot 10^{-19}$J ≈ 50 k$_B$T [36, 37]. Based on [43] and [44].

System	E_b
Spherical particles	—
Ellipsoidal particles with $b/a = 2$	$-4 \cdot 10^4$ k$_B$T
Ellipsoidal particles with $b/a = 3$	$-1 \cdot 10^5$ k$_B$T
Cuboidal particles with $b/a = 3$	$-7 \cdot 10^4$ k$_B$T
Spherical particles at membranes	-8 k$_B$T

$$\text{Li} = \frac{\tau}{\gamma_{\ell v} L}. \tag{6}$$

For micrometer-sized particles and typical density differences between, for example, silica and water, Bo $\approx 10^{-8}$ [61]; for line tensions and the corresponding surface tensions measured for polystyrene and poly(methyl methacrylate) particles at oil–water interfaces, Li = 0.01–0.1 [57]. In the following sections, we mainly discuss systems with Bo $\ll 1$ and Li $\ll 1$, where both gravity as well as line tension can be neglected.

The estimate for Li indicates that line tension may not always be entirely negligible for small micrometer-sized and large nanometer-sized particles. Line tension may qualitatively alter the behaviour of non-spherical particles at interfaces: for example, ellipsoidal and cylinderical particles may

undergo orientational changes in order to minimise the length of the contact line. In [57], contact angles have been measured for spherical particles and for prolate ellipsoidal particles with various aspect ratios obtained by deforming initially spherical particles. Here, an apparent decrease of the contact angle with increasing aspect ratio of the particles has been measured. This can be attributed to a line tension and a contact angle that is independent of particle shape [57]. The experiment predicts an effective line tension $\tau \approx 1$ nN that also includes experimentally-observed heterogeneities in the contact line. Other values for line tensions reported in the literature are in the pN to μN range [62].

One of the key reasons for the stability of colloidal assemblies at interfaces and of Pickering emulsions are the very high trapping energies for the particles [56, 63], see table 1. Calculations for non-spherical particles show that the trapping energies depend only weakly on particle shape and increase for both oblate and prolate deformations of spherical particles, see figure 6. At curved interfaces, the trapping energies of spherical particles have been shown to depend on the interface curvature and therefore on the Laplace pressure difference at the interface [64]. For spherical particles and a contact angle $\theta_c = 90°$, the trapping energy decreases with increasing interface curvature. For contact angles $\theta_c \neq 90°$, the trapping energy either increases or decreases depending on the sign of the contact angle and on whether the interface is curved towards or away from the particles.
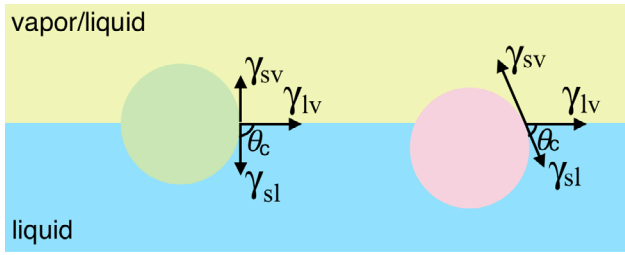
Figure 5. Spherical particles at a fluid-fluid or fluid-gas interface in a system with a solid spherical particle (s), a fluid (l), and a gas/second fluid (g). The contact angle θ_c for the green particle is 90°, while the contact angle for the red particle is smaller than 90°. The three interface tensions γ_{sv}, $\gamma_{s\ell}$, $\gamma_{\ell v}$ are sketched for each particle using arrows. They indicate the force balance given by the Young–Dupré equation that holds for all points along the three-phase contact lines.

To satisfy the Young–Dupré equation locally at every point on the three-phase contact line, see figure 5, the contact lines and therefore also the interfaces are often not planar for non-spherical particles. Also particle-surface inhomogeneities, either due to roughness or chemical surface patterning, e.g. for Janus particles, may induce contact-line undulations. Furthermore, imposed fields, such as gravity for large mm-sized particles or electromagnetic fields for electrically-charged or for magnetic particles, may lead to interface deformations. The capillary forces due to the system's tendency to reduce the total interface area between liquid and vapor is the origin of the capillary forces between particles, see table 2; very strong bond energies of $10^4 k_B T$ for micrometer-sized particles correspond to interface height perturbations of only 50nm [43].

The importance of hydrodynamic interactions for the dynamics of particles at interfaces is characterized by the capillary number

$$\text{Ca} = \frac{\eta v}{\gamma_{\ell v}} \tag{7}$$

with fluid viscosity η and typical particle velocity v. For typical velocities of 100 μm s^{-1} for particles with sizes of up to few micrometers in water [65], we find $\text{Ca} < 10^{-5}$. Therefore, for the systems discussed in this review article $\text{Ca} \ll 1$, such that hydrodynamic interactions can be neglected. Particle velocities can therefore be directly related to the forces acting on the particles and the friction by the fluid.

Self-assembly of colloidal particles at fluid interfaces is governed by both direct interactions, such as van der Waals and electrostatic interactions, and indirect interactions, such as forces due to overlap of interface distortions, popularly coined as capillary interactions [62, 66]. In 1980, Pieranski reported a two-dimensional colloidal crystal of spherical polystyrene colloids with a triangular lattice structure at an air-water interface induced by an asymmetric charge distribution [63], forced into two dimensions by the interface. A large number of more recent studies on colloids at interfaces that assemble due to interface-mediated and direct interactions show a rich variety of two-dimensional structures.

An overview of both single-particle and many-particle systems at interfaces is provided in the remainder of this section. In sections 2.1–2.4, we focus on various aspects of the
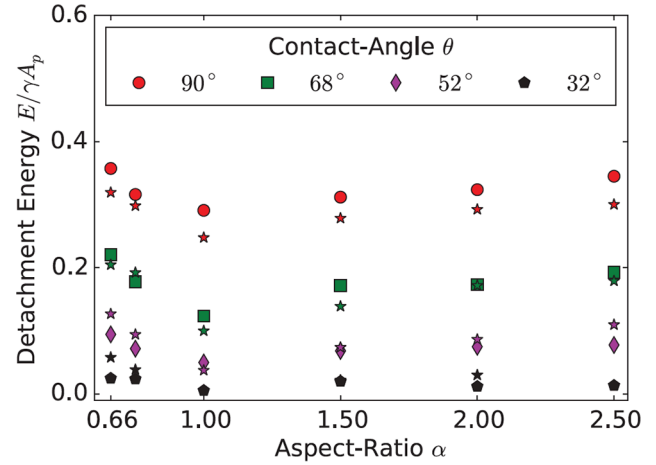
Figure 6. Trapping energies for spheroidal particles at flat interfaces. Numerical data obtained using Lattice Boltzmann simulations is compared with thermodynamical calculations ($\star$). Reprinted from [56] with the permission. Copyright (2014), AIP Publishing LLC.

interaction of single particles with interfaces, while in sections 2.5 and 2.6, we discuss two-particle and many-particle interactions, respectively. Section 2.7 focuses on the special case of particles at interfaces that are half immersed into an ordered fluid. We finally discuss applications in section 2.8.

2.1. Contact line deformation-induced interface deformation

An undulating contact line at a particle distorts a surrounding planar fluid interface. For a cylindrically-symmetric system, such as a spherical particle at an interface, the Young–Laplace equation that describes the interface deformation is best expressed in cylindrical coordinates [67],

$$\nabla^2 h(r, \phi) = 0. \tag{8}$$

The height profile $h(r, \phi)$ of the interface can then be expressed as product of a function of the radial coordinate r and a function of the angular coordinate ϕ around the sphere,

$$h(r, \phi) = R(r)\Phi(\phi). \tag{9}$$

The general solutions,

$$\Phi_m(\phi) = \Phi_{m,0} \cos(m(\phi - \phi_{m,0})) \tag{10}$$

and

$$R_m(r) = R_{m,0} r^{-m}, \tag{11}$$

are characterized by the contact line at the particle, described by $\Phi_{m,0}$, $\phi_{m,0}$, and $R_{m,0}$. The interface deformation decays faster with increasing distance from the particle the larger m, i.e. the larger the number of undulations along a circle around the particle.

The contact-line undulations can be expressed as multipole expansion,

$$h(r_c, \phi) = \sum_{m=2}^{\infty} H_m \cos(m(\phi - \phi_{m,0})), \tag{12}$$

where the contact radius r_c is often similar to the particle radius, H_m are the expansion coefficients, and $\phi_{m,0}$ the phase

angles. The first two terms of the expansion vanish, because without additional external forces the particles are at their optimal height and orientation at the interface. The lowest multipole contribution and the most important contribution for long-ranged interactions is the quadrupolar deformation with $m = 2$ [67],

$$h^{(2)}(r, \phi) = H_2 \cos[2(\phi - \phi_{2,0})]\left(\frac{r_c}{r}\right)^2, \qquad (13)$$

where H_2 characterizes the undulation amplitude of the contact line. The long-ranged interactions between two particles in the far field therefore decay with d^{-4}, where d is the interparticle distance.

Experimentally, imprinted contact-line shapes have to be distinguished from mere surface roughness. Whereas surface roughness often leads to temporary and random pinning of the contact line, engineered contact-line deformations are stable and well controlled. For instance, undulating plates allow the engineering of the interface deformation and the tuning of the capillary interaction between particles from attractive to repulsive [68, 69]. However, also nanometric roughness on microspheres or disc-like particles leads to strong capillary interactions due to contact-line pinning [67, 70–72]. The temporary nature of contact-line pinning can be observed for instance for metastable orientations of dumbbell-shaped particles at interfaces; the distribution of particle orientations relaxes towards the globally stable particle orientation when the system ages [73].

2.2. Interface deformation by non-spherical particles

In 1992, Lucassen first suggested that particles with complex shapes can induce interface distortions in absence of gravity [69]. He systematically calculated the interaction between sinusoidal interface deformations. However, the most common interface distortion due to non-spherical particles is the quadrupolar deformation, which is found for all elongated particles with homogeneous surface functionalization at planar interfaces in the far field [65, 74, 75]. For ellipsoidal particles, quadrupolar interface deformations can also be found in the near field [43, 75, 76]. For contact angles $\theta_c < 90°$, the interface is pulled down at the tips and pulled up near the long sides of the particle—and reverse for the inverse-wetting condition with $\theta_c > 90°$, see figure 7(a). For ellipsoidal particles and $\theta_c = 90°$—and for spherical particles—a planar interface remains undeformed.

Strength and nature of the interface distortions can be characterized using different quantifications: contour maps of the interface distortion, see figures 7(a) and (b), shapes of contact lines, see figure 7(c), differential heights Δu of the interface between the crest and trough along the contact lines, see figure 7(d), or height profiles along cross-sections, see figure 9(e). For well-defined particle shapes, in particular for ellipsoidal particles and quadrupolar interface deformations, the characterization of the interface deformation fields is uniquely determined by $\Delta u = z_{max} - z_{min}$, where z_{max} is
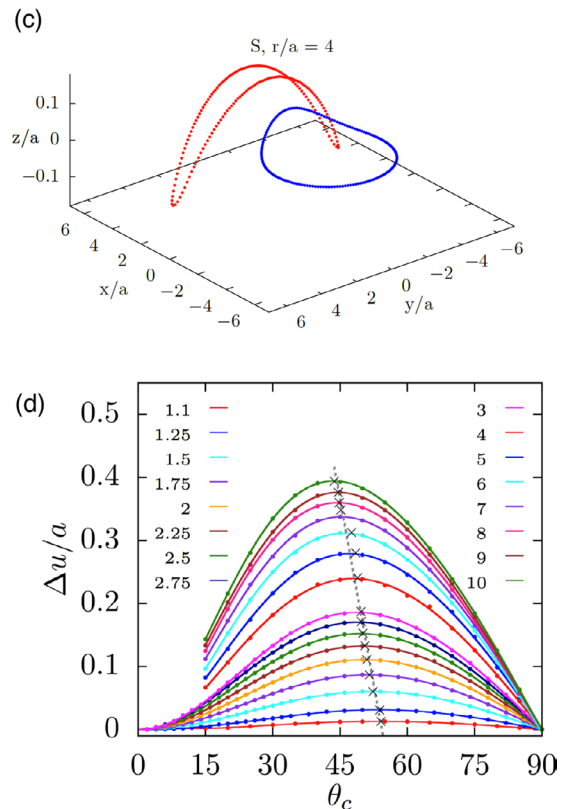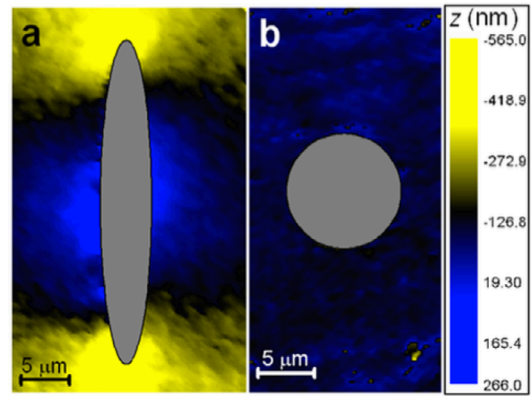
Figure 7. Characterization of interface deformations around particles. (a) Experimental plots of the interface distortions $z = h(x, y)$ around floated particles obtained from phase shifting interferometry sequences. (a) Ellipsoid. (b) Sphere. The particle bodies were artificially colored in gray. Reprinted with permission from [74]. Copyright © 2006 by the American Physical Society. (c) Contact line deformations for a spherical particle of radius $r = 4a$ next to an ellipsoidal particle of aspect ratio $b/a = 5$ for contact angle $\theta_c = 48.47$ for both particles. The spherical particle approaches the ellipsoidal particle at the side. Reprinted with permission from [43]. Copyright (2014) American Chemical Society. (d) Maximal height difference Δu of the contact line for ellipsoidal particles with several aspect ratios $1 \leqslant b/a \leqslant 10$. The numerical data are normalized by the half the length of the minor axis a and plotted as function of the contact angle θ_c. The maximum value of Δu, depicted by $\times$, shifts to smaller contact angles with increasing particle aspect ratio, as indicated by the grey lines that serve as guides to the eye. Reprinted with permission from [43]. Copyright (2014) American Chemical Society.

the maximum and z_{min} the minimum height along the contact line.

The height difference Δu for ellipsoidal particles vanishes for $\theta_c = 0°$ and for $\theta_c = 90°$ and assumes a maximal value Δu_{max} for $43° < \theta_c < 54°$ for ellipsoids with aspect ratios $1.1 \leqslant b/a \leqslant 10$ [43], see figure 7(d). The position of the peak shifts from larger to smaller contact angles with increasing aspect ratios of the particles [77], while the height of the peak increases from $\Delta u_{max}/a \approx 0.013$ for $b/a = 1.1$ to $\Delta u_{max}/a \approx 0.4$ for $b/a = 10$. Studies are available for ellipsoidal particles [43, 74, 75], for cylindrical [65], for cuboidal particles [43], and for rounded box-like particles [70]. The height difference along the contact line of elongated particles can be thought of as a measure for their capillary interaction strength. Systematic theoretical and experimental calculations thereby provide routes to tailor capillary assembly of multiple particles.

The experimental determination of contact angles using light microcopy is difficult, because the same interface deformation can be derived for two different contact angles. This 'contact-angle mystery' arises because the differential interface height distortion, i.e. $\Delta u/a$, does not show a monotonic increase with the contact angle θ_c, see figure 7(d). Due to the non-monotonic profile for ellipsoidal particles, for each value of $\Delta u/a$ there are two possible values for θ_c, see figures 8(a) and (b). However, the 'mystery' can be resolved by measuring a second quantity, such as the excess area S/S_0 plotted in figure 8(c), i.e. the ratio of the projected area by the contact line and the projected area at $\theta_c = 90°$ [74, 77].

In figure 8, results from theoretical contact-angle calculations for ellipsoidal particles with various aspect ratios are plotted together with corresponding experimental measurements of $\Delta u/a$ and with S/S_0 as function of the contact angle. The lower branch for smaller θ_c has already been reported in [74], the upper branch more recently in [77]. Only with the knowledge of both, experimental values for $\Delta u/a$ and for S/S_0, the correct branch of contact angle solutions can be singled out. A new technique using electron microscopy provides means to measure contact angles more directly than optical microscopy. This so-called freeze-fracture shadow-casting cryo-SEM (FreSCa) has been used to measure contact angles for wetting of spherical and ellipsoidal micro- and nanoparticles at liquid-liquid interfaces [57].

For more complex particle shapes, the connection between interface deformation and particle aspect ratio can be different from the case of 'simple' elongated particles. For example, figures 9(a)–(e) shows deformations around rounded box-like particles, where rises and dips depend on local particle shape rather than aspect ratio. Cuboidal particles can produce octupolar distortion fields with eight lobes (rises and dips), see figure 9(f). For rounded cylinders, there can even be multiple branches of possible contact angles due to the multiple peaks in the $\Delta u/a$ variation for certain aspect ratios (unpublished results). Table 3 provides an overview of the dominant multipole contributions for interface deformations and corresponding systems, several of them are discussed in more detail in the following.
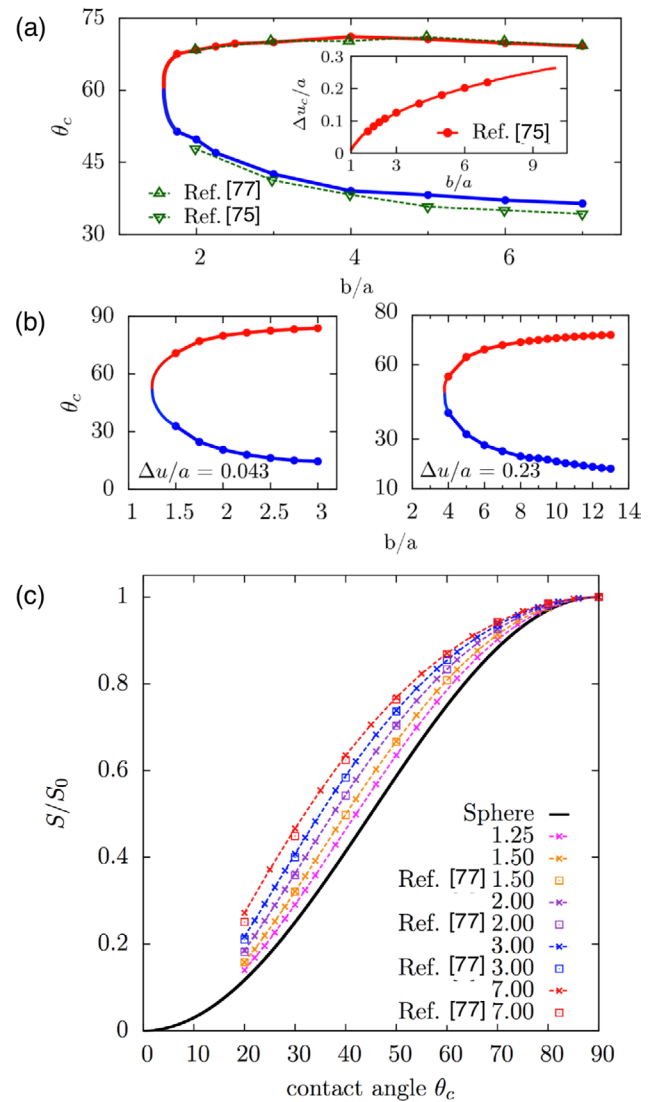

Figure 8. Calculations of contact angles for ellipsoidal particles. (a) Contact angles that correspond to experimentally measured values [74] for Δu (shown in the inset) for several aspect ratios b/a, see figure 7(c). The upper branch (red) is the solution for large θ_c, while the lower branch (blue) is the solution for small θ_c. (b) Contact angle branches as function of the aspect ratio for $\Delta u/a = 0.043$ (left) and $\Delta u/a = 0.23$ (right). (c) Ratio of projected area enclosed by the contact line for the contact angle θ_c to the projected area enclosed by the contact line for $\theta_c = 90°$, S/S_0, for ellipsoidal particles with aspect ratios in the range $1.25 \leqslant b/a \leqslant 7$. The data from [43] is plotted together with numerical data taken from [77]. For a spherical particle, S/S_0 varies as $\sin^2 \theta_c$, as shown by the solid line above. For all contact angles between $0°$ and $90°$, S/S_0 attains higher values for ellipsoidal particles in comparison to the analytical estimate obtained for a spherical particle. Adapted with permission from [43]. Copyright (2014) American Chemical Society.

2.3. Field-induced interface deformation

We discuss here gravity, buyoancy, and thin films in part 1 and non-planar interfaces in part 2.

2.3.1. Gravity, buyoancy, and thin films. The presence of graviational forces leads to floatation forces that cannot be neglected in the regime of large absolute values of the Bond number [59, 83–88, 89]. Particles either sink into the interface
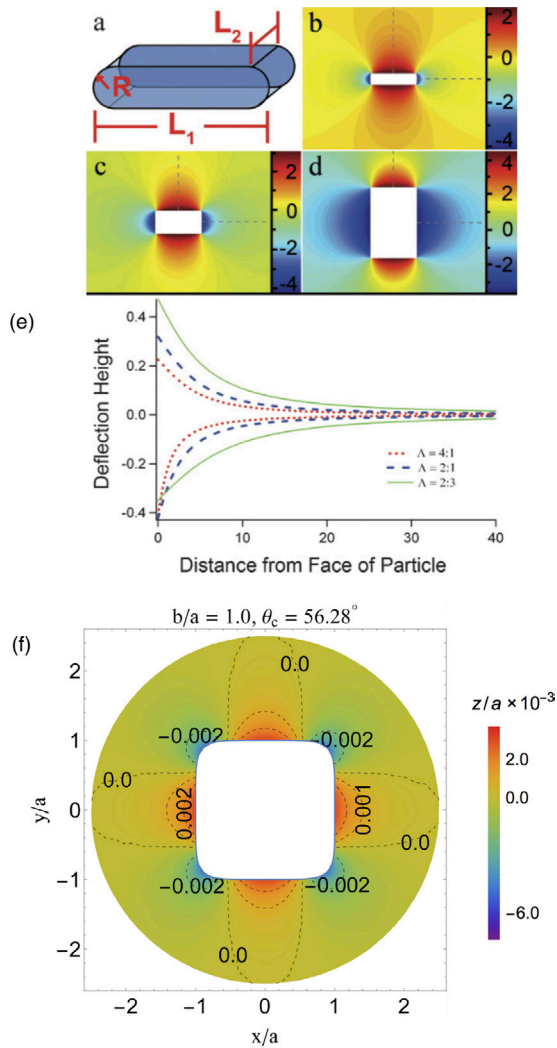
Figure 9. Interface deformations for rounded box-like and cube-like particles. (a) Particles have planar ends of length L_1, curved sides of length L_2, and radius of curvature R. Contour plot of the equilibrium configuration of the interface for particles with $L_1/R = 11.4$ and (b) $L_1/L_2 = 4.0$ (c) $L_1/L_2 = 2.0$ (d)$L_1/L_2 = 2/3$ (e) Surface shape profile as a function of distance from the middle of the curved faces ($h < 0$) and flat faces ($h > 0$) for different values of L_1/L_2. The heights are scaled by the length scale R. Reprinted with permission from [78] copyright of The Royal Society of Chemistry (f) Deformation profiles of an interface around a particle with Hauser's cube shape at contact angle $\theta_c = 56.28°$ that corresponds to maximum particle-induced interface distortion. Reprinted with permission from [43]. Copyright (2014) American Chemical Society.

if they are heavier than the fluid or float up if they are lighter than the fluid (buyoancy). Gravitational forces therefore induce dominant monopole interface deformations, so-called 'capillary charges', see equation (23) [90]. Some fascinating outcomes of the interplay of capillarity and gravity are water striders [99], meniscus-climbing insects [83, 84], and the cheerios effect in cereal bowls [59].

Monopole interface deformations are obtained as well for particles in thin films, where instead of gravitation the small thickness of the film compared with the particle size induces interface deformations [79, 100], see figure 10. The ideal interface positions on the particle are incompatible with the film thickness, which leads to immersion forces. For a thin

Table 3. Dominant multipole contributions to the interface deformations induced by particles. The interface deformations are determined by particle shape, size, surface functionalization, and external fields.

| Deformation	System	References
Monopole	part. in thin films	[79–82]
	part. in grav. fields	[58, 59, 83–88]
Dipole	elong. magn. part.	[89, 92]
Quadrupole	elongated particles	[43, 45, 70, 75]
Hexapole	elong. Janus part.	[93–95]
	cube-like particles	[96–98]
Octupole	cube-like particles	[43, 96]
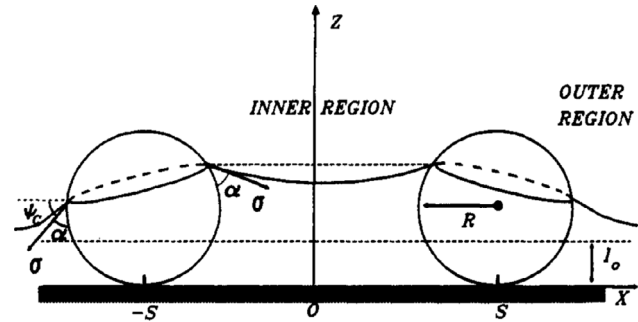
Figure 10. Two spherical particles partially immersed in a liquid layer on a horizontal substrate. The deformation of the liquid meniscus gives rise to interparticle attraction. Reprinted with permission from [79]. Copyright (1992) American Chemical Society.

film of fluid at a solid interface, the horizontal projection of the immersion force is [79]

$$F_x \approx 2\pi\gamma_{\ell v} r_c^2 (\sin^2 \Psi_c)\frac{1}{d_{cc}} \qquad (14)$$

with the radius r_c of the three-phase contact lines at the particles, the mean meniscus slope angle Ψ_c at the contact line, and the distance d_{cc} between the particles. This expression holds for $r_c \ll d_{cc} \ll (\gamma_{\ell v}/(\Delta\rho g))^{1/2}$, where $\Delta\rho$ is the density difference between the fluid and the gas. Figure 11 compares the floatation forces between particles with immersion forces for polystyrene latex particles in a water film on a glass substrate; in this example, the floatation forces decrease faster with increasing interparticle distance than the immersion forces.

As an instructive example, we discuss froth floatation as an application in more detail [101]. Here, grains of one solid are carried away with the froth, while grains of a different solid sink to the bottom of the floatation system. The selective adsorption of a collector chemical onto a mineral in a floatation plant determines—among others—the attachment of the mineral to bubbles used for separation. The stability of the froth with the particles depends mainly on the properties and the amounts of particles [80]. The so-called capillary pressure due to the liquid that drains from the film because of gravity measures the pressure when the film ruptures. This critical pressure increases if particles stabilise the film, e.g. spherical particles with contact angles far below 90°, and decreases if particles destabilise the film, e.g. particles with sharp edges.
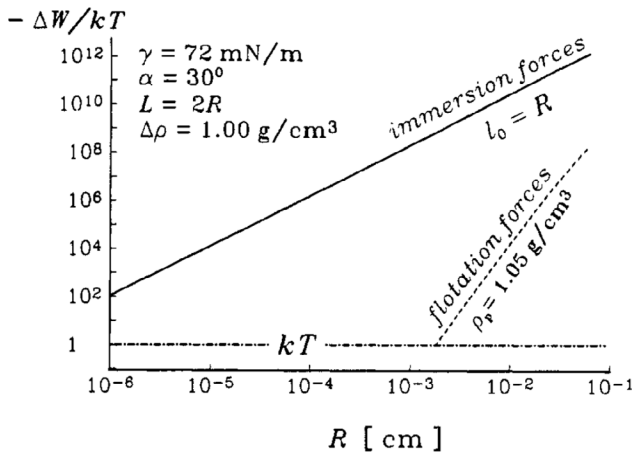
Figure 11. Comparison between immersion and floatation capillary forces between two spherical latex particles in a water film on a glass substrate: dependence of the capillary interaction energy, ΔW, on the particle radius, R. The distance between the particles is $L = 2s$, the contact angle $\theta_c = \alpha$, and the liquid-vapor interface tension $\gamma_{\ell v} = \gamma$. See figure 10 for a sketch of the system. Reprinted with permission from [79]. Copyright (1992) American Chemical Society.

Whether a particle stabilizes or destabilizes a film furthermore depends on the orientation that the particle assumes at the interface [102], see section 2.4. Figure 12 shows how a thin film ruptures due to the presence of a non-spherical sharp-edged particle.

2.3.2. Curved interfaces. Particles at curved interfaces experience forces not only due to the presence of the interface, but also because of the Laplace pressure. Curvature gradients of the interface lead to lateral forces, and curved interfaces modify interface-mediated interactions between particles [61, 64, 71, 72, 103, 104], see figure 13; vice versa, particles at high densities can induce spontaneous interface curvature [105]. Mean curvature H and deviatoric curvature $\delta c = c_1 - c_2$ determine the trapping energy [104]

$$E_{\text{trap}} = E_F - \pi\gamma_{\ell v}a^4\sin^4\theta_c\left(\frac{3}{4}H^2 + \frac{1}{24}\delta c^2\right), \quad (15)$$

where E_F is the trapping energy at the flat interface, see equation (4).

For a spherical colloid of radius a on a spherical droplet of radius R_d (i.e. $H = R_d^{-1}$ and $\delta c = 0$), this implies $\Delta E_{\text{trap}} = E_{\text{trap}} - E_F = -(3/4)\pi\gamma_{\ell v}a^4\sin^4\theta R_d^{-2}$, which is the interface curvature-induced contribution. This term is evaluated by considering contributions due to both the interface energies and the work done against the Laplace pressure. A similar estimate for the trapping energies attempted previously in [106] without including the work done by the Laplace pressure resulted in the correction term to be $\Delta E_{\text{trap,def.}} = +(3/4)\pi\gamma_{\ell v}a^4\sin^4\theta R_d^{-2}$. This result is consistent with equation (15) when the contribution due to the pressure term, $\Delta E_{\text{trap,Lapl.}} = -(3/2)\pi\gamma_{\ell v}a^2\sin^2\theta R_d^{-2}$, is added to it [104].

For a minimal surface with mean curvature $H = 0$, such as for a catenoidal interface shape, the correction term compared
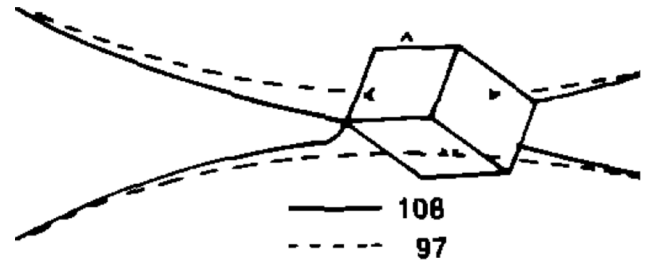
Figure 12. Frames of a recording of an approximately 160 μm-sized hydrophobic galena particle with $\theta_c \approx 80°$ rupturing a film of distilled water. The dashed line indicates the interface position in frame 97, both interfaces join at the sharp edge of the galena particle in frame 108. The time difference between both frames is 7.8 ms. After frame 108, the film ruptures. Adapted from [80], Copyright (1982), with permission from Elsevier.

with the flat interface depends only on the deviatoric curvatue δc. The trapping energy of a colloidal particle on a catenoidal minimal surface is thus $\Delta E_{\text{trap}} = -(1/24)\pi\gamma_{\ell v}a^2\sin^2\theta\delta c^2$.

On an interface with varying curvature, the lateral force on the trapped particle is given by [104]

$$F = \pi\gamma_{\ell v}a^4\sin^4\theta\left(\frac{3}{2}H\nabla H + \frac{1}{12}\delta c\nabla\delta c\right). \quad (16)$$
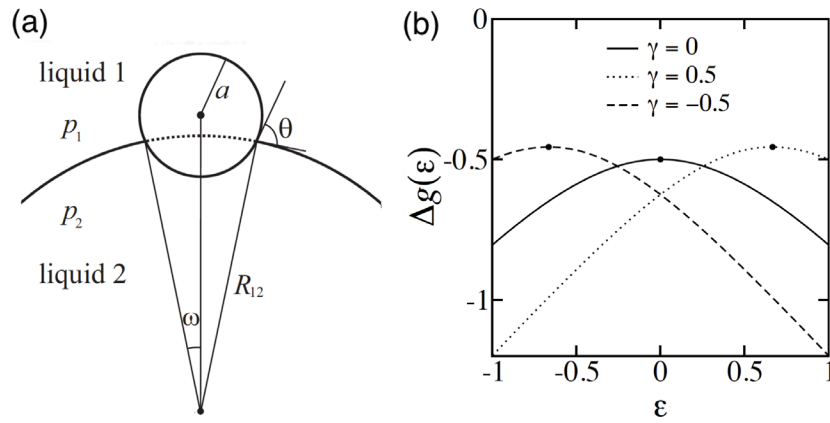
Thus, spherical particles on interfaces with curvature gradients experience forces depending on both the absolute values and the gradients of the mean and deviatoric curvature to move towards regions of high mean and deviatoric curvatures (and therefore also high Gaussian curvatures because $K = c_1c_2 = (H^2 - \delta c^2)/4$). Recent experiments of microspheres on interfaces with different curvatures have evaluated these forces to be of the order $F_c = -2.5 \pm 0.3$ fN for silica beads with radii $a = 2$ μm at oil–water interfaces ($\gamma_{\ell v} = 28$ mN m^{-1}) with contact angle 30° and, for interface, curvatures of the order of $H \approx 0.008$ μm^{-1} [35].

Theoretical estimates of capillarity at curved interfaces—which neglect pinning—suggest that capillary forces for particles that are smaller than the capillary length

$$L_c = \left(\frac{\gamma_{\ell v}}{\rho_\ell g}\right)^{1/2}, \quad (17)$$

where ρ_ℓ is the density of the fluid, are proportional to both a^4 and the gradient of the Gaussian curvature, ∇K [35]. This has been verified in experiments where large microposts induce a curvature gradient and cause smaller particles to migrate along the deformed interface to assemble in regions of high Gaussian curvature, see figure 14.

Experimental evidence further suggests that capillary migration on curved interfaces can be enhanced by contact-line pinning. Contact-line undulations, which lead to finite local interface curvatures, induce capillary forces of the order $6 \cdot 10^3$–$5 \cdot 10^4$ k_BT, which are much larger compared with the weak forces due to capillarity for perfectly smooth spherical particles. The experiments demonstrate that rough microspheres, microdisks, and rod-like particles move along deterministic trajectories to regions of maximum deviatoric curvature [71, 72, 103]. Non-spherical particles do not only migrate

Figure 13. Spherical particles at curved interfaces. (a) Schematic of spherical colloids of radius a, trapped at a droplet. (b) Theoretical estimates of normalized interface energy as function of droplet curvature. Reprinted with permission from [64]. Copyright (2006) AIP publishing.
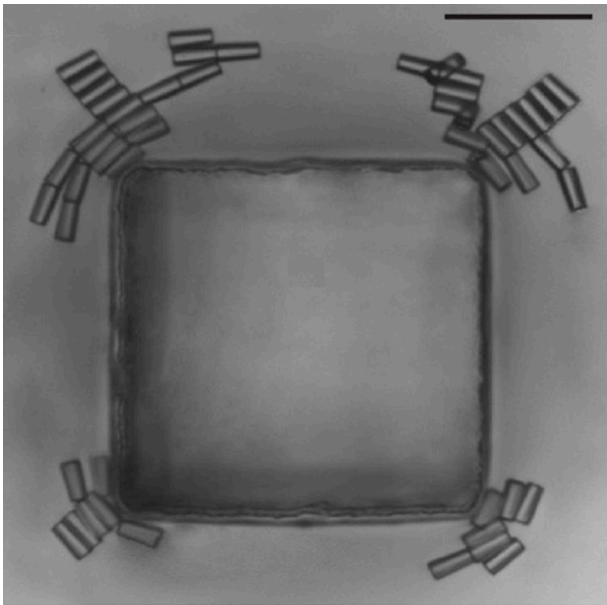
Figure 14. Particle migration near a square micropost. Complex structures formed by aggregated particles near the corners of the micropost. The scale bars corresponds to 100 μm. Reprinted with permission from [103].

translationally by sensing the background interface curvature, but also orient themselves to align their long axes, such that the excess area is minimized. For example, cylindrical particles reorient either parallel or perpendicular to the groove as the interface curvature changes from concave to convex [107].

2.4. Non-spherical shapes, surface heterogeneities, and particle orientations For non-spherical particles, the orientation of the particles at interfaces, as well as particle shape, size, and surface properties have to be taken into account to determine adsorption energies and interface deformations. Cube-like particles can be oriented in a corner-top or face-top orientation depending on the contact angle. Elongated particles in a magnetic field or elongated Janus particles in their stable orientations can be oriented with their long axes tilted with respect to the interface.

2.4.1. Cube-like particles. One way to estimate the adsorption energy of a particle at an interface is to calculate the area of the fluid interface that is 'cut out'. This estimate can be exact if the interface tensions between particle and both phases are equal. For a particle that is symmetric with the interface acting as a mirror plane, the surrounding interface remains planar. However, in general particle-induced deformations of the surrounding interface can change adsorption energies and stable particle orientations even qualitatively. Figure 15(a) sketches the various angles by which a cube-like particle can be rotated. Figure 15(b) shows deformation energy calculations for the contact angles $\theta_c = 90°$ and $\theta_c = 72.5°$. For $\theta_c = 90°$ the flat-interface approximation predicts the edge-top orientation to be globally stable, while accounting for the deformation of the surrounding interface the corner-top orientation is found to be globally stable.

Figure 15(c) shows specific orientations for a cube-like particle at an interface. For a contact angle $\theta_c = 72.5°$, the globally stable state is the face-top orientation, while for $\theta_c = 90°$ the globally stable state is the corner-top orientation. Figure 15(d) shows the predicted interface deformations for both cases using the same scale: hexapolar for the corner-top orientation and almost planar for the face-top orientation. Capillary interactions between the cubes are therefore expected to be much stronger in the corner-top orientation compared with the face-top orientation. For particles with complex shapes, such as cube-like particles, a multitude of kinetically stabilised orientations and corresponding multipolar interface deformations is expected to be observed in experiments.

2.4.2. Janus particles. A simple non-spherical particle with a stable tilted state is a Janus dumbbell, which consists of two spherical particles made from different materials, see figures 16 and 17. These particles do not deform planar interfaces, because the contact line around each of the spherical particles is a circle. Figure 16(a) shows the experimentally observed orientations for dumbbell particles that consist of an hydrophobic spherical particle of radius R_a and a hydrophilic spherical particle of radius R_p. In their lowest-energy orientation, the spherical particles intersect the interface at different heights. The tilt angle of the dumbbell in the lowest energy state is [73]
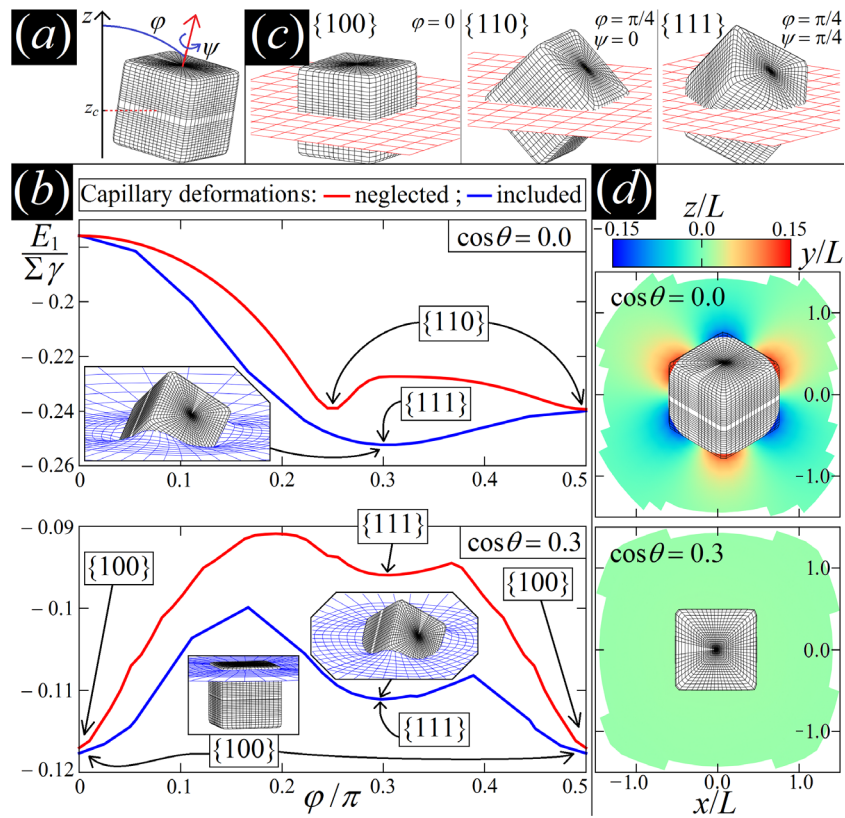
Figure 15. Orientations of cube-like particles at interfaces. (a) Configuration of a cubic particle at a fluid-fluid interface. (b) Adsorption energy of a single cube (side L) at a fluid-fluid interface, in units of the product of the cube surface area and the interface tension, $\Sigma\gamma$, minimized over the center of mass height and the internal Euler angle ψ as function of the polar angle ϕ for contact angles $\theta_c = 90°$ and $\theta_c = 72.5°$. The blue and red lines include and neglect capillarity, respectively. The labels 100, 110, and 111 indicate the cube's orientation in each minimum of the energy. The insets show, for the equilibrium configurations, a 3D view of the interface shape (blue grid) close to the particle (black grid), as calculated by our method. (c) 3D illustration of the 100, 110, and 111 orientations of a cube, where the red grid represents a plane parallel to the flat interface. (d) Contour plots of the deformed-interface height profile for the global minimum-energy configuration of the cube. For $\theta_c = 90°$, a hexapolar deformation emerges, while for $\theta_c = \arccos 0.3$, the interface is essentially undeformed. Reprinted with permission from [97]. Copyright (2016) by the American Physical Society.

$$\cos\theta_r = \frac{\cos\theta_p - \alpha\cos\theta_a}{((b/a) - 1)(\alpha + 1)}, \quad (18)$$

see figure 16(b). Here θ_p is the contact angle at the polar particle, θ_a is the contact angle at the apolar particle, $\alpha = R_a/R_p$ is the relative size of the two lobes, and $b/a = (R_a + R_p + d)/(R_a + R_p)$ is the aspect ratio.

With decreasing aspect ratio, the tilt angle of the Janus dumbbell increases. For aspect ratio $b/a = 2$, only one of the spherical particles is in contact with the interface. However, also for cases where the tilted orientation of the dumbbell is predicted to have the lowest energy, a substantial fraction of particles are found experimentally in one of the kinetically stable orientations, where only one of the spherical particles intersects the interface [73]. The lowest-energy orientation, where both spheres are at the interface, coexists with two kinetically stable orientations where only one of the spheres is at the interface. Because the energy for an orientation where only one spherical particle is in contact with an interface does not depend on the tilt angle, an arrest in such a state could be caused by surface roughness. In these trapped states, the particles can therefore reorient to the tilted orientation only by diffusion.

Unlike Janus dumbbell particles, Janus ellipsoidal particles that are half hydrophobic and half hydrophilic do not show a continuous transition of their the orientation between a tilted long axis and a perpendicular long axis to the interface, see figures 17 and 18. Energy landscapes for various orientations of an ellipsoidal and a dumbbell particle are shown in figure 17. The lowest energy states for different aspect ratios are indicated in the figure using green symbols; the discontinuous transition in the particle orientation is clearly visible. The tilted orientation is only stable above a threshold aspect ratio and the orientation of the particle orientation jumps to the perpendicular orientation below this aspect ratio [108]. These energies for various particle orientations have been calculated numerically, under the assumption of a flat interface surrounding the particles.

Whereas for ellipsoidal particles with homogeneous surface properties the deformations of the surrounding interface are quadrupolar with a dip at the tips and a rise at the long sides for contact angles below 90°, see section 2.2, the deformations of the interface around Janus ellipsoids can show both a dip and a rise along their long sides [93], see figure 18. Similar interface deformations have been observed for double-hydrophilic Janus cylinders with aspect ratios 0.9, 1.2, and

2.4 [94], see figure 19. The cylinders are found in kinetically trapped end-on orientations as well as globally stable tilted orientations. The cylinders have asymmetric hydrophilicity unlike most studies where the Janus particles have amphiphilic properties [94]. In their tilted orientations, they induce hexapolar interface deformations that lead to capillary interaction. Complex particle assemblies have been observed due to the multi-lobed deformations and the non-determininistic assembly.

2.4.3. Particles in magnetic fields. An external magnetic field can be used to tune the orientation of prolate ellipsoidal magnetic particles at fluid interfaces [41, 92, 109], see figure 20. The field tends to align the magnetic dipole with the direction of the applied magnetic field,

$$E_{\text{ext}} = -\boldsymbol{\mu} \cdot \mathbf{H} = -B\cos\phi, \qquad (19)$$

where $\boldsymbol{\mu}$ and $\mathbf{H}$ are the dipole and the field, respectively. The angle ϕ indicates the particle orientation and $B = |\mu||H|$ represents the field-dipole strength. The total free energy of the particle at the interface, neglecting particle-induced interface deformations, can therefore be written as

$$E_{\text{int}} = -\gamma_{\ell v} S + (\gamma_{sv} - \gamma_{s\ell}) A_{sv} - B\cos\phi, \qquad (20)$$

where S is the area of the interface 'cut out' by the particle, and A_{sv} is the area of the particle in contact with the vapor/the second liquid.

If the field is oriented normal to the interface and if the direction of the permanent magnetic dipole coincides with the major axis of the ellipsoid, the analytical estimation of the tilt energy predicts that at a critical field strength the particle 'jumps' from a tilted orientation to a vertical orientation. Here, $\phi = 0°$ and $\phi = 90°$ correspond to vertical and horizontal particle orientations, respectively. In figure 21, the energies of magnetic prolate ellipsoidal particles are shown as function of their orientation angle for various aspect ratios and field strengths. For particles with aspect ratio $b/a = 1.67$ and length of the minor axis a $= 30$ nm, the energy barrier between vertical and tilted states can be several hundred $k_{\text{B}}T$, such that the particles are trapped in one of both orientations.

Lattice-Boltzmann simulations have been used to investigate the orientations of magnetic ellipsoidal particles in external fields including the deformations of the surrounding interface [91]. The simulations show that the interface deformations around the particles significantly affect the tilt angles for a given dipole strengths, altering the properties of the reorientation transition. Figure 22 shows a simulation snapshot of the deformed interface and a plot of the tilt angle for various field strengths together with the analytical approximation discussed above. The simulation snapshot shows that the interface deformations remove more interface than in the planar-interface approximation, which lowers the free energy. Deviations from the approximate result are found mainly for high aspect ratios.

The discontinuous transitions allows the switching of the particle orientations using external magnetic fields, which could find applications for instance using its dynamically-tunable optical properties for electronic readers [110].
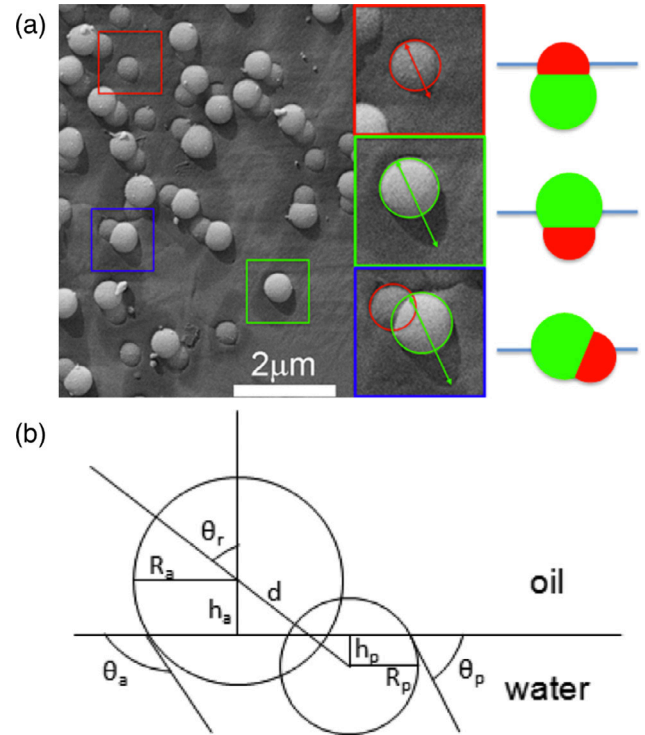
Figure 16. Amphiphilic dumbbell particles at an oil–water interface. (a) In experiments, three dumbbell orientations are found: only the hydrophilic sperical particle intersects the interface, only the hydrophobic spherical particle intersects the interface, and both spherical particles intersect the interface. The circles and arrows indicate the size of the particle crossection at the interface and the shadow length obtained by freeze-fracture, shadow-casting (FreSCa) cryo-scanning electron microscopy, that can be used to measure the contact angle. (b) Schematic diagram highlighting the geometry of the dumbbells at a liquid-liquid interface. Reprinted with permission from [73]. Copyright (2014) American Chemical Society.

Furthermore, also the dipolar interface deformations can be switched on and off and thus lead to switchable capillary interactions between particles adsorbed at fluid interfaces.

## 2.5. Long-range interface-mediated interactions

Overlaps of interface deformations around particles lead to interface-mediated interactions, also called (lateral) capillary forces. Capillary interaction energies between two particles, see figure 23, can be calculated based on the difference between the changes of the fluid-vapor interface area for placing two particles at given center-of-mass separation d_{cc} and for placing two isolated particles at a planar interface. The corresponding capillary interaction energy is [67]

$$\Delta E_{\text{cap}} = \gamma_{\ell v}(\Delta S_{\text{AB}} - \Delta S_{\text{A}} - \Delta S_{\text{B}}), \qquad (21)$$

where ΔS_{AB} is the change of the fluid-vapor interface area around the interacting particles, and ΔS_{A} and ΔS_{B} are the changes of the interface areas around the single particles. Interface-mediated interactions follow power laws in the far field and are thus long-ranged. In the near field, the interactions strongly depend on the particle shapes. Because the dynamics occurs in the Stokes regime for small capillary numbers,
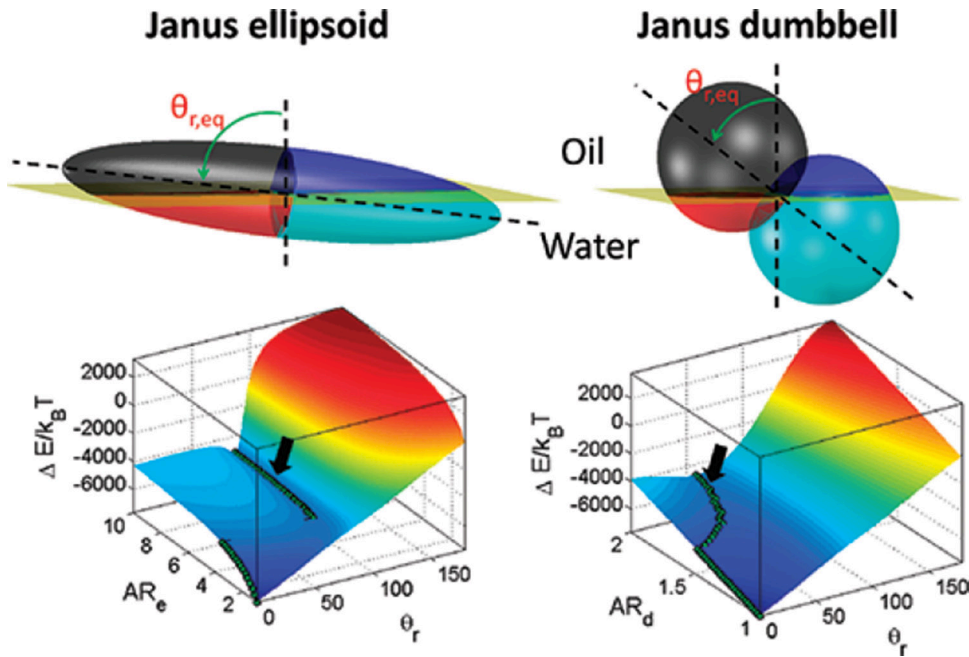
Figure 17. Janus ellipsoid and Janus dumbbell at an interface with corresponding energy landscapes for particle orientations. While the dumbbell smoothly transitions to the perpendicular orientation with increasing aspect ratio, the ellipsoid jumps from a small tilt angle to the perpendicular orientation beyond a critical aspect ratio. Reprinted with permission from [108]. Copyright (2012) American Chemical Society.
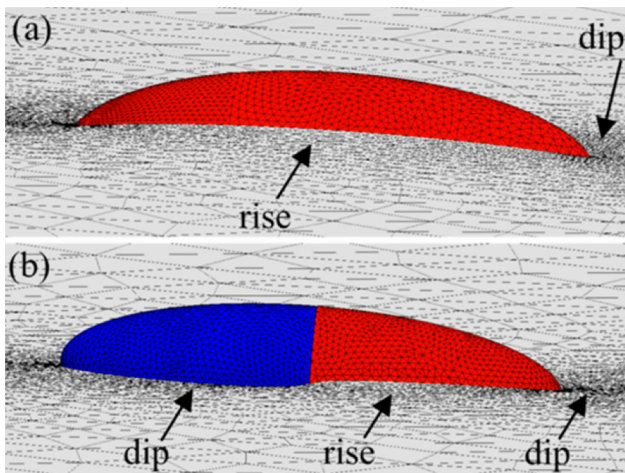
Figure 18. An ellipsoidal particle with (a) homogeneous surface properties and (b) a Janus ellipsoid at an interface. Around an ellipsoid with homogeneous properties and contact angles below $90\,^\circ$ the interface is suppressed at the tips and pulled up at the sides of the particle. Around a Janus ellipsoid the interface can experience a hexapolar deformation. Reprinted with permission from [93]. Copyright (2013) American Chemical Society.

see equation (7), the particle velocities are proportional to the interaction forces and can therefore be extracted for example from videos. Analytical solutions for the interaction forces are available in the far field, while numerical calculations have to be used in the near field.

2.5.1. Far-field interactions. For large distances between particles, the deformation field of particle A can be assumed to be small at the position of particle B and vice versa. The capillary interaction energy can then be calculated using the superposition of the interface deformations around the single particles [58, 67, 111]

$$\Delta E_{\text{cap}} = \frac{\gamma_{\ell v}}{2} \int dS \left((\nabla(h_A + h_B))^2 - \sum_{i=A,B} (\nabla h_i)^2 \right)$$
$$= \gamma_{\ell v} \int dS\, \nabla h_A \cdot \nabla h_B, \tag{22}$$

where h_A and h_B are the interface height deformation fields due to particle A and B, respectively. The lowest multipole contribution for a given system, see table 3, dominates the interaction.

For sufficiently large particles for that gravity or buyoancy have to be considered, the capillary forces act between two monopole interface deformations [58]

$$\Delta E_{\text{cap}}^{\text{mon}} = -2\pi\gamma_{\ell v} Q_1 Q_2 K_0(d_{cc}/L_c), \tag{23}$$

with the capillary length defined in equation (17), the mass density $\Delta\rho$ between the upper and the lower phase, and the capillary charges $Q_i = r_i \sin(\psi_i)$. The angle ψ_i is the slope of the interface at radius r_i, the radius of the contact line. For $qR_i \ll 1$, $Q_i \approx (q^2 R_i^3/6)(2 - 4D_i + 3\cos\alpha_i - \cos^3\alpha_i)$ with $D_i = (\rho_i - \rho_\ell)/(\rho_g - \rho_\ell)$, particle mass density ρ_i, fluid mass density ρ_ℓ, and upper fluid/gas mass density ρ_g.

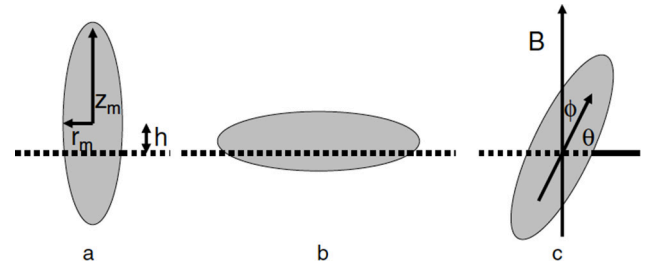Stamou *et al* first presented an analytical result for the pair potential between two quadrupolar deformation fields in polar coordinates [67]. In this quadrupolar approximation, the energy between two ellipsoidal particles is

$$\frac{\Delta E_{\text{cap}}^{\text{quad}}}{\gamma_{\ell v} a^2} = -3\pi \cos(2\omega_1 + 2\omega_2)\left(\frac{\Delta u}{a}\right)^2 \left(\frac{d_{cc}}{a}\right)^{-4}, \tag{24}$$
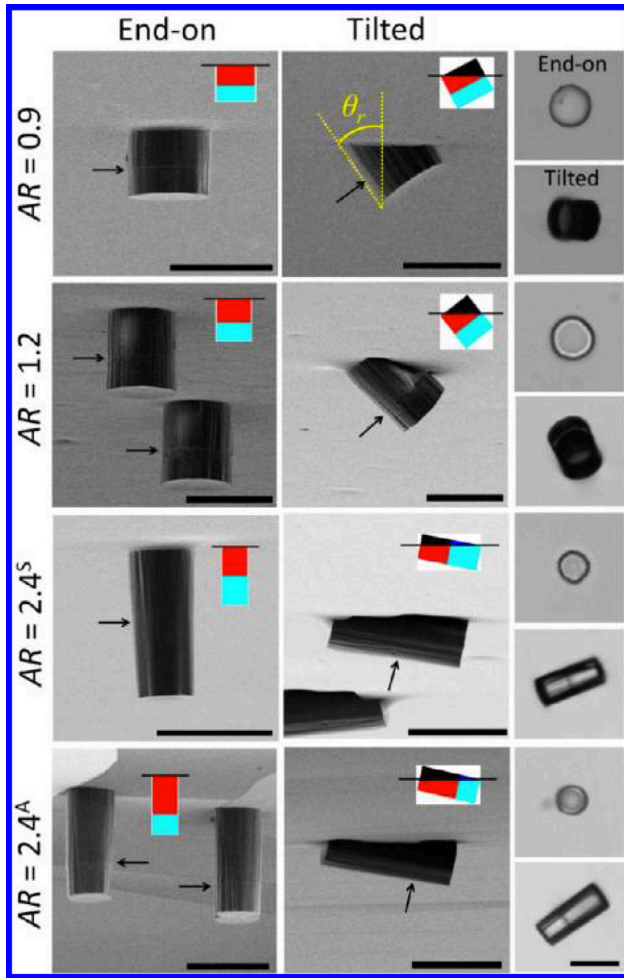
Figure 19. Configurations of double-hydrophilic Janus cylinders at the air-water interface. The first and second columns are SEM images of Janus cylinders embedded in PDMS slabs prepared by the gel trapping method. Arrows indicate the location of the wettability separation line. The schematic representations show the side view of particle configurations at the air-water interface where four colors represent four different particle-fluid surfaces: weakly polar surface in air (black), weakly polar in water (red), strongly polar in air (blue, rarely shown), and strongly polar in water (cyan). The third column shows the corresponding optical microscopy images. The scales bars are 50 μm. Reprinted with permission from [94]. Copyright (2013) American Chemical Society.
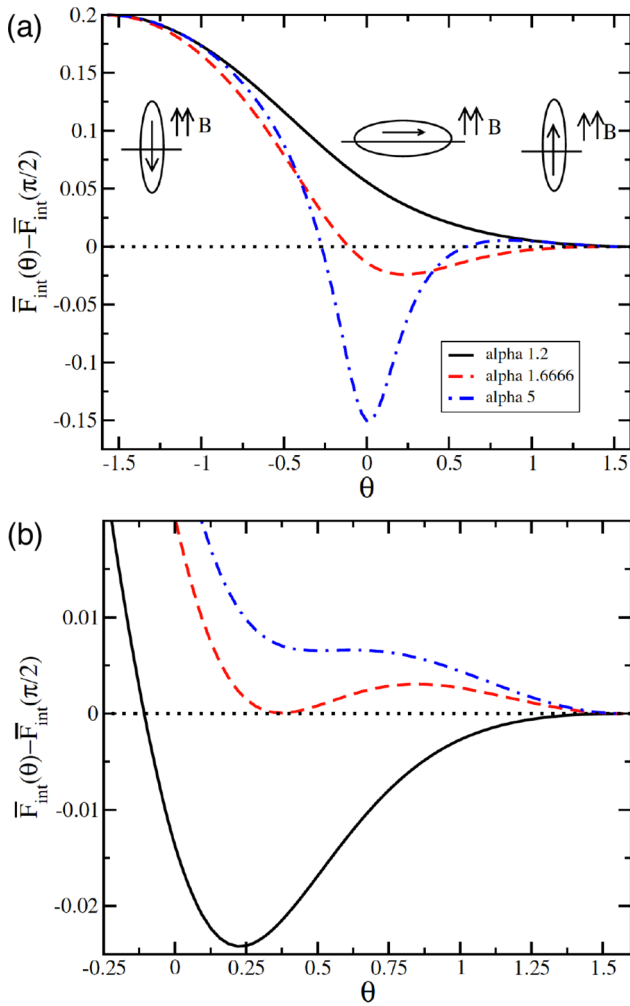

Figure 20. Sketch of an ellipsoidal particle adsorbed at a liquid-liquid interface in (a) vertical, (b) horizontal, and (c) tilted orientation. The variables defining the geometry and orientation of the particle are discussed in the text. The direction of the magnetic field is indicated by *B*. Reprinted from [41]. © IOP Publishing Ltd. All rights reserved.

Figure 24 shows interaction potentials for cylindrical particles and forces between two ellipsoidal particles using the superposition approximation. For large distances, the expected dependences of potential and force with the inter-particle distance d_{cc} for elongated particles, $V_{cap} = (d_{cc}/a)^{-4}$ and $F_{cap} = -\partial V(d_{cc})/\partial d_{cc} \propto (d_{cc}/a)^{-5}$, are observed for both cylindrical and ellipsoidal particles [65, 75]. Deviations are observed for small interparticle distances, which is discussed in section 2.5.2.

2.5.2. Near-field interactions. Elongated particles that touch each other have lower bond energies than predicted by the quadrupolar approximation in side-by-side orientation and higher bond energies in end-to-end orientation, see figure 24. Capillary self-assembly is determined by the contact interactions between the particles, therefore near-field interactions are important for all many-particle systems. Uncharged ellipsoidal particles at low Bond numbers preferentially align in side-by-side orientation [45]. The higher stability of the side-by-side orientation over the tip-to-tip orientation is obvious from equation (24) and is qualitatively unchanged by the deviation from the ideal quadrupolar approximation in the near field.

Using triangulated surfaces and energy minimisation, numerical calculations of deformation energies have been applied for various particle shapes, orientations, and contact angles. Figure 25 shows snapshots and interaction potentials for pairs of identical ellipsoidal particles with aspect ratios $b/a = 2$ and $b/a = 3$ [43]. The bond energies increase quadratically as function of the bond angle $|\phi|$ that quantifies deviations from the side-by-side orientation with $\phi = 0°$. Figure 26 shows the bond-bending energies for two ellipsoids with $b/a = 3$ and $\theta_c = 80°$. The capillary torque $T = -\partial E/\partial \phi$ on each particle quantifies the resistance to rotation from the equilibrium state. The plot of T versus $180° - \phi$ shows a linear elastic regime with $T = G\phi$, where $G = 0.0015\gamma a^2$ [76]; the torques may reach values up to 10^3–$10^4 k_B T$. A bending modulus for the polymer-like assemblies of particles at the interface can be extracted from many-particle calculations. If two ellipsoids with different aspect ratios interact, the stable assembly is an arrow [112], see figure 27.

Unlike ellipsoidal particles, cylindrical particles preferentially assemble in end-to-end orientation, see figure 28. Because of the flat ends of cylindrical particles, the contact

see figure 23. The maximal contact line deformations Δu depend on the contact angles and the aspect ratios of the particles, see figure 7. The angles ω_1 and ω_2 measure the orientations of the particles with respect to the line joining their centers of mass. For $\omega_1 = \omega_2 = 90°$ the particles are in side-by-side (S-S) orientation, for $\omega_1 = \omega_2 = 0°$ in tip-to-tip (T-T) orientation. Equation (24) predicts attraction for S-S and T-T orientation, and repulsion for tip-to-side (T-S) orientation with $\omega_1 = 0°$ and $\omega_2 = 90°$. Interestingly, the magnitudes of the interaction potentials are equal in S-S, T-T, and T-S orientation for equal center-of-mass distances. Kralchevsky *et al* extended the multipole approach to multipoles of arbitrary orders [105]. Whereas for weak deviations from circular contact lines a polar multipole expansion is most appropriate, for ellipsoidal particles with higher aspect ratios the appropriate choice are elliptical multipoles [75].

Figure 22. Magnetic ellipsoidal particles in an external field. (a) Simulation snapshot of an ellipsoidal particle with aspect ratio $\alpha = 3$ unter the influence of a dipole field $B/A_p\gamma_{12}$. (b) Comparison of the tilt angle of the particle obtained from the analytical, planar-interface approximation in [41] and the numerical data in [91]. Although the numerical data qualitatively confirms the prediction of a discontinuos transition, there are quantitative deviations in particular at higher aspect ratio. Reprinted from [89] with permission from The Royal Society of Chemistry.

Figure 23. Two ellipsoidal particles at an interface. The angles ω_1 and ω_2 indicate the orientation of the particle 1 or 2, respectively, with respect to the vector joining the centers of the two particles. The center-to-center distance is given by d_{cc} for a particle of aspect ratio b/a. Reprinted with permission from [43]. Copyright (2014) American Chemical Society.
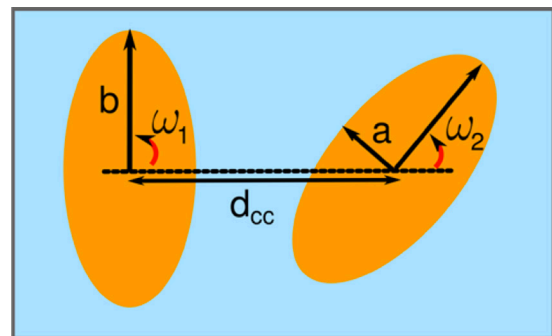
Figure 21. Energy of a magnetic ellipsoidal particle at an interface as function of its orientation. (a) The results for particle aspect ratios $b/a = \alpha = 1.2$, $b/a = \alpha = 1.6666$, and $b/a = \alpha = 5$ correspond to a representative field strength $\bar{B} = 0.1$. (b) Energies for an ellipsoidal nanoparticle with aspect ratio $\alpha = 1.6666$ for different external field strengths $\bar{B} = 0.1$, $\bar{B} = 0.134$, and $\bar{B} = 0.145$. Reprinted from [41]. © IOP Publishing Ltd. All rights reserved.

line can adjust its height rather freely if the height of the surrounding interface changes because the contact angle remains unchanged. When two cylindrical particles approach each other, the energy gain for wetting the surfaces overcomes the costs for the deformation of the surrounding interface, thus the interface forms a capillary bridge between the two ends. The bond-bending energies for cylindrical particles around their preferred tip-to-tip state are very high, with restoring torques up to $T = 10^6 k_B T$ [76]. Therefore, such chains are usually not distorted. Two cylindrical particles may switch to the metastable side-by-side orientation only for bond angles larger than $\phi_c \approx 120$–$140°$, which can be achieved for particulate monolayers under compression or shear stress.

The height of the capillary bridge that forms between two cylindrical particles decreases when the distance between them is increased, compare snapshots for $d/a = 0.9$ with $d/a = 0.3$ in figure 28; it changes also if the particles are tilted with respect to each other, compare snapshots for $d/a = 0.3$ and

$\phi = 0°$, and for $d/a = 0.3$ and $\phi = 20°$. For cylindrical particles, bond bending is not elastic as for ellipsoidal particles, but shows non-elastic hinging behaviour. Therefore, both bond energies and bond-bending energies are significantly affected by deformations of the surrounding interface and by changes of the wetting of the planar faces of the particles. This importance of wetting energy is a qualitative difference for the capillary interactions between ellipsoidal and between cylindrical particles. The crossover between elastic bond-bending and non-elastic hinging can be further explored using superegg-shaped particles with variable edge curvatures, as discussed in [43].
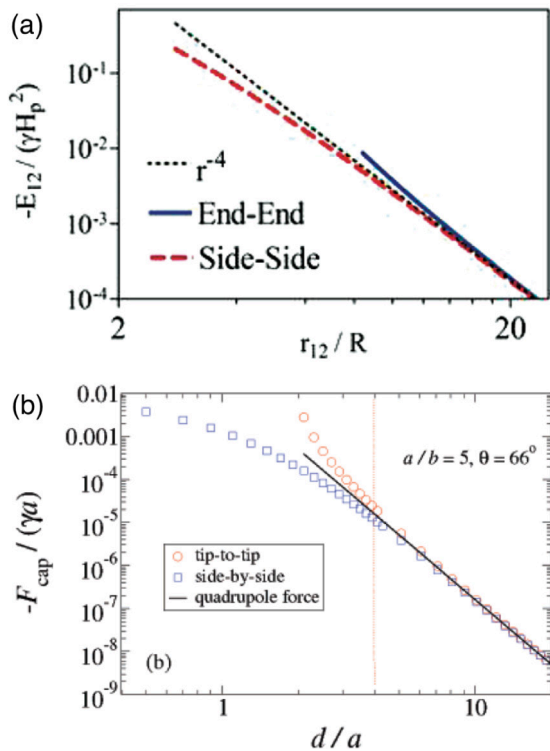
Figure 24. Interaction energies and capillary forces. (a) Interaction energy between two elliptical quadrupoles for two neighbouring cylindrical particles approaching each other in side-by-side and end-to-end orientation. Reprinted with permission from [65]. Copyright (2010) American Chemical Society. (b) Capillary forces evaluated for two similar ellipsoidal particles using superposition of elliptical quadrupoles for aspect ratio 5 and contact angle 66° for varying inter particle separation. Reprinted with permission from [75]. OA CC BY 4.0.

In general, the presence of one particle changes the contact-line position on the other particle. Figure 7(c) shows the deformation of the initially circular contact line around a spherical particle by a nearby ellipsoidal particle. Figure 29 shows that although the spherical particle at a planar interface by itself does not deform the interface and does not induce interface-mediated attraction, an ellipsoidal and a spherical particle mutually attract each other. The attractive interaction between spherical and ellipsoidal particles is larger for side-on configurations of the spherical particles than for tip-on configurations. In both configurations, however, the attraction between spherical and ellipsoidal particles is significantly weaker than the attraction between two ellipsoidal particles with similar sizes that have equal aspect ratios and surface properties.

2.6. Many-particle interactions

Attractive energies for capillary bonds and energy barriers between locally stable configurations are often high, therefore computer simulations show self-assembly in kinetically-trapped dendritic and raft-like structures [114]. Numerical calculations for two-particle, three-particle, and four-particle interactions predict a variety of stable and metastable configurations [77, 115]. Many-particle studies of particles at interfaces can also be extended to polydisperse particle mixtures [116].

Figure 30 shows two locally stable configurations of three ellipsoidal particles. The parallel configuration is globally stable with an energy $E_{par} \simeq -4 \cdot 10^7 k_B T$, but the triangular configuration has a similar energy $E_{tri} \simeq -3.6 \cdot 10^7 k_B T$ for $\theta_c = 65°$, $\gamma_{\ell v} = 0.07$ Nm^{-1}, and ellipsoidal particles with aspect ratio $b/a = 4$ that have been obtained by deformation of spherical particles with $a = 5$ μm [77]. For prolate ellipsoidal particles mostly the side-by-side orientation is observed in experiments, hexagonal networks can be stable if an additional repulsive electrostatic repulsion contributes to the particle-particle interaction. Figure 31(a) shows self-assembly of slightly charged micrometer-sized ellipsoidal particles. The structure initially shows many tip-to-tip contacts; after slow relaxation it compactifies slightly and shows less triangular and more chain-like aggregates in side-by-side orientation after 12 h [113], see figure 31(b). The chains of particles in side-by-side orientation can be thought of as 'colloidal polymers': worm-like chains or rings with bending elasticity.

For non-spherical particles at planar interfaces, particle-particle interactions may affect the orientations of particles and vice versa. For example, cube-like particles at lower interfacial densities assemble on hexagonal and honeycomb lattices in corner-top orientation [97], and at higher interfacial densities on a square lattice in face-top orientation [117]. Figure 32 shows how particle orientations affect interparticle interactions: chains form for prolate ellipsoidal particles that are oriented with their long axes parallel to the interface, while particles disperse homogeneously if they are oriented with their long axes perpendicular to the interface. Particle orientation can be controlled using an external magnetic field [110], see section 2.4.3. A similar tunable (dipolar) interface deformation and therefore tunable capillary interaction can be achieved using magnetic spherical Janus particles [118].

Interface curvature alters particle-induced interface deformations and therefore many-particle self-assembly, see section 2.3.2. In order to systematically understand the interaction of many particles at non-planar interfaces, it is important to study model systems with controlled curvatures [61, 118–121]. For example, spherical particles at interfaces with saddle-like shapes induce quadrupolar interface deformations and therefore at low densities assemble on a square lattice [61], see figure 33(a); at high densities, the optimal packing on a hexagonal lattice is observed. The local lattice structure can be investigated using bond-orientational order parameters,

$$\psi_n = \frac{1}{N_j} \sum_j \exp(in\theta_j), \tag{25}$$

where N_j indicates the number of neighbors of a particle. The angle θ_j is the angle between the bond with a neighboring particle j and an arbitrary reference axis. Figure 33(b) shows that the lattice order switches continuously from square to hexagonal with increasing particle density.

2.7. Particles in ordered fluids

Particles embedded within a nematic liquid crystal (LC) interact with the nematic directors in the vicinity of the colloid and
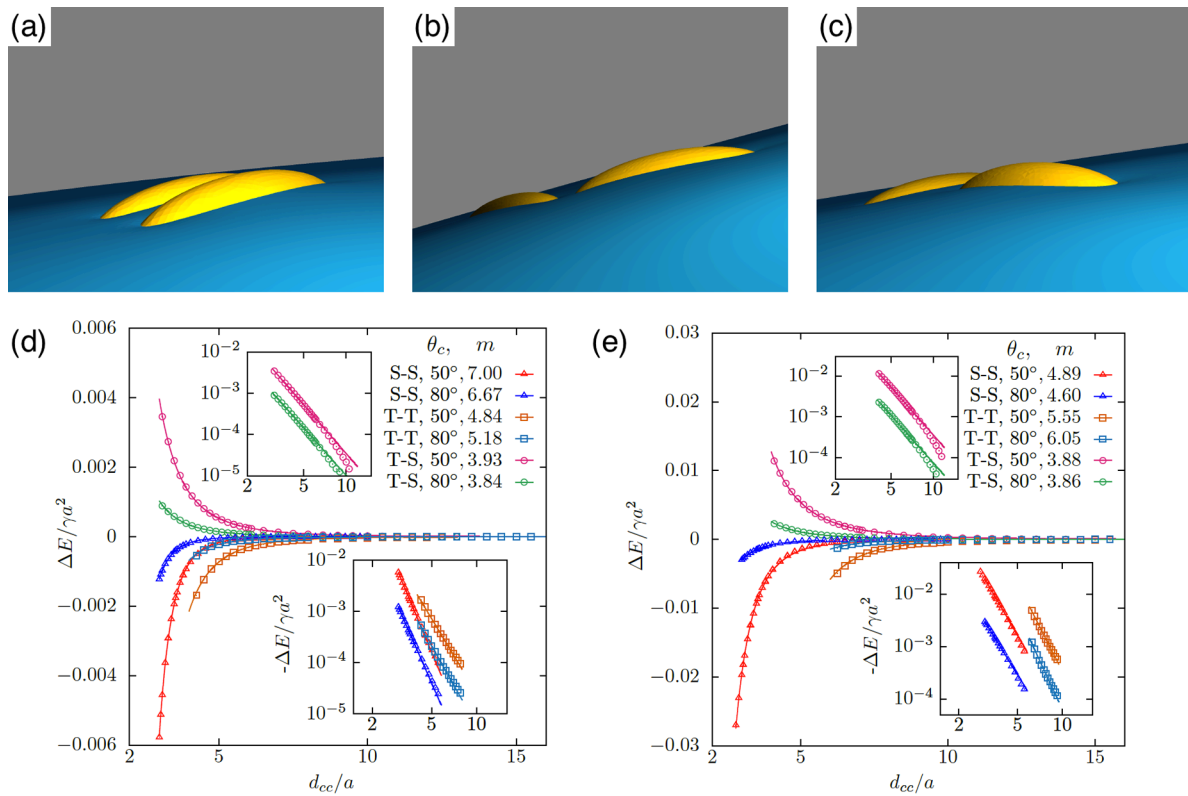
Figure 25. Interface deformations around two ellipsoidal particles with aspect ratios $b/a = 3$ for contact angle $\theta_c = 50°$ in (a) side-by-side, (b) tip-to-tip and (c) tip-to-side orientation calculated using triangulated surfaces. The particles attract each other in side-by-side and tip-to-tip orientation and repel each other in tip-to-side orientation. The side-by-side orientation is energetically most stable. (d-e) Interaction energies $\Delta E/\gamma a^2$ for two identical ellipsoidal particles with aspect ratios (d) $b/a = 2$ and (e) $b/a = 3$ and contact angles $\theta_c = 50°$ and $\theta_c = 80°$. The energies are plotted as function of the distance d_{cc}/a between between the centers of the ellipsoids for side-by-side (S-S), tip-to-tip (T-T), and tip-to-side (T-S) orientation. The interaction is attractive in S-S and T-T orientation and repulsive in T-S orientation. Inset: fit of the numerical data using $\Delta E/\gamma a^2 = k(d_{cc}/a)^{-m}$; the fit parameters are given in the figure. Reprinted with permission from [43]. Copyright (2014) American Chemical Society.

therefore impose boundary conditions on the nematic order parameter at the colloid-LC boundary. This leads to long-ranged anisotropic elastic interactions for spherical and ellipsoidal particles dispersed in nematogenic fluids [122, 123]. Due to varying nature of nematic defects at the colloid-LC boundary, typically elastic multipoles, such as dipoles and quadrupoles, are observed. Large pair interaction strengths render the self-assembled aggregates insensitive to thermal or hydrodynamic fluctuations [124]. Capillary interactions dominate the elastic energies [125]. For microspheres in nematic films, strength and nature of the elastocapillary interactions depend on film thickness and particle size [126]. For small thicknesses of films, giant elastic dipoles occur due to interface distortions. Defects appear around particles, elastic dipoles and nematic elasticity counterbalance the strongly attractive capillary interactions and stabilize particles pairs at finite distance.

Figure 34 shows how cylindrical nanoparticles first assemble at a nematic interface in their energetically favourable tip-to-tip orientation and then align with the nematic director [125]. The weak elastic interactions are able to manifest themselves at flat nematic interfaces, but under curvature gradients again capillarity dominates [125]. Particle anisotropy shall also play a significant role for defect formation at colloid-LC

boundaries and shall thus also control nature and strength of pair-particle interactions. Future experiments and theoretical investigations to elucidate these elusive interplay between capillarity and elasticity are warranted.

2.8. Applications

Applications for (engineered) particles at interfaces range from emulsion stabilisation and colloidosomes to suppression of the coffee-ring effect and froth floatation. In addition to capillary forces, also for example Marangoni flows, surfactants, electric charges, or gravity have to be taken into account.

2.8.1. Pickering emulsions. A classical application is the stabilisation of emulsions. Here, the interactions of particles at interfaces on the mesoscale can be expected to determine macroscopic rheologial properties. In general, the strong adsorption of particles to interfaces leads to thermodynamically stable droplets of oil (water) suspended in water (oil) [1, 3, 127–129]. At low particle concentrations, the mechanism of limited coalescence generates narrow and reproducible droplet-size distributions [117]. Phase inversion of droplet emulsions is obtained by increasing the volume fraction of oil (water). For mixtures for small hydrophilic and
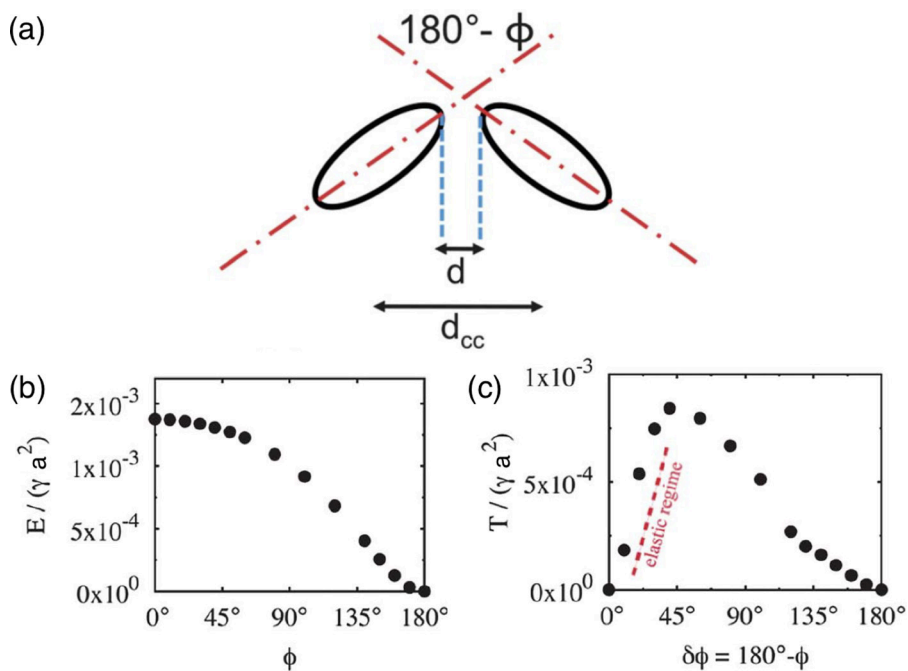
Figure 26. Capillary interaction between two identical ellipsoidal particles. (a) Definition of the parameters. ((b), (c)) Bond-bending energies E and torques T as function of the deviation from the stable side-by-side orientation for two ellipsoids with $b/a = 3$ and $\theta_c = 80°$. A linear-elastic regime for the torques is found for bond angles $\phi < 40°$. Adapted from [76] with permission of The Royal Society of Chemistry.
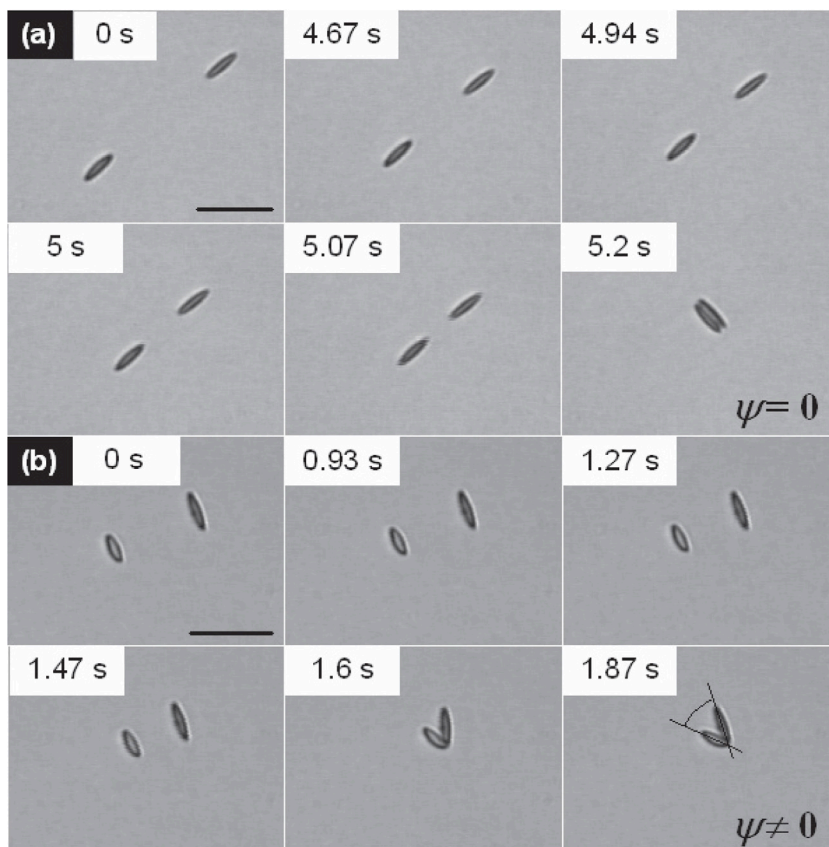
Figure 27. Two ellipsoidal particles approaching side-by-side with (a) equal and (b) dissimilar shapes. Equal particles assemble with their long axes parallel, ellipsoidal particles with different sizes form a capillary arrow. Reprinted with permission from [112]. © EPLA. All rights reserved.

hydrophobic particles also sponge-like, bicontinuous phases and non-spherical colloidosomes have been observed [4, 130]. Particles with anisotropic surface functionalization, such as Janus particles, can be used as amphiphilic colloidal surfactants [131, 132]. Particle-stabilised emulsions are used for example in food and cosmetic industries [8–11].

2.8.2. Colloidosomes. Colloidosomes are solid capsules engineered with controlled permeability and mechanical strength that can have sizes from sub-micrometers to millimeters [133]. The capsules are prepared by self-assembly of colloidal particles to emulsion droplets that are then locked together for example using sintering or electrostatic binding of an oppositely-charged polyelectrolyte. This ensures that the shells remain intact when they are transferred to a different fluid. With the help of centrifugation, the particles are typically transferred into a solvent that is identical to the internal phase. Colloidosomes can be used for encapsulation of drugs, proteins, vitamins, flavors, gas bubbles, and even living cells.

2.8.3. Suppression of the coffee-ring effect. Particles that are homogeneously dispersed over an entire drop often form ring-like deposits when the drop evaporates, so-called 'coffee rings' [134]. Addition of ellipsoidal particles with aspect ratio 3.5, obtained by deforming spherical particles with $a = 0.65\ \mu$m, to droplets that contain the spherical particles has been found to lead to more homogeneous deposition [135]. For droplets that contain ellipsoidal particles only, a strong suppression of the coffee ring effect is already observed for very moderate aspect ratios $b/a \approx 1.5$. Numerical calculations predict capillary attraction between spherical and ellipsoidal particles [43]; the uniform deposition may therefore be caused by capillarity-induced cluster formation. Applications for that a more uniform deposition of the material instead of 'coffee rings' may be desired are inkjet printing, fabrication of micro- and nanostructures, and coating.

2.8.4. Froth floatation. Froth floatation is used to separate minerals from gangue. The separation efficiency depends on both the particle-bubble attachment and the froth stability [80, 136]. While the particle-bubble attachment can be adjusted using collector chemicals that modify the particle's surface properties, the film stability is affected by particle shape. One complication that decreases froth stability can be particles with sharp edges [79]. Therefore, a systematic understanding of the interaction of non-spherical particles with thin films and potentially also of immersion forces may help to improve froth floatation [80, 98, 102, 136].

3. Particles at biological interfaces

Particles adsorb at biological interfaces, often called membranes, because of an adhesion strength w between the particles and the membranes. In addition to the adhesion strength, the minimal ingredients required to study spherical particles are the bending ridigity κ and the tension γ of the membranes, and the radius a of the particles. For small particles, molecular
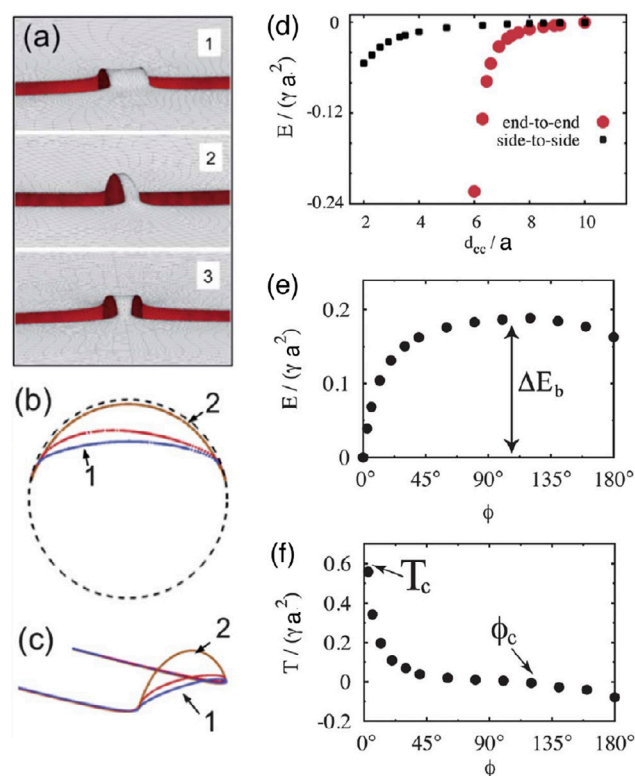
Figure 28. Near-field interaction between two cylindrical particles of aspect ratio $b/a = 3$ for contact angle $\theta_c = 80°$. (a) Interface shape for the shortest distance between to cylinders $d = 0.9a$ and $\phi = 0°$ (configuration '1'), $d = 0.3a$ and $\phi = 0°$ (configuration '2'), $d = 0.3a$ and $\phi = 20°$ (configuration '3'). The light (grey) and dark (red) surfaces are the vapor–liquid and liquid-solid interfaces, respectively. Visualization of the solid-vapor interface has been disabled to allow examination of the meniscus between the cylinders. (b) Contact line profiles at the end face of each cylinder. (c) Perspective views of the contact line profiles shown in (b). (d) Capillary energy versus center-to-center separation for ellipsoids. In this figure, the value of the energy for $d = 10.0a$ is taken as reference. (e) Capillary energy versus bond angle for ellipsoids in contact. (f) Capillary torque corresponding to the energy in (e), as a function of the angular deviation from the stable side-to-side configuration. Adapted from [76] with permission of The Royal Society of Chemistry.

interactions are important. Coarse-grained or even atomistic computer simulations are used to investigate theoretically translocation through and incorporation within membranes [142–145]. Experimentally, the interaction of small particles with membranes can be investigated using a combination of microfluidic devices, fluorescence microscopy, and electrophysiological measurements [146], by scattering techniques [147], and by quartz crystal microbalance and AFM [148]. For larger particles with radii $a > 20$ nm, wrapping is the dominant mechanism of the interaction between particles and membranes, as will be discussed in detail in this section. Particles that interact with membranes can be engineered and are found in biological systems with a wide variety of sizes, shapes, and surface functionalizations, see figure 35.

Comparing the different energetic contributions, large spherical nanoparticle adhesion and wrapping is determined by two characteristic crossover radii,
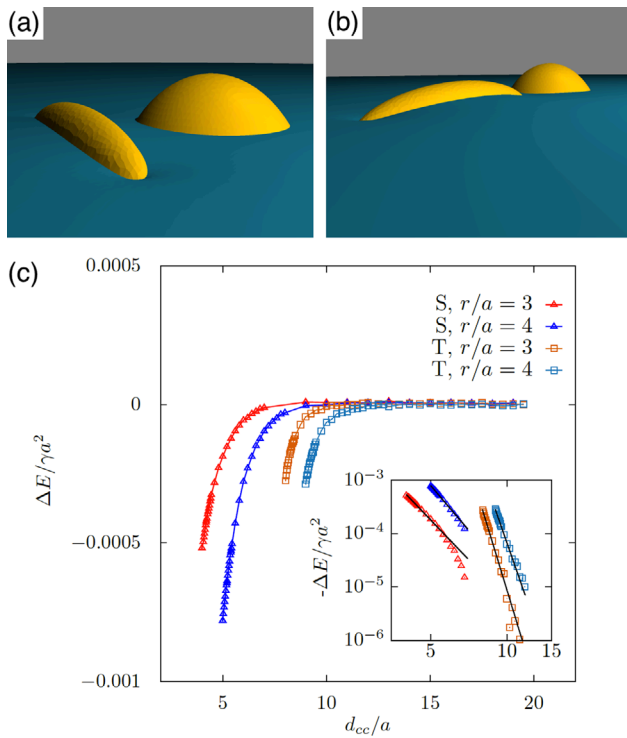
Figure 29. Interaction of a spherical particle with an ellipsoidal particle of aspect ratio $b/a = 5$. The contact angle $\theta_c = 48.47°$ has been used for both particles. The energies are plotted for spherical particles with radii $r = 3a$ and $r = 4a$ that approach the ellipsoidal particle (a) at the side (b) and at the tip, here shown for a spherical particle with $r = 3a$. (c) Interaction energies $\Delta E/\gamma a^2$ as function of d_{cc}/a between the centers of mass of the particles. Inset: double-logarithmic plot and the fit of the numerical data to a power-law decay. Reprinted with permission from [43]. Copyright (2014) American Chemical Society.

$$a^*_{\kappa\gamma} = \sqrt{\frac{2\kappa}{\gamma}} \quad \text{and} \quad a^*_{\kappa w} = \sqrt{\frac{2\kappa}{w}}. \tag{26}$$

The radius $a^*_{\kappa\gamma}$ that compares the bending energy with the membrane tension characterizes the crossover between the bending-dominated regime for particles with $a < a^*_{\kappa\gamma}$ and the tension-dominated regime for larger particles. While for nanoparticles bending energy is thus the main player, for micrometer-sized particles tension plays the dominant role. Within the bending-dominated regime, small particles with $a < a^*_{\kappa w}$ remain unwrapped, while larger particles get wrapped, determined by the subtle balance of bending and adhesion energy [139, 149–151]. For given particle radius, the threshold adhesion strength $w^* = 2\kappa/a^2$ therefore marks the transition between the unwrapped and the complete-wrapped regime.

Adhesion may be mediated by van der Waals interaction [152], hydrophobic interaction [152], electrostatic interaction [153], and specific adhesion via receptor-ligand bonds [154–160]. In biological media, nanoparticles can be surrounded with a corona of proteins that effectively changes their surface properties [161–166]. Throughout this section, we assume that the adhesion can be modeled by a continuous and mostly homogeneous adhesion strength, which is appropriate for many systems, but not always sufficient for
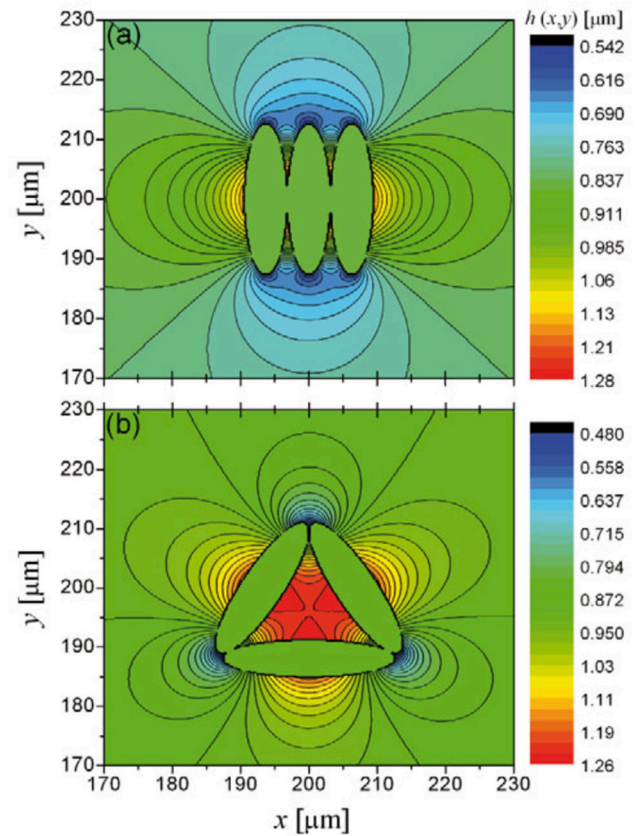

Figure 30. Computed contour plots of $u(x, y)$ in the case of three contacting equal ellipsoids. The energy of the side-by-side configuration (a) is a bit lower than that of the triangular one (b). The ellipsoidal particles with aspect ratios $b/a = 4$ have been fabricated by deforming spherical particles with $a = 5\ \mu m$; $\theta_c = 65°$, and $\gamma = 0.07\ Nm^{-1}$. Reprinted from [77] with permission. 2011 © EDP Sciences, SIF, Springer-Verlag.

systems dominated by receptor-ligand bonds and electrostatic interactions. Typical values for the bending rigidity are $20\,k_BT < \kappa < 100\,k_BT$, for the membrane tension $0.05\,k_BT\ nm^{-2} < \gamma < 20\,k_BT\ nm^{-2}$ [149, 167], and for the adhesion strength $2 \cdot 10^{-6}\,k_BT\ nm^{-2} < w < 0.2\,k_BT\ nm^{-2}$ [42]. Instead of the absolute values for energy, tension and adhesion strength, it is often convenient to use dimensionless, reduced values, e.g. $\tilde{E} = E/(\pi\kappa)$, $\tilde{\gamma} = \gamma a^2/\kappa$, and $\tilde{w} = 2wa^2/\kappa$.

An overview of both single-particle and many-particle systems at membranes is provided in this section. In sections 3.1–3.4 we focus on various aspects of the interaction of single particles with membranes, while in sections 3.5 and 3.6 we discuss two-particle and many-particle interactions, respectively. Section 3.7 focuses on particles at membranes with spontaneous curvature. We finally discuss applications in section 3.8.

3.1. Spherical particle-induced membrane deformation

For a spherical particle and an infinitely large tensionless membrane, the membrane surrounding the particle assumes a catenoidal shape, see figure 36(a). This shape is found around all cylindrically-symmetric, 'conical' membrane inclusions,
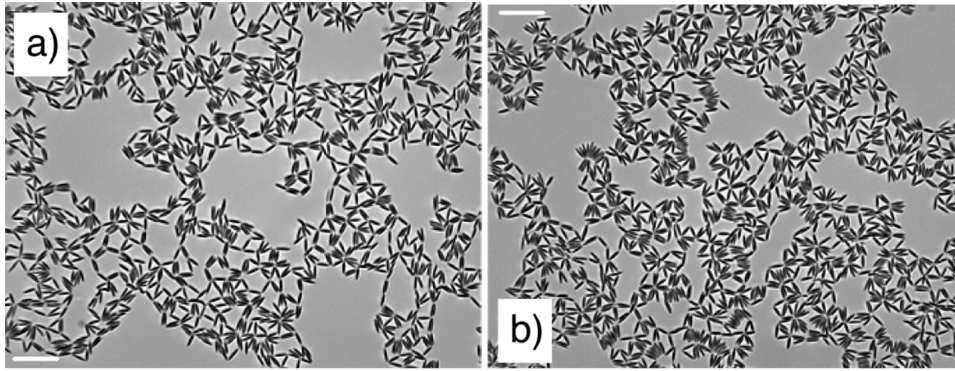
Figure 31. Self-assembly of ellipsoids with low surface charge at higher surface coverage on a water-decane interface. (a) Initial structure. (b) After 12 h. The aspect ratio of the ellipsoids is 5.5. The scale bar corresponds to 50 μm. Reprinted with permission from [113]. Copyright (2009) American Chemical Society.
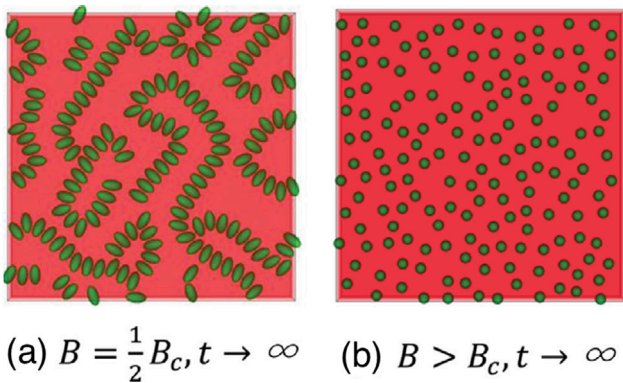
$$\text{(a) } B = \frac{1}{2}B_c, t \to \infty \quad \text{(b) } B > B_c, t \to \infty$$

Figure 32. Ellipsoidal magnetic microparticles at interfaces. The neutrally-wetting particles (contact angle $\theta_c = 0°$) are initially distributed randomly in their equilibrium orientations with surface fraction $\phi = 0.38$. (a) Applying a magnetic field parallel to the interface normal, **H**, causes them to self-assemble due to dipolar capillary interactions. (b) Once the critical dipole field strength B_c is reached, the particles transition to the vertical state, halting dipolar capillary interactions. The particles randomly redistribute if magnetic dipole-dipole and van der Waals interactions are weak compared with thermal fluctuations. Reprinted with permission from [110]. OA CC BY 3.0.

which includes curved proteins [140, 169, 170] and attached polymers [171–174]. A catenoid is a minimal surface with vanishing mean curvature at every point and therefore with vanishing bending energy. The deformation energy cost for the membrane adhered to the particle and the adhesion energy gain for contact between particle and membrane can therefore be directly compared with each other in order to predict whether a particle gets wrapped or not. The wrapping transition is fully characterized using the critical particle radius $a^*_{\kappa w}$ for wrapping in equation (26). However, in general the deformation energy of the membrane surrounding a particle will contribute to the total deformation energy of the membrane.

A convenient way to characterize wrapping states of particles for various parameters are wrapping diagrams based on energy minimisation, analogous to phase diagrams in thermodynamics [139, 149, 175], see figure 36(b). Spherical particles remain unwrapped below a threshold adhesion strength and get partial-wrapped or complete-wrapped for higher adhesion strengths. Particles at membranes with finite tension can be found in

stable partial-wrapped states for adhesion strengths just above those for the binding transitions, see figure 36(b). The stable partial-wrapped states are separated by continuous transitions from the unwrapped states and by discontinuous transitions from the complete-wrapped states. The latter transitions with energy barriers are associated with two spinodals that indicate those values for the adhesion strength beyond which particles transition spontaneously from partial-wrapped to complete-wrapped states and below which particles transition spontaneously from complete-wrapped to unwrapped states.

3.2. Membrane deformation by non-spherical particles

Membrane deformations induced by non-spherical particles depend on both particle shape, discussed in this section, and particle orientation, discussed in section 3.4. In general, inhomogeneous surface curvature of particles corresponds to energy barriers for wrapping [139, 176]. For non-spherical particles, membrane tension is therefore not required to stabilize partial-wrapped states; such particles are ideal membrane markers for imaging. Thus not only size and aspect ratio, but also local particle surface curvature matters for wrapping of non-spherical particles [176].

The importance of local particle surface curvature can be demonstrated well for Hauser's cube-shaped particles. The phase diagram in figure 37 shows that no membrane deformation energy costs arise if cube-like particles attach with a flat face to a membrane. The particles therefore adhere already for very small adhesion strengths and are found in shallow-wrapped states. The first energy barriers are encountered between shallow-wrapped and deep-wrapped states when the membrane has to bend around the highly-curved edges to increase wrapping from one face to five faces. The energy barriers between deep-wrapped and complete-wrapped states correspond to the last four edges to be wrapped. Both energy barriers shift to higher adhesion strengths for higher values of the membrane tension.

3.3. Field-induced membrane deformation

We discuss here particles within the hydrophobic tail region of lipid bilayers in part 1 and particles at curved membranes in part 2.
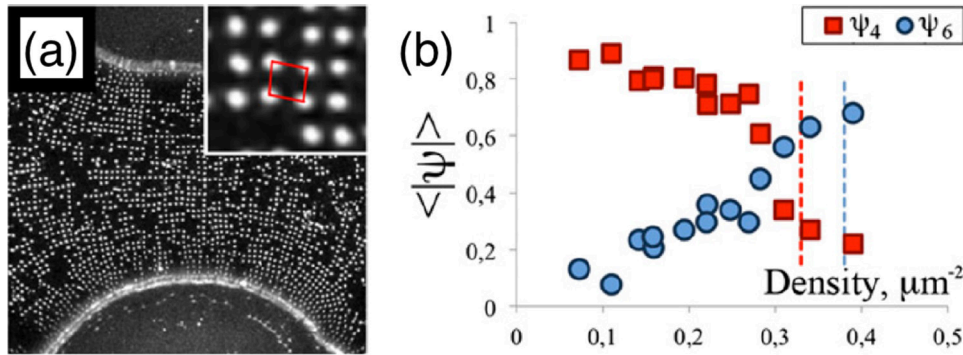
Figure 33. Transition from square to hexagonal packing at high particle densities. (a) Part of a dumbbell-shaped droplet covered with colloidal particles at relatively low density ($0.16 \, \mu m^{-2}$). The particles organize in a square pattern with a bond-orientational order parameter for four-fold symmertry $\langle |\psi_4| \rangle = 0.81$ and a bond-orientational order parameter for six-fold symmetry $\langle |\psi_6| \rangle = 0.2$. (b) Bond order parameters for four- and sixfold symmetry as a function of particle density for interfaces with deviatoric curvature $D = |k_1 - k_2|/2 = 0.006 \, \mu m^{-1}$. The red and blue vertical dashed lines indicate maximum densities for a particle separation of $1.74 \, \mu m$ in a square and a hexagonal lattice, respectively. Reprinted with permission from [61].
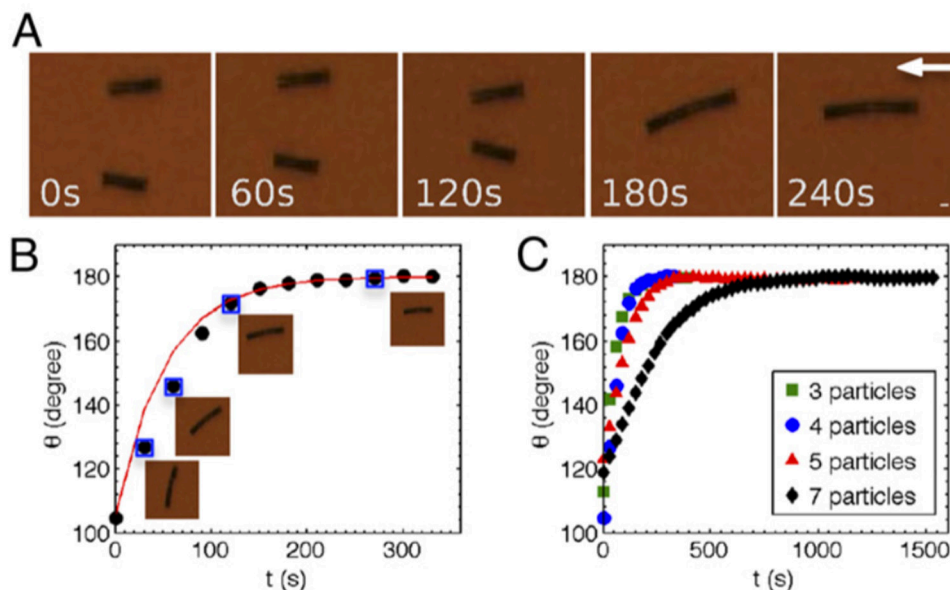

Figure 34. Particles at interfaces of ordered fluids. (a) Upon forming a rigid chain, the aggregate rotates such that the chain axis aligns parallel to the director field. Arrow indicates the direction of LC alignment. The scale bar represented by the arrow corresponds to $10 \mu m$. (b) Elastic rotation rate of a chain comprising four particles. (c) Rotations observed on the interface for chains of three, four, five, and seven particles in length. Reprinted with permission from [125].

3.3.1. Particles within membranes. Particles with sizes of few nanometers may incorporate themselves in membranes and locally distort both lipid order and membrane thickness [142, 145, 177], see figure 38(a). While lipid order can only be investigated on the molecular scale, thickness variations can also be investigated using continuum models. Here the headgroup positions of the monolayers can be modeled by mathematical surfaces with bending rigidity and monolayer tension, and a confinement potential which maintains the lipid bilayer thickness.

Analogous to integral membrane proteins with hydrophobic mismatch [178–181], particles that locally induce membrane-thickness deformations experience short-ranged deformation-mediated interactions. While the interactions may be repulsive at long distances as predicted by the continuum models, both continuum models and molecular dynamics simulations predict short-ranged attractive interactions and therefore clustering of nanoparticles within membranes. For high membrane tensions, the energy barrier for a third particle approaching a pair of particles is considerably decreased, such that particle aggregation may occur spontaneously [145], see figures 38(b) and (c).

3.3.2. Curved membranes. Not only particle shapes, also membrane curvature prior to wrapping has to be taken into account for the interaction of particles with membranes. This can be demonstrated by calculating entry of particles into and exit of particles out of vesicles with different curvatures, see figure 39. The vesicles are assumed to freely adjust volume but keep a fixed membrane area. Vesicles without particles thus adopt an overall spherical shape that is then locally distorted by binding a nanoparticle. The adhesion strength w and
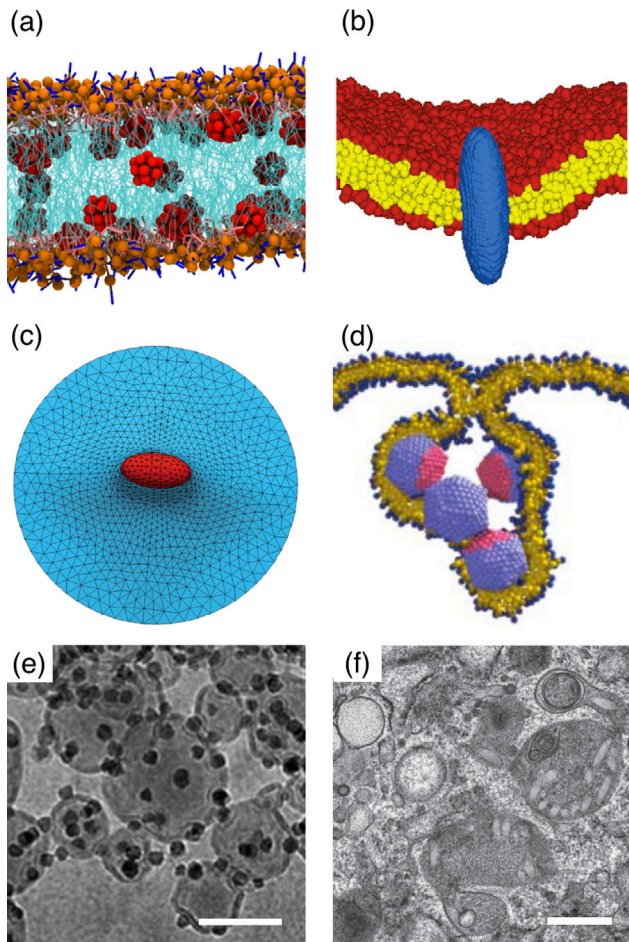
Figure 35. Interaction of nanoparticles with membranes. (a) Incorporation. Fullerenes in a POPC membrane. Adapted with permission from [137]. Copyrighted by the American Physical Society. (b) Penetration. An ellipsoidal nanoparticle passes through a lipid bilayer. Adapted by permission from Macmillan Publishers Ltd: *Nat. Nanotechnol.* [138], copyright © 2010. (c) Wrapping. An ellipsoidal nanoparticle gets wrapped by a lipid bilayer membrane. Reproduced from [139] with permission from the Royal Society of Chemistry. (d) Cooperative wrapping. Capsids bud cooperatively. Adapted by permission from Macmillan Publishers Ltd: Nature, [140], copyright © 2007. (e) Cryo-TEM micrographs of nanoparticles interacting with vesicles. The scale bar corresponds to 100 nm. Adapted from [51] with permission of The Royal Society of Chemistry. (f) TEM micrographs of nanoparticles internalized in human mesenchymal stem cells. The scale bar corresponds to 500 nm. Adapted with permission from [141]. Copyright © 2012 Wiley-VCH Verlag GmbH & Co. KGaA, Weinheim.

the relative curvature of particle and vesicle $c_r = a/R_v$, for vesicles with radius R_v, are the relevant parameters to characterize this system. They are a subset of the full parameter space, determined in addition by membrane spontaneous curvatures and by osmotic pressures [183].

For particles that enter vesicles from the outside, $c_r > 0$, wrapping is hindered by an energy barrier. For particles that exit vesicles from the inside, $c_r < 0$, upon increasing the adhesion strength the particles continuously transit from the free state via stable partial-wrapped states with increasing wrapping fractions to the complete-wrapped state. Partial-wrapped particles can be used as probes for the local membrane curvature [184]. A direct and barrierless transition between the free and
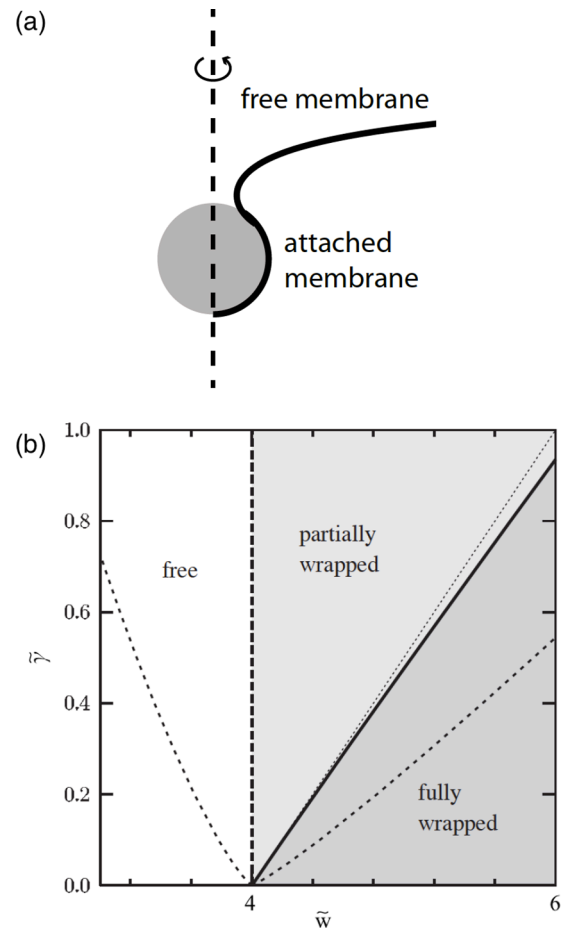
Figure 36. Wrapping of a spherical nanoparticle for various reduced adhesion strengths $\tilde{w} = 2wa^2/\kappa$ and membrane tensions $\tilde{\gamma} = \gamma a^2/\kappa$. (a) The membrane deforms in a cylindrically symmetric way around the symmetry axis and the shape can be described by a radial deformation profile. For an infinitely large tensionless membrane, the shape of the free membrane is catenoidal. (b) The wrapping phase diagram shows that the nanoparticles are unwrapped below a critical adhesion strength $\tilde{w} = 4$, and completely enveloped for adhesion strengths beyond the thick solid line. The thin dotted line is the envelopment transition calculated neglecting the deformation energy of the free membrane. The thin dashed lines are the spinodals for spontaneous unwrapping from the complete-wrapped to the free/non-wrapped state and for spontaneous envelopment from the partially wrapped to the fully wrapped state. Adapted with permission from [168]. © EPLA. All rights reserved.

the complete-wrapped state is only present for particles at infinitely large planar membranes. With decreasing absolute relative curvature c_r, both the energy barriers for particle entry as well as the stability of partially-wrapped states for particle exit decrease. The adhesion strengths for the wrapping transitions can be well approximated by the instability relations [42, 183] $w_1^* = 2(1 + c_r)^2 \kappa/a^2$ and $w_2^* = 2(1 - c_r/\sqrt{1 - c_r^2})^2 \kappa/a^2$, as indicated in figure 39.

3.4. Non-spherical shapes, surface heterogeneities, and particle orientations

For non-spherical particles, the orientation of particles at membranes—in addition to particle shapes, sizes, and surface properties—has to be taken into account to determine
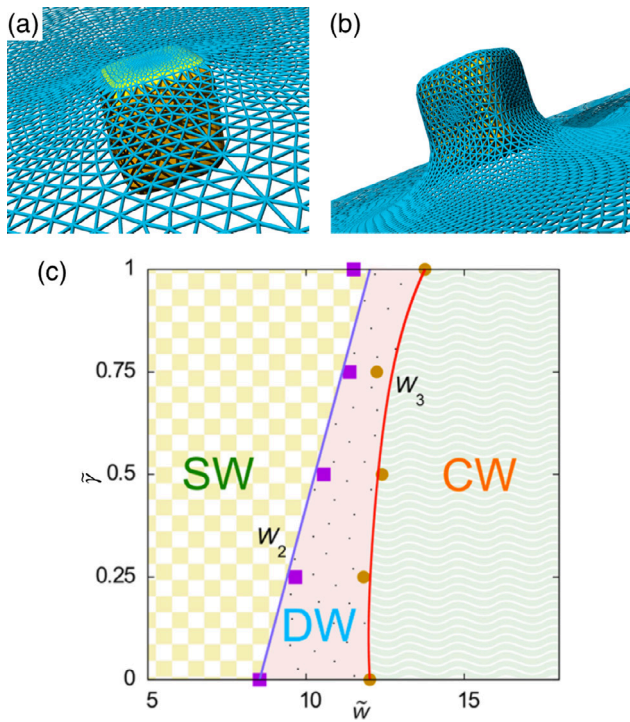
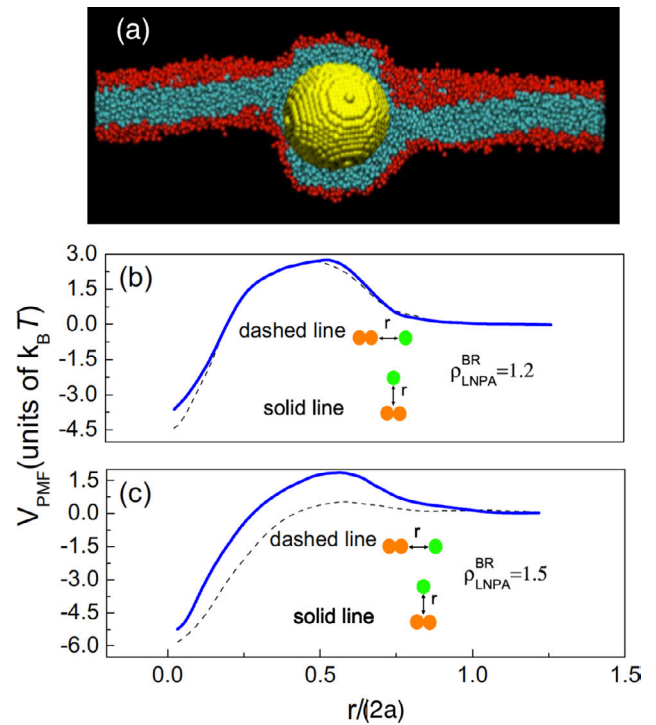**Figure 37.** Wrapping of cube-like nanoparticles. (a,b) Membrane deformation for wrapping of Hauser's cube. The network of edges and triangles describes the membrane shape and is used for the numerical calculations of the curvature energy. Membrane conformations are shown at fixed membrane tension $\tilde{\gamma} = 0.50$ for two corresponding states at the W_2 phase boundary: (a) a shallow-wrapped state with approximately 10% of particle wrapped, and (b) a deep-wrapped state with approximately 80% of the particle wrapped. (c) Phase diagram for wrapping of Hauser's cube for reduced membrane tension $\tilde{\gamma} = \gamma a^2/\kappa$ and reduced adhesion strength $\tilde{w} = wA/(2\pi\kappa)$, where A is the particle surface area. We find a shallow-wrapped (SW), a deep-wrapped (DW), and a complete-wrapped (CW) state, separated by two discontinuous wrapping transitions, labeled as W_2 and W_3. Adapted with permission from [176]. Copyright (2014) American Chemical Society.

Figure 38. Hydrophobic nanoparticles interacting with membranes. (a) Simulation snapshot of a single nanoparticle radius $a = 6$nm incorporated in a lipid membrane for lipid area density $\rho_{\text{LNPA}}^{\text{BR}} = 1.5$. ((b), (c)) Calculated potential of mean force V_{PMF} profiles as a third nanoparticle approaches a fixed nanoparticle cluster formed by two identical nanoparticles with radius $a = 5$ nm at (b) high membrane tension (lipid area density $\rho_{\text{LNPA}}^{\text{BR}} = 1.2$) and at (c) low membrane tension (lipid area density $\rho_{\text{LNPA}}^{\text{BR}} = 1.5$). Adapted with permission from [145]. Copyright (2014) the American Physical Society.
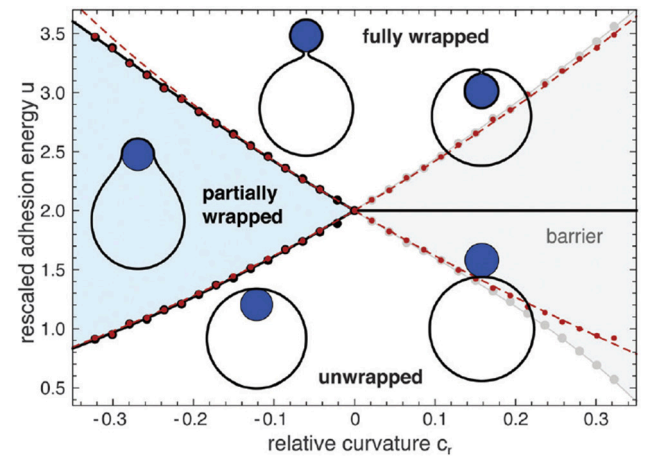
wrapping states and membrane deformations. Elongated particles can be oriented in rocket and in submarine orientation, with their long axes perpendicular and parallel to the membrane, respectively. Janus particles preferably bind with their most adhesive side to the membrane. Changing the orientation of particles in magnetic fields can be used to probe the elastic properties of membranes and cells.

3.4.1. Elongated particles. The orientations of elongated particles at membranes crucially depend on particle shapes, membrane elastic properties, and membrane-particle interactions, see figure 40. Table 4 summarizes wrapping states and transitions for various particles shapes and membrane elastic parameters based on the results of [139, 149, 176, 185].

For prolate ellipsoidal particles, the particles bind to membranes with their points of lowest curvature at the sides of the particles. In these shallow-wrapped states, they are in the so-called 'submarine orientation'. For fast wrapping, if reorientation does not occur, the particles remain in submarine orientation until they reach the complete-wrapped state [139]. For

Figure 39. Morphology diagram of stable states of a particle adhering to a vesicle. The wrapping state is plotted for various values of rescaled adhesion energies $u = wa^2/\kappa$ and relative curvatures c_r of the vesicle membrane and the particle surface. The three black lines divide the diagram into three regions in which the particle is either partially wrapped, unwrapped, or fully wrapped. In the grey shaded region, the transitions between the unwrapped state and the wrapped state of a particle outside the vesicle require the crossing of an energy barrier. The red dashed lines are analytical instability lines derived from the stability relations in [42]. Reproduced from [183].—Published by The Royal Society of Chemistry. OA CC BY 3.0.
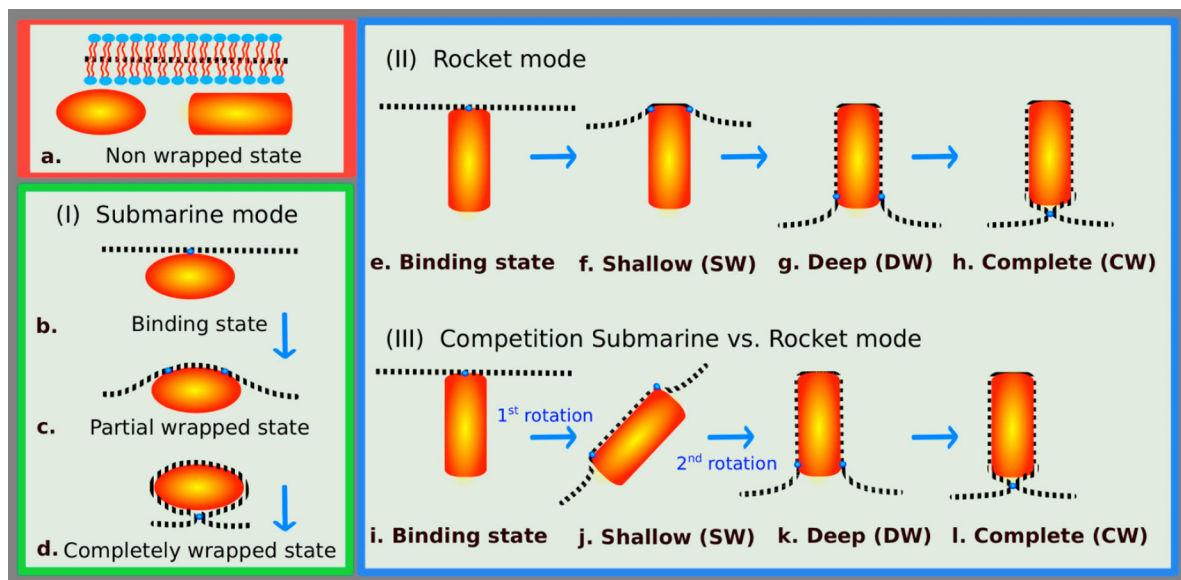
Figure 40. Modes of entry for nanoparticle uptake by membrane wrapping: (I) submarine mode with the long axis of the particles oriented parallel to the membrane, (II) rocket mode with the long axis oriented perpendicular to the membrane, and (III) competition between submarine and rocket mode as observed for rod-like particles with high aspect ratios. The complete-wrapped particle is connected by an infinitely small catenoidal neck to the membrane; the particle orientation in this state is irrelevant. Reprinted with permission from [176]. Copyright (2014) American Chemical Society.

Table 4. Shape dependence of particle wrapping, based on the results of [139, 149, 176, 185]. The membrane can be characterized by bending rigidity only, 'κ', or by bending rigidity and membrane tension, 'κ and γ'; the binding transition can occur at finite or vanishing adhesion strength w; the particle can be in submarine or rocket orientation; transitions can be continuous (cont.) or discontinuous (discont.) and may involve reorientation (reorient.). The binding transition for ellipsoids is independent of the membrane tension and is given in [139, 185].

Particle shape	Membrane	Binding transition	Shallow-wrapped state	Deep-wrapping transition	Deep-wrapped state	Envelopment transition
Spherical	κ	cont., for $w = 2\kappa/R^2$	—	—	—	$\equiv$ binding
Spherical	κ and γ	cont., for $w = 2\kappa/R^2$	yes	—	—	discont.
Ellipsoidal	κ, κ and γ	cont., indep. of γ	yes, submarine	discont., reorient.	yes, rocket	cont.
Ellipsoidal[a]	κ, κ and γ	cont., indep. of γ	yes, submarine	—	—	discont.
Cube-like	κ, κ and γ	at vanishing w	yes	discont.	yes	discont.
Sphero-cylinder	κ, κ and γ	at vanishing w, rocket	yes, submarine	discont., reorient.	yes, rocket	discont.
Rod-like	κ, κ and γ	at vanishing w, rocket	yes, submarine	discont., reorient.	yes, rocket	discont.
Rod-like[a]	κ, κ and γ	at vanishing w, rocket	yes, submarine	—	—	discont.
Rod-like[b]	κ, κ and γ	at vanishing w, rocket	yes, rocket	discont.	yes, rocket	discont.

[a] Fast wrapping at high adhesion strength, such that a bound ellipsoid cannot reorient to rocket orientation.
[b] Rocket mode for supereggs with blunt tips and small aspect ratio (e.g. $n = 4$ and $b/a = 1.5$).
Reprinted with permission from [176]. Copyright (2014) American Chemical Society.

slow wrapping, the particles are able to reorient to their minimal-energy states at every time, they transit from submarine orientation to the so-called 'rocket orientation' at deep wrapping. The rocket state is energetically preferable at deep wrapping, because only one of the pointed tips needs to be wrapped. From a stable deep-wrapped state, ellipsoidal particles then continuously transition to the complete-wrapped state [176].

For rod-like particles, energy minimisation predicts that the particles readily bind with their blunt tips in rocket orientation at very small adhesion strengths. If the edges of the particles are sharp and their aspect ratios are small, the particles remain in rocket orientation until they reach complete wrapping; the transitions between shallow-wrapped and deep-wrapped, as well as between deep-wrapped and complete-wrapped states are discontinuous. For high aspect ratios or round edges of the particles, rod-like particles bind with their blunt tips in rocket orientation only with a very small fraction of their surface area. They then rotate to submarine orientation in the shallow-wrapped state, and back to rocket orientation in the deep-wrapped state [176, 186], see figure 40. In particular, the theoretical prediction for the rotation from submarine orientation to rocket orientation is in agreement with experimental observations for budding of filamentous viruses [28, 29].

The dynamics of wrapping of spherical nanoparticles is determined by the typical time scales for the relevant processes, such as membrane deformation [170], receptor or protein diffusion that may be hindered by a cortical cytoskeleton [187–191], and potential metabolic remodeling of the cytoskeleton [192–194]. After initial contact between nanoparticles and membranes, the deformed area of the membrane surrounding the particles increases until half wrapping and then again decreases. While the membrane deformation is catenoid-like for small and for large wrapping fractions of particles, for finite membrane size the highest deformation energy costs are expected for about half-wrapped particles. Formation of a defect in the neck towards the end of the wrapping process can induce the separation of bent and flat membrane and completes wrapping [186].

The reorientation dynamics for elongated particles can be calculated using molecular dynamics simulations for nanoparticles that interact with initially flat lipid bilayer membranes [186, 195]. Also local free-energy analysis and incremental changes of the nanoparticle orientation in the direction of lowest energy at each time step allow to predict the wrapping pathway [186]. In figure 41, the corresponding curvature-energy landscapes are displayed. A spherocylindrical nanoparticle that is initially oriented in the unfavourable rocket orientation first reorients towards submarine orientation. However, although energetically most favourable until half wrapping the particle may never actually reach submarine orientation. Beyond half wrapping, the particle turns back to the then favourable rocket orientation, in agreement with the energetics discussed at the beginning of this section.

3.4.2. Janus particles.

We are not aware of systematic experimental studies for the interaction of lipid-bilayer membranes with nanoparticles that have anisotropic surface functionalization. However, micrometer-sized spherical particles that are half coated with ligands preferably orientate with the ligand-coated side towards the membrane during phagocytosis [196]. Furthermore, viruses have been modeled as partially adhesive particles [140]. The reorientation of the malaria parasite in tip-first orientation at the beginning of the invasion process may also be due to an adhesive gradient on the parasite surface [22]. Analytical calculations for partial-wrapped particles, e.g. Janus particles, at non-spherical vesicles show that membrane curvature-induced forces pull the particles to regions with preferred membrane curvature [197].

3.4.3. Magnetic particle rheology.

In analogy to magnetic particles with switchable orientation at fluid interfaces, micrometer-sized magnetic particles can also be attached to cell membranes with an underlying cytoskeleton [198]. Such microrheological measurements reveal glassy behaviour for various cell types [198–201]. For red blood cells with their cortical spectrin cytoskeleton responsible for the shear elasticity of the complex cell membrane [202], the values of the elastic parameters obtained using magnetic particle microrheology agree well with those used for computer simulations for cell stretching and blood flow [37].
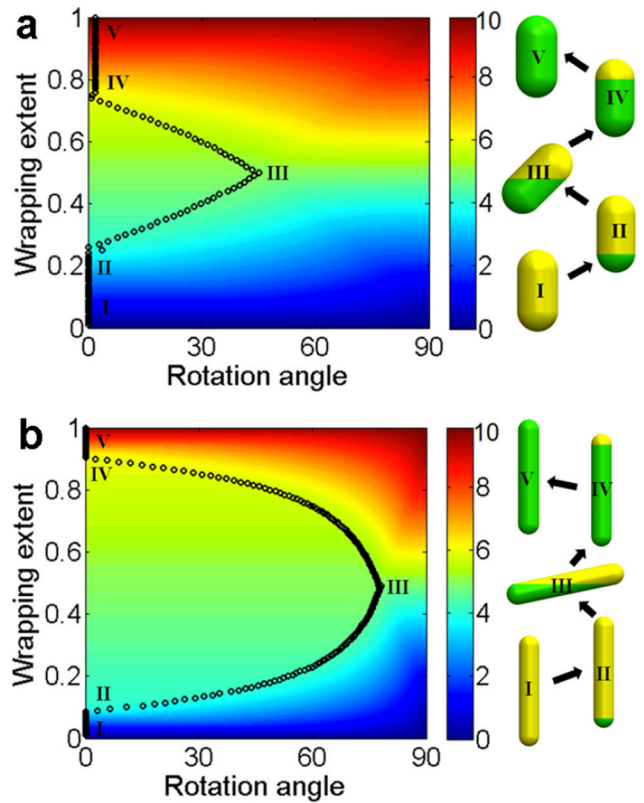
Figure 41. Endocytic pathways for spherocylindrical nanoparticles with aspect ratios (a) $b/a = 2$ and (b) $b/a = 5.5$ predicted by local energetics. The nanoparticles take a general laying-down-then-standing-up sequence during endocytosis. The heat maps show the curvature energy for various particle orientation angles and wrapping fractions. Nanoparticle wrapping at the turning points (I–V) along the endocytic pathways predicted by local free-energy analysis is schematically shown on the right: green-shaded areas are wrapped, while yellow-shaded areas are naked. Reprinted with permission from [186]. Copyright (2013) American Chemical Society.

3.5. Long-range membrane-mediated interactions

Membrane deformations induced by partial-wrapped particles lead to membrane-mediated interactions that minimise the sum of both membrane deformation energy and particle-membrane attachment energy [203]. Several recent studies are discussed in this section. However, much more is known—and this knowledge may partially be transferred to nanoparticles—about the related systems of lipid bilayer-mediated interactions between curved inclusions, both for membrane-deformation mediated interactions [48, 140, 169, 170, 204], as well as for membrane-fluctuation mediated Casimir interactions [205–206].

3.5.1. Far-field interactions.

Membrane-mediated interaction between two parallel and long cylindrical particles at distance d attached to the same side of membranes under lateral tension is repulsive [208],

$$V(d) = -\frac{(\kappa + 2a_{cyl}^2 w)^2 (1 + \tanh(\xi d/2))}{4(\gamma\kappa)^{1/2} a_{cyl}^2},\qquad(27)$$
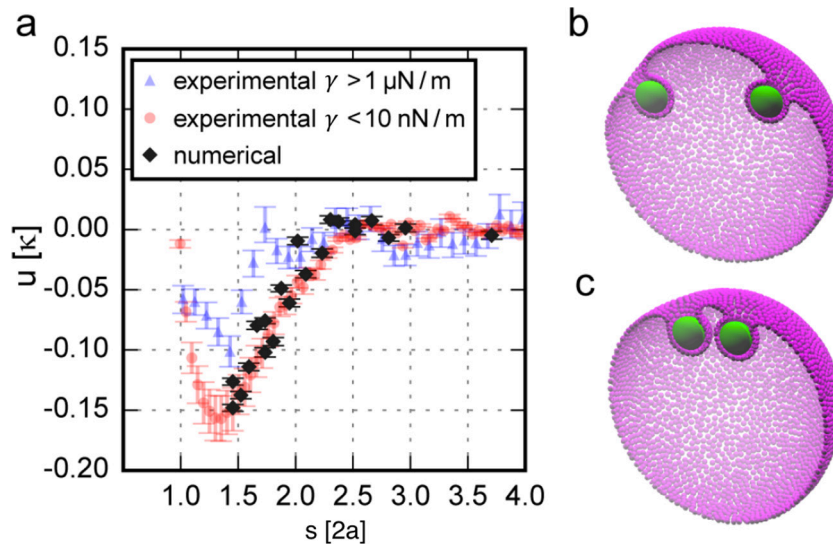
Figure 42. Interaction potentials between two partial-wrapped particles. (a) The numerical results are displayed together with the experimental results, which are rescaled by the bending rigidity $\kappa = 20.9 \pm 2.5\,k_\mathrm{B}T$ [207] and the particle radius $a = 1.96 \pm 0.06\,\mu m$. ((b)–(c)) Simulation snapshots for two particles (green) adhered to a coarse-grained vesicles (magenta) at separations (b) $s = 7.4\,a$ and (c) $s = 3.0\,a$. The membrane vertices are plotted using small spheres. Adapted with permission from [44]. CC BY 4.0.

where $\xi = \sqrt{\gamma/\kappa}$ is a characteristic reciprocal length, and a_cyl is the cylinder radius. The interaction between two cylindrical particles attached to opposite sides of the membrane is attractive,

$$V(d) = -\frac{(\kappa + 2a_\mathrm{cyl}^2 w)^2 (1 + \coth(\xi d/2))}{4(\gamma\kappa)^{1/2} a_\mathrm{cyl}^2}. \qquad (28)$$

Here, the length of the cylinders is contained in the parameters for the bending rigidity, adhesion strength, and membrane tension for these effectively one-dimensional calculations. Results for stronger membrane deformations can be found in [209].

Only few studies are available for far-field interactions between spherical nanoparticles that are partially attached to lipid bilayer membranes. Figure 42 shows both numerical calculations and experimental data. Membrane-mediated particle attraction is found for distances below $5\,a$, with an attractive energy well of $E_\mathrm{A} \approx -0.17\,\kappa$ for an interparticle distance of about $2.8\,a$ [44]. For typical lipid bilayer bending rigidities $20\,k_\mathrm{B}T < \kappa < 100\,k_\mathrm{B}T$, this corresponds to binding energies $-3.4\,k_\mathrm{B}T > E_\mathrm{A} > -17\,k_\mathrm{B}T$. The figure shows larger attraction strengths for membrane tensions $\gamma < 10$ nN/m compared with membrane tensions $\gamma > 1\,\mu$N/m.

Many computer simulation studies for membrane-mediated interactions between partial-wrapped nanoparticles, as shown in figure 42, rely on finite-element calculations. Here, the bending energy is discretized on triangulated surfaces [210–213]. Large systems that require at the same time fine discretization in high-curvature regions around particles are computationally expensive, therefore membrane-mediated interactions between the particles have so far mostly been studied in the near field. However, long-ranged membrane-mediated

interactions between partial-wrapped nanoparticles might be similar to long-ranged interactions between curved inclusions. For example, for two spherical-cap inclusions attached to the same side of planar membranes, the repulsive membrane-mediated interaction is [169]

$$V(d) = 4\pi\kappa(\alpha_1^2 + \alpha_2^2)\frac{a^4}{d^4} + O(d^{-5}), \qquad (29)$$

where α_1 and α_2 are polar angles that determine the sizes of the spherical caps, a is their radius, and d is the distance between the centers of the caps. Strongly-curved inclusions at very close distances experience an attractive interaction [48].

3.5.2. Near-field interactions. Interactions between two (spherical) nanoparticles have been shown to be attractive, see e.g. figure 42. This is surprising on the first view, because catenoid-like membrane deformations around partial-wrapped nanoparticles at large distances require only very small deformation-energy costs. If two spherical-cap inclusions or two particles approach each other on a planar membrane the ideal catenoid-like deformations cannot form any more because of the boundary conditions. Therefore, the membrane-mediated interactions because of deformation-energy are expected to be repulsive [169, 204]. However, for spherical particles the attractive membrane-mediated interactions because of membrane-particle adhesion energy dominate and lead to an overall attraction [203].

For two partial-wrapped particles in the near field, not only the interparticle distance, but also the orientation of the pair of particles with respect to the membrane has to be taken into account. For example, in [46] the connecting line between two particles adsorbed to a vesicle is parallel to the membrane at large distances and reorients to perpendicular orientation
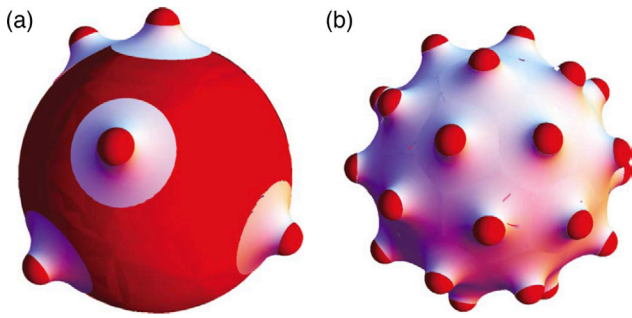
Figure 43. Spherical-cap inclusions on vesicles. (a) Inclusions, indicated by small red caps, on a vesicle at low density. White membrane patches indicate catenoidal deformations with vanishing bending energy around the inclusions. (b) An inclusion-decorated vesicle with vanishing total bending energy at optimal inclusion density. Reprinted with permission from [170]. Copyright (2009) by the American Physical Society.

at small distances. The attractive interaction is significantly higher for this particularly stable tubular arrangement [214].

3.6. Many-particle interactions

Many-particle interactions are important for membrane-mediated interactions, which has been demonstrated in several cases for integral membrane proteins with hydrophobic mismatch and for spherical-cap inclusions [140, 170, 182, 215]. It is therefore essential to not only consider pair interactions between particles. We start our discussion with the 'inclusion case', i.e. with membrane deformation-mediated interactions only, where the membrane area attached to each particle is fixed. While two weakly-curved spherical-cap inclusions that are attached to the same side of the membrane repel each other as discussed in section 3.5.1, many inclusions have been observed to aggregate and to induce bud formation [140, 170, 215–217]. A membrane that is curved prior to adhesion of inclusions or that gets curved by cooperative budding screens the repulsive interaction and can therefore lead to effective attraction. Figure 43 highlights catenoidal membrane deformations around inclusions on vesicles; the size of the catenoidal 'halo' shrinks with increasing background curvature, thereby screening the repulsive interaction between the inclusions. These catenoidal patches reduce the total bending energies of the vesicles, which vanish at optimal inclusion density. In comparison, on planar membranes curved inclusions always increase the deformation energy.

A particle dimer switches from a linear aggregate on the membrane to a tubular aggregate for increasing wrapping fraction [46, 47], compare also section 3.4 for the orientation of elongated particles. On a vesicle, the wrapping fraction can be tuned by adjusting the reduced volume of the vesicle, $v = V/V_{sph}$, where V is its actual volume and V_{sph} is the volume of a spherical vesicle with the same membrane area. A small reduced volume also allows more than two particles to join the tube. The energy gain of such tubular assemblies compared with single, complete-wrapped particles strongly depends on the ratio of the range ρ of the particle-membrane interaction potential and the particle radius a. The finite potential range
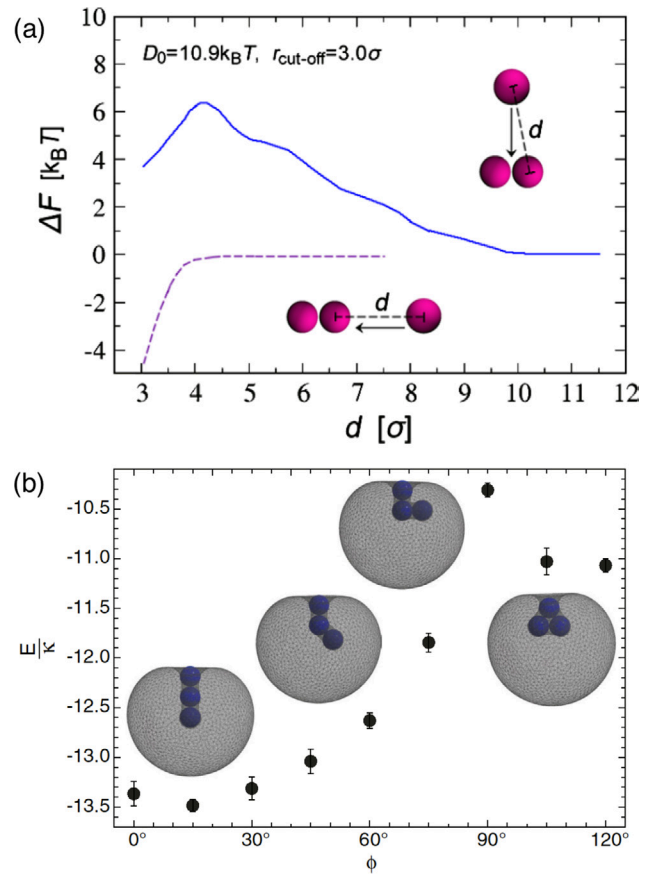
Figure 44. Membrane-mediated interactions between three spherical particles. (a) Total energy as a function of the separation when a third particle approaches a fixed dimer along the direction of the dimer's axis (dashed line) and perpendicular to it (full line). In both cases $\kappa = 20\,k_BT$ and $\sigma_{np} = 3\,\sigma$ has been used, where σ is the diameter of spherical hard beads used to model the membrane. Reprinted with permission from [203]. Copyright (2012) by the American Physical Society. (b) Rescaled total energy E/κ of a vesicle with three adsorbed particles bound together by membrane tubes as a function of the angle ϕ between the particles for the reduced volume $v = 0.88$ and the rescaled adhesion energy $wa^2/\kappa = 2$. The membrane area of the vesicle is $A_v = 485a^2$. Here, $\phi = 0°$ corresponds to a linear arrangement of the particles. The four snapshots depict minimum-energy conformations at the angles $\phi = 0°, 45°, 90°,$ and $120°$. Reprinted with permission from [46]. Copyright (2012) by the American Physical Society.

leads to a higher adhesion energy gain for tubular arrangements compared with single-particle buds, because some fraction of the tubular necks between particles are inside the interaction range; for example the energy gain per particle is about $5\,\kappa$ for $\rho/a = 0.2$ [214].

Simulation snapshots and energies for several configurations of three particles attached to membranes are shown in figure 44. If the particles are all located in the plane of the membrane, a third particle that attaches to form a linear aggregate gains membrane-mediated binding energy of few k_BT and attaches without an energy barrier. In contrast, a particle that attaches from the side to the existing particle aggregate experiences an energy barrier and has a few k_BT higher energy in the (metastable) bound state compared with the unbound state. Bending energy has been shown to favour compact aggregation,
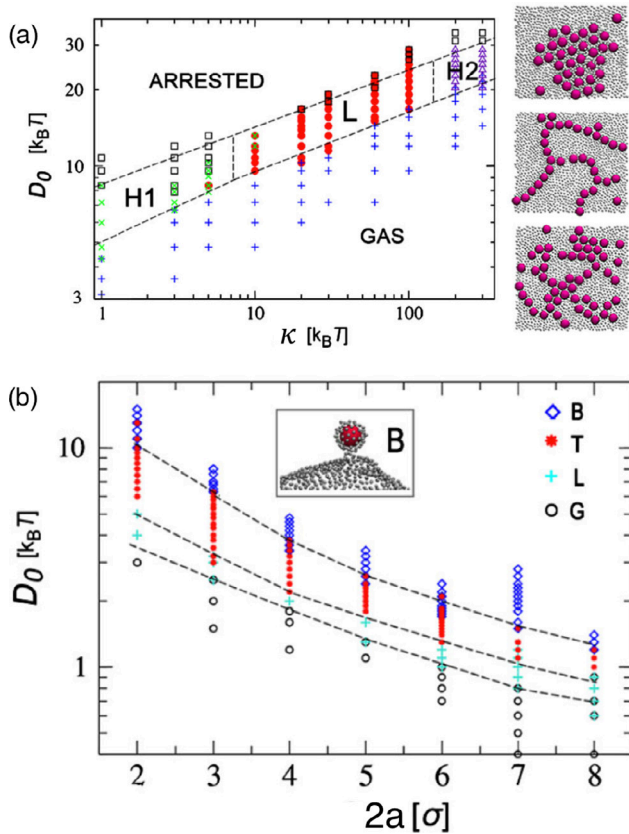
Figure 45. Membrane-mediated interactions between many particles. (a) Phase diagram for nanoparticle self-assembly in terms of membrane bending rigidity κ and particle-membrane binding energy D_0, which replaces the adhesion strength w in the simulations. The snapshots show typical aggregates in the H1, the L, and the H2 phase (top to bottom). Adapted with permission from [203]. Copyright (2012) by the American Physical Society. (b) Phase diagram in terms of nanoparticle diameter $2a$ and D_0. With increasing D_0, the gaseous phase G with non-attached particles is followed by the linear aggregation phase L, the tube-formation phase T, and the single-particle bud phase B. The radius of the vesicle is $R_v = 30\sigma$ and the particle surface fraction is 0.15. Adapted with permission from [47]. Copyright (2012) by the American Physical Society.

adhesion energy linear aggregation [203]. Also for tubular aggregates, the linear-tube configuration is preferred over the more compact, triangular configuration [46], see figure 44(b). Linear aggregates in the plane of the membrane have been experimentally observed for colloidal particles bound to giant unilamellar vesicles (GUVs) [218], tubular aggregates for the interaction of viruses with cells and GUVs [219].

Figure 45(a) shows a phase diagram for many-particle systems in terms of bending rigidity κ and particle-membrane binding energy D_0 [203]. In the limit of small bending rigidities, partial-wrapped particles form a hexagonal cluster phase where the membrane penetrates in-between the particles. In the limit of high bending rigidities, the particles are barely attached to the membrane. They deform the membrane only weakly, therefore they also interact only weakly and are found in loose, mostly hexagonal aggregates. Linear aggregates are observed inbetween both limites for biologically relevant bending rigidities $10\,k_BT < \kappa < 100\,k_BT$. Figure 45(b) shows
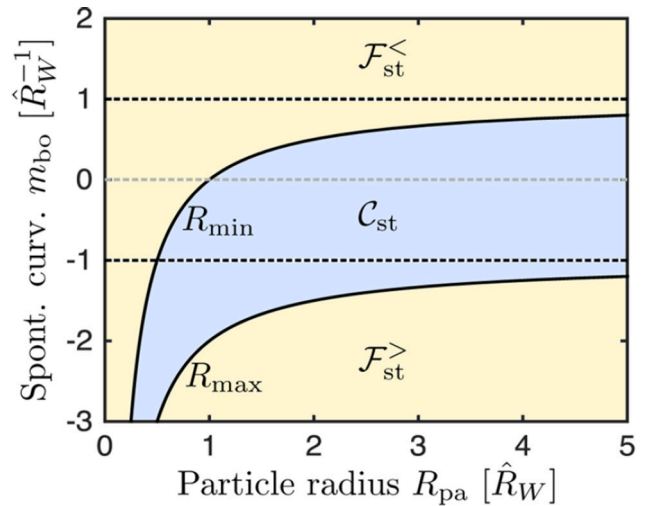

Figure 46. Engulfment regimes for weakly curved mother membranes as a function of particle radius $R_{pa} = a$ and spontaneous curvature $m_{bo} = c_0$ of the membrane segment bound to the nanoparticle. Both quantities are given in units of the modified adhesion length $\hat{R}_W = \sqrt{2\kappa/w}$. The direction of negative spontaneous curvature coincides with direction of the curvature of the particle surface. Complete-wrapped states $\mathcal{C}_{st}$ (blue) are found between the two regimes with non-wrapped states, $\mathcal{F}_{st}^<$ and $\mathcal{F}_{st}^>$ (yellow). The phase boundaries are given by $R_{pa} = 1/(\hat{R}_W^{-1} - m_{bo})$ for $m_{bo} < 1/\hat{R}_W$ and $R_{pa} = 1/(|m_{bo}| - \hat{R}_W^{-1})$ for $m_{bo} < -1/\hat{R}_W$. Reprinted with permission from [42]. Copyright (2015) American Chemical Society.

a phase diagram in terms of particle diameter and particle-membrane binding energy. Free unbound nanoparticles are found at low adhesion strengths and for small particle radii, then linear aggregates, tubular aggregates, and single-particle buds are observed with increasing adhesion strength [47]. This sequence of configurations is consistent with the reorientation reported for elongated nanoparticles in [176], see section 3.4.

3.7. Membranes with spontaneous curvature

Biological membranes are often not symmetric, the two monolayers usually consist of different lipids. This asymmetry can be modeled with the help of a spontaneous curvature c_0 of the membrane. If the directions of spontaneous curvature and the curvature of the particle surface coincide, the spontaneous curvature facilitates complete wrapping compared with a symmetric membrane [42]. At the same time, the direct transition between free and complete-wrapped states is replaced by a discontinuous transition. For a spontaneous curvature opposite to the curvature of the particle surface, the complete-wrapped state is shifted to higher adhesion strengths. Furthermore, a new regime with partial-wrapped states is found. With increasing spontaneous curvature, also the regime of adhesion strengths where partial-wrapped states are stable increases.

For fixed adhesion strengths, finite spontaneous curvatures lead to size selectivity for wrapping of nanoparticles, see figure 46. For vanishing or small spontaneous curvatures, all particles with radii beyond a threshold radius get
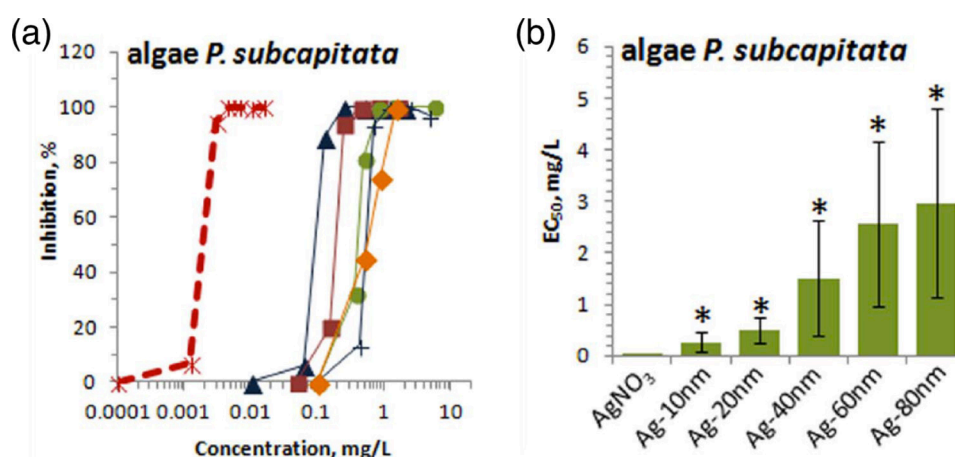
Figure 47. Dose-response curves and respective EC_{50} values of Ag formulations to test algae. (a) Dose-response curves ((red) AgNO$_3$, (blue,triangle) Ag nanoparticles with size 10 nm, (brown) 20 nm, (green) 40 nm, (blue, +) 60 nm, (orange) 80 nm) and (b) EC_{50} values for algae P. subcapitata, a very sensitive test organism. Reprinted with permission from [19]. CC BY 4.0.
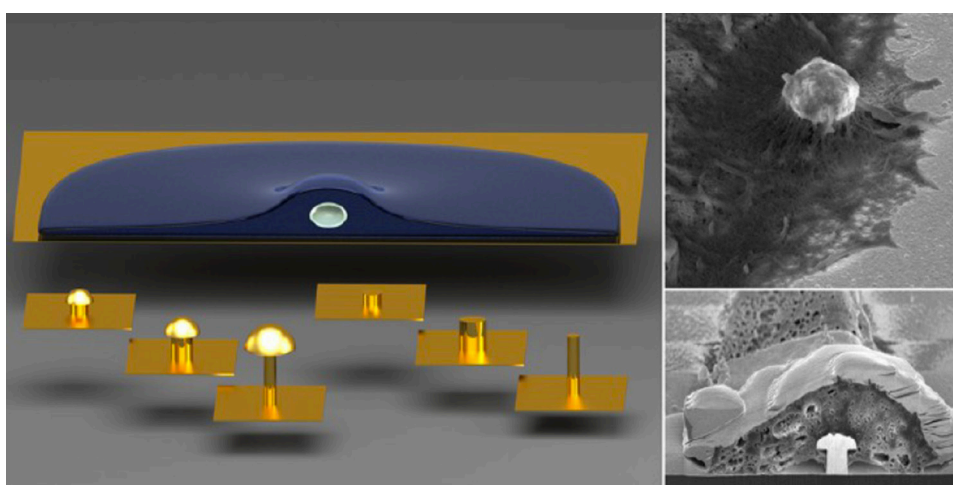
Figure 48. A cardiomyocyte cell interfacing with cylindrical and mushroom-shaped gold nanopillars. Focused ion-beam cuts of cells that engulf mushroom-shaped pillars show the shape of the lipid-bilayer membranes. Reprinted with permission from [231]. Copyright (2014) American Chemical Society.

wrapped, see equation (26). With decreasing spontaneous curvatures, in addition to the lower threshold radius for complete wrapping, also an upper threshold radius beyond the that particles remain unwrapped is found [42]. The regime with stable complete-wrapped states thus narrows to a small window in the particle radius for high negative values of the spontaneous curvature. Such a preferred radius for particle wrapping has been observed in experiments [220, 221]. Size selectivity by spontaneous membrane curvature is therefore an alternative to receptor-based models for cellular uptake that are usually used to motivate an upper limit for the particle radius to achieve complete wrapping [154].

3.8. Applications

On the one hand, particle-membrane systems can be used for applications in therapeutics and diagnostics. On the other hand, for numerous other applications in industry,

potential toxic effects have to be considered. Furthermore, nanostructured surfaces can be rationalised as nanoparticles bound to a substrate, which opens an entire new field for applications. For basic research, particle-membrane systems can serve as model systems to understand biological processes, such as viral budding, malaria invasion, and phagocytosis.

3.8.1. Drug delivery. Nanoparticles are potential drug-delivery vectors and tools for diagnosis [222–226]. For diagnosis, in particular non-spherical nanoparticles with enhanced stability of partial-wrapped states can serve as membrane markers for imaging [141]. For drug delivery, rough hydrophobic particles have been proposed to have a high drug-carrying capacity and high loading efficiency [227]. Such particles can prolong the time of release of a drug payload, which can be therapeutically advantageous. Nanoparticles may even cross the blood-brain barrier via transcytosis and may therefore be applied for drug delivery in the brain [228, 229]. Recently hollow shell-shell nanocontainers with stimuli-responsive
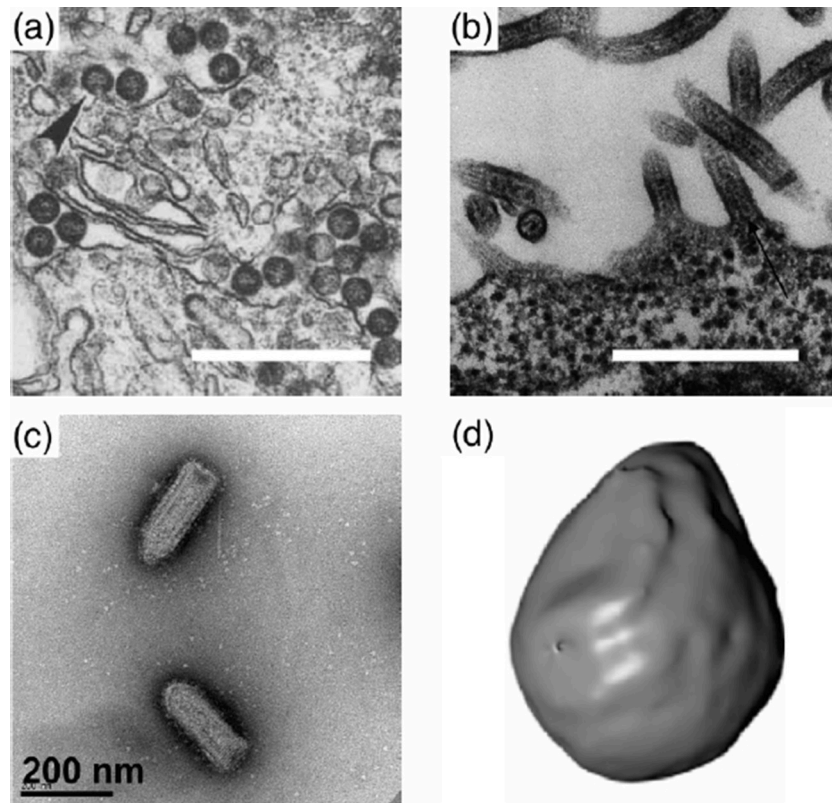
Figure 49. Viruses and parasites. (a) Rift valley feaver viruses in primary rat hepatocytes. The length of the scale bar corresponds to 600 nm. Adapted from [234], with permission from Elsevier, Copyright (1987). (b) Virus-like particles as seen in nucleocapsids of Ebola virions, about to bud. The length of the scale bar corresponds to 500 nm. Reprinted with permission from [28]. CC BY 4.0. (c) Vesicular stomatitis virus (VSV). The length of the scale bar corresponds to 200 nm. Reprinted with permission from [235]. CC BY 4.0. (d) An isosurface-rendered malaria parasite. Reprinted with permission from [22]. CC BY 4.0.
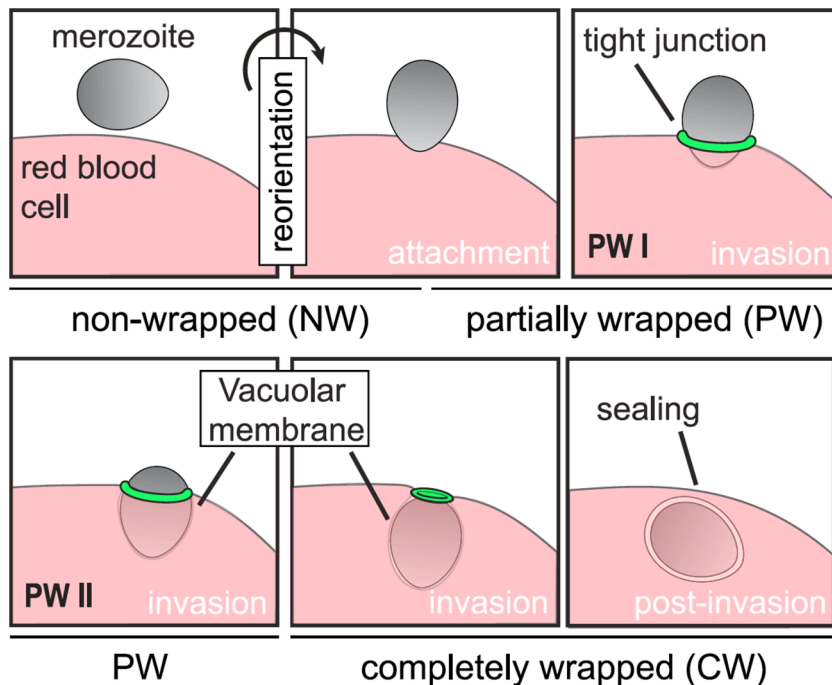
Figure 50. The stages of merozoite invasion. Schematic representation depicting different wrapping phases of the merozoite from reorientation through to invasion and postinvasion. Reprinted with permission from [22]. CC BY 4.0.
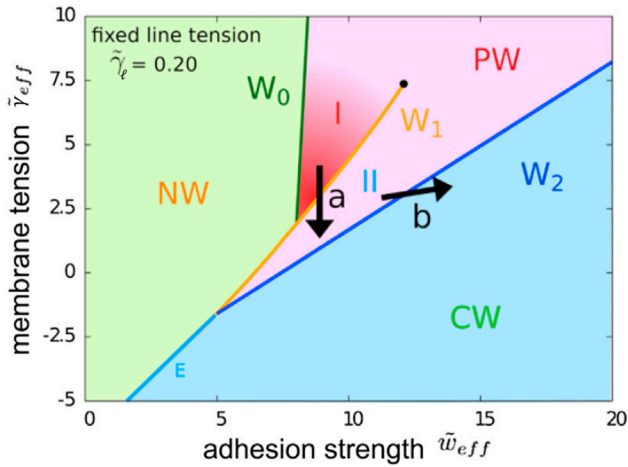
Figure 51. Wrapping phase diagram for a tip first-oriented merozoite for fixed reduced line tension $\tilde{\gamma}_{\ell} = \gamma_{\ell}a/(2\kappa) = 0.20$ and several values of effective adhesion strength and effective membrane tension: non-wrapped merozoites (NW), partial-wrapped merozoites with small (PW I) and high wrapping fractions (PW II), and complete-wrapped/fully invaded merozoites (CW), see figure 50. The transition W_0 is a continuous transition, whereas the transitions W_1, W_2, and E are associated with energy barriers. The transition W_1 ends at a critical point where the difference between PW I and PW II vanishes. The spontaneous curvature c_0 can be combined with the membrane tension and the adhesion strength to an effective membrane tension, $\tilde{\gamma}_{\text{eff}} = \tilde{\gamma} + \tilde{c}_0^2/(aH_0)^2$, and an effective adhesion strength, $\tilde{w}_{\text{eff}} = \tilde{w} + c_0$, respectively. The critical point is indicated by a black point. Here, $\tilde{c}_0 = c_0 a^2 H_0$, $\tilde{\gamma} = \gamma a^2/(2\kappa)$, $\tilde{w} = wH_0 4\pi a^2/(2\kappa)$, where $H_0 = \int_{\text{merozoite}} \text{d}S\, H / \int_{\text{merozoite}} \text{d}S = 2.5/a$ and a is the radius of a sphere with the same surface area as the meozoite. Modified with permission from [22]. CC BY 4.0.

properties that could allow for controlled drug release have been suggested for drug delivery [230].

3.8.2. Nano-Toxicity. For studies of potential toxic effects, not only single-particle properties, such as composition and size, but also particle concentrations play an important role [19]. Toxicity can be quantified by EC_{50} values that refer to the concentration of particles that induce a response of cells or organisms halfway between the base line and the maximum after 72 h exposure time to nanoparticles. While $AgNO_3$ leads to growth inhibition for algae already at concentrations of 10^{-3} mg l^{-1}, Ag nanoparticles lead to growth inhibition only at concentrations between 0.1 mg l^{-1} and 1 mg l^{-1}, see figure 47. Most other organisms are less sensitive to nanoparticles and growth inhibition occurs only at higher particle concentrations compared with algae. In general, the EC_{50} values increase significantly with particle size, which means that the toxic effect is reduced. For mammalian cells they range from $c_{EC50} \approx 2$ mg l^{-1} for 10 nm Ag particles to $c_{EC50} \approx 35$ mg l^{-1} for 100 nm Ag particles, for *E. coli* bacteria from $c_{EC50} \approx 0.3$ mg l^{-1} for 10 nm Ag particles to $c_{EC50} \approx 3$ mg l^{-1} for 100 nm Ag particles.

3.8.3. Nanostructured surfaces. Multi-electrode arrays allow to electrically couple excitable cells to electronic devices, see figure 48. The challenge is to achieve an optimal coupling, which requires to minimize the cleft between the cell and the electrode and to achieve tight attachment of the cell to the substrate in general. While thin electrodes pierce cell membranes [232], micro-electrodes get wrapped [231, 233]. A systematic study of different micro-electrode shapes reveals that mushroom-shaped pillars are engulfed more than cylindrical pillars without caps [231]. Furthermore, cells have been found to preferably engulf pillars in their center compared with their edge. Quantitative evaluation of focused ion-beam cuts allows to extract normal cytoskeletal stresses between few Pa for cylinders with caps and several hundred Pa for cylinders without caps.

3.8.4. Viral budding, malaria invasion, and phagocytosis. Passive endocytosis of particles with a homogeneous adhesion strength between particles and membranes is often modified by specific adhesion and active processes for biological systems. Figure 49 shows viruses with different shapes and a malaria parasite that have similar sizes as the particles discussed earlier. One specific example for active wrapping is the invasion of the malaria parasite into an erythrocyte, see figure 50. Reorientation of the parasite, possibly because of a gradient of adhesive molecules, is followed by invasion. During invasion, a tight junction forms and reseales the membrane, which completes the formation of the parasitophorous vacuole.

For the egg-like shape of the malaria parasite, line tension at the tight junction, and anisotropic adhesion of the parasite leads to a complex phase diagram for passive endocytosis with stable non-wrapped, shallow-wrapped, deep-wrapped, and complete-wrapped states [22], see figure 51. As indicated in figure 51, secretion of unstructured membrane from the parasite and favourable spontaneous curvature of the erythrocyte membrane may help the parasite to overcome energy barriers for wrapping and to finally invade the cell. In addition, also motor forces have been proposed to assist invasion [22].

Another active biological 'wrapping' process is phagocytotic uptake, see figure 52. Here, the growth of the phagocytotic cup with its actin cytoskeleton is the major dynamic process [238]. Quantification using microscopy and image analysis shows fast uptake at the beginning, followed by a plateau with weakly increasing wrapping fraction, and again fast uptake of the particle towards the end of the process [237]. Various mechanisms for phagocytotic uptake have been suggested, among them receptor diffusion and directed motion [239], a zipper-like mechanism based on membrane fluctuations and membrane adhesion to the particle [240], and hindered uptake by increase and relaxation of membrane tension [241].
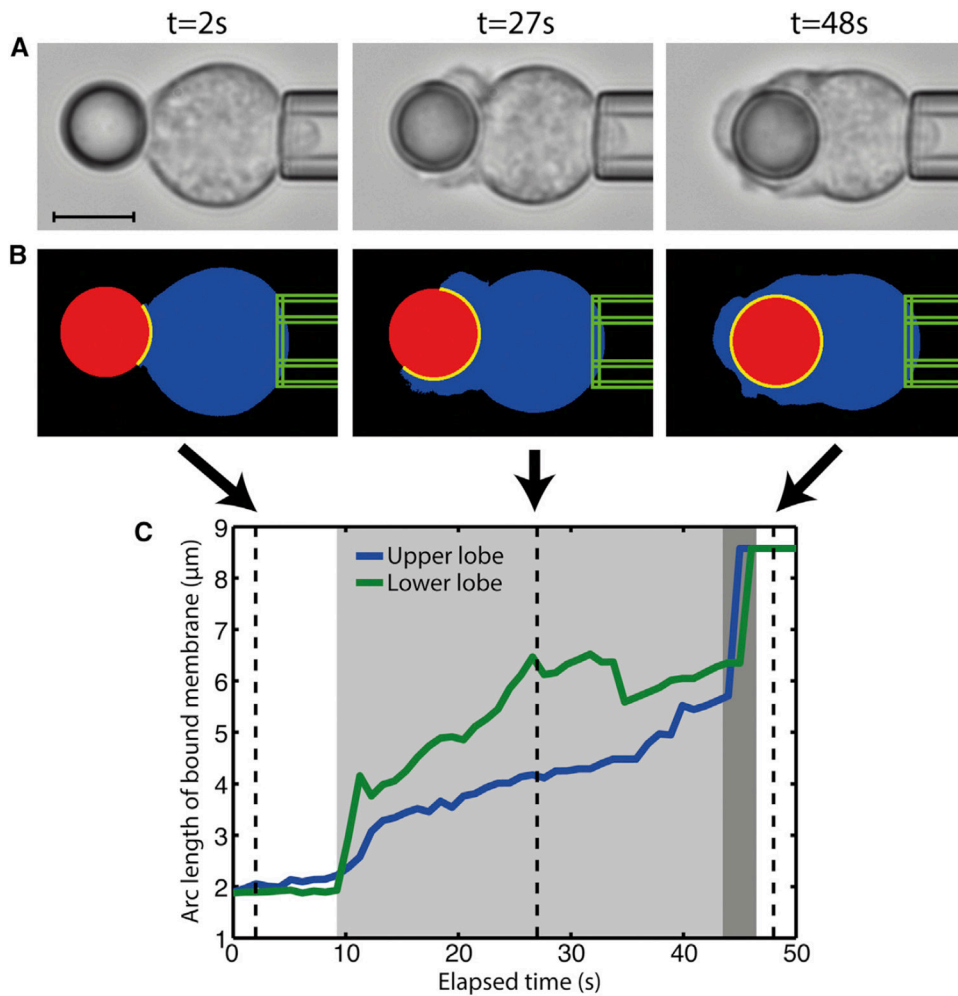
Figure 52. Typical time-lapse movie and image analysis of a neutrophil engulfing an IgG-coated bead with radius $a = 2.3$ μm. The data has been taken from [236]. (A) Raw images of three frames at various stages of engulfment. At $t \approx 2$ s, the bead has been released onto the cell, with a contact area of $A_{ad} \approx 2$ μm^2. At this point engulfment has not yet started. At $t \approx 27$s the bead is approximately half-engulfed, with the lower lobe noticeably ahead of the upper lobe. At $t \approx 48$ s engulfment is complete, the bead is entirely within the cell, and the phagosome is fully formed. The length of the scale bar corresponds to 5 μm. (B) The same frames as in panel A after automatic image analysis: (blue) cell, (red) bead, (green) outline of the pipette, (yellow) membrane attached to the bead. (C) Engulfment as function of time. For both the upper and lower lobes, after engulfment begins at $t \approx 10$ s there is an initial slow stage (light gray) followed by a much quicker second stage (dark gray). Engulfment is complete by $t \approx 46$ s. Reprinted from [237], Copyright (2014), with permission from Elsevier.

4. Conclusions

Multi-phase fluid systems and cellular biological systems abound with interfaces. Nano- and microparticles naturally collect at such interfaces, because their localization at the interfaces lowers their interaction energy with the environment. We have considered here two types of interfaces: fluid-fluid interfaces governed by interfacial tensions, and biological interfaces controlled by curvature elasticity. Particles at both types of interfaces show many common behaviours. The interface attraction depends on particle size, shape, and surface properties. Particles can orient in different ways at interfaces, they deform the interfaces around them, and these interface deformations lead to interface-mediated interactions and collective behaviour.

Although systems and concepts for particles at fluid and biological interfaces are very similar, and for instance SDS stabilisation of droplets can drive the system from fluid interfaces towards membranes [242], there is a major difference. In many cases, particle sizes at fluid interfaces are in the micrometer range, while particle sizes at lipid bilayer membranes are in the nanometer range. This implies that different experimental techniques are required in both cases, where the nanometer scale makes particles at membranes more difficult to observe and more difficult to manipulate. Therefore, we have a better knowledge about particles at fluid interfaces, and there is an urgent need for systematic and well-controlled experiments for particles at membranes. Nevertheless, a unified numerical and theoretical description of both systems is possible—at least for particles above a threshold diameter of about $15 - 20$ nm—on the basis of continuum models for two-dimensional surfaces and their deformations embedded in three-dimensional space.

From the technological point of view, micrometer-sized particles at fluid interfaces can be used in many ways to control and tailor interface properties. Such applications range

from emulsion stabilisation through an effective reduction of the interface tension to the design of solid shells and surfaces with controlled optical properties. From a biological point of view, nanoparticles are interesting in nanomedicine as biomarkes and drug carriers, but their effect on cells also has to be assessed because of their potential nanotoxicity. In addition, there is a large range of biological particles, such as viruses and parasites, the interaction of which with cells is also highly desirable to be controlled.

The interaction of single hard particles with interfaces is by now reasonably well understood. Therefore, we believe that future research should move towards particle-mediated interactions and collective properties for many particles at both fluid and biological interfaces, as well as towards soft particles. For example, size and concentration effects for the interaction or nanoparticles with liposomes and polymersomes have been studied using electron microscopy and scattering [49–51]. Using force measurements, nanoparticle-mediated adhesion between elastic gels has been measured [243]. The hard particles can serve as 'glue' between soft interfaces. Soft particles, e.g. microgel and polymeric particles, add further complexity by allowing the particle shape to adjust in response to the interaction with a fluid or biological interface [160, 244–248].

Finally, dynamical behaviour of particles at fluid and biological interfaces awaits further characterization. For instance, dynamics of wrapping of non-spherical particles by biological interfaces has been discussed in section 3.4.1, but calculations that include Brownian motion are missing. Colloids adsorbed to stabilised oil–water interfaces show different diffusion properties than colloids in bulk [242], systematic studies could be used to measure the viscosity of lipid bilayers. Furthermore, nanoparticles in combination with superresolution microscopy can be used as probes to study dynamics in biological cells [249–251].

To conclude, particles are already widely used for applications, but a systematic understanding of the interactions of engineered nano- and microparticles with soft and biological matter is often lacking. Furthermore, our understanding of basic biological processes on the cellular scale, such as phagocytosis and blood-stage malaria, will benefit from a detailed understanding of particles at biological interfaces. We expect that in the future more systematic studies for particles at fluid and biological interfaces will allow the engineering of even better tailored nano- and microparticles for applications and to achieve a more thorough understanding of cellular uptake and invasion mechanisms. Examples for areas where rational design of interface-particle systems may improve applications include targeted drug delivery for particles at biological interfaces, and a better control of the rheological properties of emulsions for particles at fluid interfaces.

Acknowledgments

References

[1] Pickering S U 1907 CXCVI.-Emulsions *J. Chem. Soc., Trans.* **91** 2001–21

[2] Stratford K, Adhikari R, Pagonabarraga I, Desplat J-C and Cates M E 2005 Colloidal jamming at interfaces: a route to fluid-bicontinuous gels *Science* **309** 2198–201

[3] Ramsden W 1903 Separation of solids in the surface-layers of solutions and 'suspensions' (observations on surface-membranes, bubbles, emulsions and mechanical coagulation).—Preliminary account *Proc. R. Soc. Lond.* **72** 156–64

[4] Aveyard R, Binks B P and Clint J H 2003 Emulsions stabilised solely by colloidal particles *Adv. Colloid Interface Sci.* **100** 503–46

[5] Cates M E and Clegg P S 2008 Bijels: a new class of soft materials *Soft Matter* **4** 2132–8

[6] Canton I and Battaglia G 2012 Endocytosis at the nanoscale *Chem. Soc. Rev.* **41** 2718–39

[7] Hurley J H, Boura E, Carlson L-A and Różycki B 2010 Membrane budding *Cell* **143** 875–87

[8] Weir A, Westerhoff P, Fabricius L, Hristovski K and Von Goetz N. 2012 Titanium dioxide nanoparticles in food and personal care products *Environ. Sci. Technol.* **46** 2242–50

[9] Tiede K, Boxall A B, Tear S P, Lewis J, David H and Hassellöv M 2008 Detection and characterization of engineered nanoparticles in food and the environment *Food Addit. Contam.* **25** 795–821

[10] Dickinson E 2010 Food emulsions and foams: stabilization by particles *Curr. Opin. Colloid Interface Sci.* **15** 40–9

[11] McHale G and Newton M I 2011 Liquid marbles: principles and applications *Soft Matter* **7** 5473–81

[12] Prabhu S and Poulose E K 2012 Silver nanoparticles: mechanism of antimicrobial action, synthesis, medical applications and toxicity effects *Int. Nano Lett.* **2** 1–10

[13] Sondi I and Salopek-Sondi B 2004 Silver nanoparticles as antimicrobial agent: a case study on *e. coli* as a model for gram-negative bacteria *J. Colloid Interface Sci.* **275** 177–82

[14] Calvo P, Remunan-Lopez C, Vila-Jato J and Alonso M 1997 Novel hydrophilic chitosan-polyethylene oxide nanoparticles as protein carriers *J. Appl. Polym. Sci.* **63** 125–32

[15] Wang Y *et al* 2015 Mesoporous silica nanoparticles in drug delivery and biomedical applications, Nanomed. Nanotechnol. Biol. Med. **11** 313–27

[16] Allen T M and Cullis P R 2004 Drug delivery systems: entering the mainstream *Science* **303** 1818–22

[17] Robinson R L M *et al* 2016 How should the completeness and quality of curated nanomaterial data be evaluated? *Nanoscale* **8** 9919–43

[18] Toropova A P, Toropov A A, Benfenati E and Korenstein R 2014 Qsar model for cytotoxicity of SiO2 nanoparticles on human lung fibroblasts *J. Nanopart. Res.* **16** 1–7

[19] Ivask A *et al* 2014 Size-dependent toxicity of silver nanoparticles to bacteria, yeast, algae, crustaceans and mammalian cells *in vitro PLOS One* **9** e102108

[20] Pletikapić G, Žutić V, Vinković Vrček I and Svetličić V 2012 Atomic force microscopy characterization of silver nanoparticles interactions with marine diatom cells and extracellular polymeric substance *J. Mol. Rec.* **25** 309–17

[21] Heinlaan M, Ivask A, Blinova I, Dubourguier H-C and Kahru A 2008 Toxicity of nanosized and bulk ZnO, CuO and tio 2 to bacteria vibrio fischeri and crustaceans daphnia magna and thamnocephalus platyurus *Chemosphere* **71** 1308–16

[22] Dasgupta S *et al* 2014 Membrane-wrapping contributions to malaria parasite invasion of the human erythrocyte *Biophys. J.* **107** 43–54

[23] Cowman A F and Crabb B S 2006 Invasion of red blood cells by malaria parasites *Cell* **124** 755–66

[24] Luo J, Wang Z W, Wang F, Zhang H, Lu J, Guo H Y and Ren F Z 2014 Cryo-sem images of native milk fat globule indicate small casein micelles are constituents of the membrane *RSC Adv.* **4** 48963–6

[25] Champion J A, Katare Y K and Mitragotri S 2007 Making polymeric micro-and nanoparticles of complex shapes *Proc. Natl Acad. Sci. USA* **104** 11901–4

[26] Park J-G, Forster J D and Dufresne E R 2010 High-yield synthesis of monodisperse dumbbell-shaped polymer nanoparticles *J. Am. Chem. Soc.* **132** 5960–1

[27] Cho E C, Zhang Q and Xia Y 2011 The effect of sedimentation and diffusion on cellular uptake of gold nanoparticles *Nat. Nanotechnol.* **6** 385–91

[28] Noda T, Ebihara H, Muramoto Y, Fujii K, Takada A, Sagara H, Kim J H, Kida H, Feldmann H and Kawaoka Y 2006 Assembly and budding of ebolavirus *PLoS Pathog.* **2** e99

[29] Welsch S, Kolesnikova L, Krahling V, Riches J D, Becker S and Briggs J 2010 Electron tomography reveals the steps in filovirus budding *PLoS Pathog.* **6** e1000875

[30] Hoffelner D, Kundt M, Schmidt A M, Kentzinger E, Bender P and Disch S 2015 Directing the orientational alignment of anisotropic magnetic nanoparticles using dynamic magnetic fields *Faraday Discuss.* **181** 449–61

[31] Höfling F and Dietrich S 2015 Enhanced wavelength-dependent surface tension of liquid-vapour interfaces *Europhys. Lett.* **109** 46002

[32] Risselada H J and Marrink S J 2008 The molecular face of lipid rafts in model membranes *Proc. Natl Acad. Sci. USA* **105** 17367–72

[33] Safran S A 1994 *Statistical Thermodynamics Of Surfaces, Interfaces And Membranes* (Boulder, CO: Perseus Books)

[34] Helfrich W 1973 Elastic properties of lipid bilayers: theory and possible experiments *Z. Naturforsch.* C **28** 693–703

[35] Blanc C, Fedorenko D, Gross M, In M, Abkarian M, Gharbi M A, Fournier J-B, Galatola P and Nobili M 2013 Capillary force on a micrometric sphere trapped at a fluid interface exhibiting arbitrary curvature gradients *Phys. Rev. Lett.* **111** 058302

[36] Noguchi H and Gompper G 2005 Shape transitions of fluid vesicles and red blood cells in capillary flows *Proc. Natl Acad. Sci. USA* **102** 14159–64

[37] Fedosov D A, Caswell B and Karniadakis G E 2010 A multiscale red blood cell model with accurate mechanics, rheology and dynamics *Biophys. J.* **98** 2215–25

[38] Anderson T H, Min Y, Weirich K L, Zeng H, Fygenson D and Israelachvili J N 2009 Formation of supported bilayers on silica substrates *Langmuir* **25** 6997–7005

[39] Moy V T, Jiao Y, Hillmann T, Lehmann H and Sano T 1999 Adhesion energy of receptor-mediated interaction measured by elastic deformation *Biophys. J.* **76** 1632–8

[40] Gruhn T, Franke T, Dimova R and Lipowsky R 2007 Novel method for measuring the adhesion energy of vesicles *Langmuir* **23** 5423–9

[41] Bresme F and Faraudo J 2007 Orientational transitions of anisotropic nanoparticles at liquid–liquid interfaces *J. Phys.: Condens. Matter* **19** 375110

[42] Agudo-Canalejo J and Lipowsky R 2015 Critical particle sizes for the engulfment of nanoparticles by membranes and vesicles with bilayer asymmetry *ACS Nano* **9** 3704–20

[43] Dasgupta S, Katava M, Faraj M, Auth T and Gompper G 2014 Capillary assembly of microscale ellipsoidal, cuboidal and spherical particles at interfaces *Langmuir* **30** 11873–82

[44] van der Wel C, Vahid A, Šarić A, Idema T, Heinrich D and Kraft D J 2016 Lipid membrane-mediated attraction between curvature inducing objects *Sci. Rep.* **6** 32825

[45] Loudet J C, Alsayed A M, Zhang J and Yodh A G 2005 Capillary interactions between anisotropic colloidal particles *Phys. Rev. Lett.* **94** 018301

[46] Bahrami A H, Lipowsky R and Weikl T R 2012 Tubulation and aggregation of spherical nanoparticles adsorbed on vesicles *Phys. Rev. Lett.* **109** 188102

[47] Šarić A and Cacciuto A 2012 Mechanism of membrane tube formation induced by adhesive nanocomponents *Phys. Rev. Lett.* **109** 188101

[48] Reynwar B J and Deserno M 2011 Membrane-mediated interactions between circular particles in the strongly curved regime *Soft Matter* **7** 8567–75

[49] Jaskiewicz K, Larsen A, Lieberwirth I, Koynov K, Meier W, Fytas G, Kroeger A and Landfester K 2012 Probing bioinspired transport of nanoparticles into polymersomes *Angew. Chem.* **124** 4691–5

[50] Michel R, Kesselman E, Plostica T, Danino D and Gradzielski M 2014 Internalization of silica nanoparticles into fluid liposomes: formation of interesting hybrid colloids *Angew. Chem. Int. Ed.* **53** 12441–5

[51] Michel R, Plostica T, Abezgauz L, Danino D and Gradzielski M 2013 Control of the stability and structure of liposomes by means of nanoparticles *Soft Matter* **9** 4167–77

[52] Huang B, Wang W, Bates M and Zhuang X 2008 Three-dimensional super-resolution imaging by stochastic optical reconstruction microscopy *Science* **319** 810–3

[53] Betzig E, Patterson G H, Sougrat R, Lindwasser O W, Olenych S, Bonifacino J S, Davidson M W, Lippincott-Schwartz J and Hess H F 2006 Imaging intracellular fluorescent proteins at nanometer resolution *Science* **313** 1642–5

[54] Hell S W 2007 Far-field optical nanoscopy *Science* **316** 1153–8

[55] Ruska H 1940 Die Sichtbarmachung der bakteriophagen Lyse im Übermikroskop *Naturwissenschaften* **28** 45–6

[56] Davies G B, Krüger T, Coveney P V and Harting J 2014 Detachment energies of spheroidal particles from fluid–fluid interfaces *J. Chem. Phys.* **141** 154902

[57] Coertjens S, Moldenaers P, Vermant J and Isa L 2014 Contact angles of microellipsoids at fluid interfaces *Langmuir* **30** 4289–300

[58] Chan D, Henry J and White L 1981 The interaction of colloidal particles collected at fluid interfaces *J. Colloid Interface Sci.* **79** 410–8

[59] Vella D and Mahadevan L 2005 The 'cheerios effect' *Am. J. Phys.* **73** 817–25

[60] Galatola P and Fournier J-B 2014 Capillary force acting on a colloidal particle floating on a deformed interface. *Soft Matter* **10** 2197–212

[61] Ershov D, Sprakel J, Appel J, Stuart M A C and van der Gucht J 2013 Capillarity-induced ordering of spherical colloids on an interface with anisotropic curvature *Proc. Natl Acad. Sci. USA* **110** 9220–4

[62] Bresme F and Oettel M 2007 Nanoparticles at fluid interfaces *J. Phys.: Condens. Matter* **19** 413101

[63] Pieranski P 1980 Two-dimensional interfacial colloidal crystals *Phys. Rev. Lett.* **45** 569

[64] Komura S, Hirose Y and Nonomura Y 2006 Adsorption of colloidal particles to curved interfaces *J. Chem. Phys.* **124** 241104

[65] Lewandowski E P, Cavallaro M, Botto L, Bernate J C, Garbin V and Stebe K J 2010 Orientation and self-assembly of cylindrical particles by anisotropic capillary interactions *Langmuir* **26** 15142–54

[66] Grzelczak M, Vermant J, Furst E M and Liz-Marzán L M 2010 Directed self-assembly of nanoparticles *ACS Nano* **4** 3591–605

[67] Stamou D, Duschl C and Johannsmann D 2000 Long-range attraction between colloidal spheres at the air-water interface: the consequence of an irregular meniscus *Phys. Rev.* E **62** 5263–72

[68] Yao L, Botto L, Cavallaro M Jr, Bleier B J, Garbin V and Stebe K J 2013 Near field capillary repulsion *Soft Matter* **9** 779–86

[69] Lucassen J 1992 Capillary forces between solid particles in fluid interfaces *Colloids Surf.* **65** 131–7

[70] Botto L, Lewandowski E P, Cavallaro M and Stebe K J 2012 Capillary interactions between anisotropic particles *Soft Matter* **8** 9957–71

[71] Yao L, Sharifi-Mood N, Liu I B and Stebe K J 2014 Capillary migration of microdisks on curved interfaces *J. Colloid Interface Sci.* **449** 436–42

[72] Sharifi-Mood N, Liu I B and Stebe K J 2015 Curvature capillary migration of microspheres *Soft Matter* **11** 6768–79

[73] Isa L, Samudrala N and Dufresne E R 2014 Adsorption of sub-micron amphiphilic dumbbells to fluid interfaces *Langmuir* **30** 5057–63

[74] Loudet J C, Yodh A G and Pouligny B 2006 Wetting and contact lines of micrometer-sized ellipsoids *Phys. Rev. Lett.* **97** 018304

[75] Lehle H, Noruzifar E and Oettel M 2008 Ellipsoidal particles at fluid interfaces *Eur. Phys. J.* E **26** 151–60

[76] Botto L, Yao L, Leheny R L and Stebe K J 2012 Capillary bond between rod-like particles and the micromechanics of particle-laden interfaces *Soft Matter* **8** 4971–9

[77] Loudet J and Pouligny B 2011 How do mosquito eggs self-assemble on the water surface? *Eur. Phys. J.* E **34** 1–17

[78] Lewandowski E P, Bernate J A, Tseng A, Searson P C and Stebe K J 2009 Oriented assembly of anisotropic particles by capillary interactions *Soft Matter* **5** 886–90

[79] Denkov N, Velev O, Kralchevski P, Ivanov I, Yoshimura H and Nagayama K 1992 Mechanism of formation of two-dimensional crystals from latex particles on substrates *Langmuir* **8** 3183–90

[80] Dippenaar A 1982 The destabilization of froth by solids. I. The mechanism of film rupture *Int. J. Miner. Process.* **9** 1–14

[81] Kralchevsky P A and Nagayama K 2000 Capillary interactions between particles bound to interfaces, liquid films and biomembranes *Adv. Colloid Interface Sci.* **85** 145–92

[82] Morris G, Hadler K and Cilliers J 2015 Particles in thin liquid films and at interfaces *Curr. Opin. Colloid Interface Sci.* **20** 98–104

[83] Hu D L and Bush J W 2005 Meniscus-climbing insects *Nature* **437** 733–6

[84] Yu Y, Guo M, Li X and Zheng Q-S 2007 Meniscus-climbing behavior and its minimum free-energy mechanism *Langmuir* **23** 10546–50

[85] He A, Nguyen K and Mandre S 2013 Capillary interactions between nearby interfacial objects *Europhys. Lett.* **102** 38001

[86] Bowden N, Oliver S R J and Whitesides G M 2000 Mesoscale self-assembly: capillary bonds and negative menisci *J. Phys. Chem.* B **104** 2714–24

[87] Nicolson M M 1949 The interaction between floating particles *Math. Proc. Cambridge Phil. Soc.* **45** 288–95

[88] Gifford W and Scriven L 1971 On the attraction of floating particles *Chem. Eng. Sci.* **26** 287–97

[89] Oettel M, Dominquez A and Dietrich S 2005 Effective capillary interaction of spherical particles at fluid interfaces *Phys. Rev.* E **71** 051401

[90] Dominquez A, Oettel M and Dietrich S 2008 Force balance of particles trapped at fluid interfaces *J. Chem. Phys.* **128** 114904

[91] Davies G B, Krüger T, Coveney P V, Harting J and Bresme F 2014 Interface deformations affect the orientation transition of magnetic ellipsoidal particles adsorbed at fluid–fluid interfaces *Soft Matter* **10** 6742–8

[92] Newton B J and Buzza D M A 2016 Magnetic cylindrical colloids at liquid interfaces exhibit non-volatile switching of their orientation in an external field *Soft Matter* **12** 5285–96

[93] Rezvantalab H and Shojaei-Zadeh S 2013 Role of geometry and amphiphilicity on capillary-induced interactions between anisotropic janus particles *Langmuir* **29** 14962–70

[94] Park B J, Choi C-H, Kang S-M, Tettey K E, Lee C-S and Lee D 2013 Double hydrophilic Janus cylinders at an air–water interface *Langmuir* **29** 1841–9

[95] Park B J, Choi C-H, Kang S-M, Tettey K E, Lee C-S and Lee D 2013 Geometrically and chemically anisotropic particles at an oil–water interface *Soft Matter* **9** 3383–8

[96] Anjali T G and Basavaraj M G 2017 Shape induced deformation, capillary bridging and self-assembly of cuboids at fluid-fluid interface *Langmuir* **33** 791–801

[97] Soligno G, Dijkstra M and van Roij R 2016 Self-assembly of cubes into 2d hexagonal and honeycomb lattices by hexapolar capillary interactions *Phys. Rev. Lett.* **116** 258001

[98] Morris G, Neethling S and Cilliers J 2012 Modelling the self orientation of particles in a film *Miner. Eng.* **33** 87–92

[99] Hu D L, Chan B and Bush J W 2003 The hydrodynamics of water strider locomotion *Nature* **424** 663–6

[100] Kralchevsky P A and Nagayama K 1994 Capillary forces between colloidal particles *Langmuir* **10** 23–36

[101] Rao S R 2013 *Surface Chemistry of Froth Flotation: volume 1: Fundamentals* (Berlin: Springer)

[102] Morris G, Neethling S and Cilliers J 2010 The effects of hydrophobicity and orientation of cubic particles on the stability of thin films *Miner. Eng.* **23** 979–84

[103] Cavallaro M, Botto L, Lewandowski E P, Wang M and Stebe K J 2011 Curvature-driven capillary migration and assembly of rod-like particles *Proc. Natl Acad. Sci. USA* **108** 20923–8

[104] Leandri J and Wuerger A 2013 Trapping energy of a spherical particle on a curved liquid interface *J. Colloid Interface Sci.* **405** 249–55

[105] Kralchevsky P, Ivanov I, Ananthapadmanabhan K and Lips A 2005 On the thermodynamics of particle-stabilized emulsions: curvature effects and catastrophic phase inversion *Langmuir* **21** 50–63

[106] Würger A 2006 Curvature-induced capillary interaction of spherical particles at a liquid interface *Phys. Rev.* E **74** 041402

[107] Lewandowski E P, Bernate J A, Searson P C and Stebe K J 2008 Rotation and alignment of anisotropic particles on nonplanar interfaces *Langmuir* **24** 9302–7

[108] Park B J and Lee D 2012 Equilibrium orientation of nonspherical Janus particles at fluid–fluid interfaces *ACS Nano* **6** 782–90

[109] Newton B J, Brakke K A and Buzza D M A 2014 Influence of magnetic field on the orientation of anisotropic magnetic particles at liquid interfaces *Phys. Chem. Chem. Phys.* **16** 26051–8

[110] Davies G B, Krüger T, Coveney P V, Harting J and Bresme F 2014 Assembling ellipsoidal particles at fluid interfaces using switchable dipolar capillary interactions *Adv. Mater.* **26** 6715–9

[111] Danov K D, Kralchevsky P A, Naydenov B N and Brenn G 2005 Interactions between particles with an undulated contact line at a fluid interface: capillary multipoles of arbitrary order *J. Colloid Interface Sci.* **287** 121–34

[112] Loudet J C and Pouligny B 2009 Self-assembled capillary arrows *Europhys. Lett.* **85** 28003

[113] Madivala B, Fransaer J and Vermant J 2009 Self-assembly and rheology of ellipsoidal particles at interfaces *Langmuir* **25** 2718–28

[114] Van Nierop E, Stijnman M and Hilgenfeldt S 2005 Shape-induced capillary interactions of colloidal particles *Europhys. Lett.* **72** 671

[115] Fournier J-B and Galatola P 2002 Anisotropic capillary interactions and jamming of colloidal particles trapped at a liquid-fluid interface *Phys. Rev.* E **65** 031601

[116] Schwenke K, Isa L and Del Gado E 2014 Assembly of nanoparticles at liquid interfaces: crowding and ordering *Langmuir* **30** 3069–74

[117] de Folter J W, Hutter E M, Castillo S I, Klop K E, Philipse A P and Kegel W K 2013 Particle shape anisotropy in pickering emulsions: cubes and peanuts *Langmuir* **30** 955–64

[118] Xie Q, Davies G B, Günther F and Harting J 2015 Tunable dipolar capillary deformations for magnetic janus particles at fluid–fluid interfaces *Soft Matter* **11** 3581–8

[119] Günther F, Frijters S and Harting J 2014 Timescales of emulsion formation caused by anisotropic particles *Soft Matter* **10** 4977–89

[120] Günther F, Janoschek F, Frijters S and Harting J 2013 Lattice boltzmann simulations of anisotropic particles at liquid interfaces *Comput. Fluids* **80** 184–9

[121] Irvine W T, Vitelli V and Chaikin P M 2010 Pleats in crystals on curved surfaces *Nature* **468** 947–51

[122] Tasinkevych M, Mondiot F, Mondain-Monval O and Loudet J-C 2014 Dispersions of ellipsoidal particles in a nematic liquid crystal *Soft Matter* **10** 2047–58

[123] Galatola P and Fournier J B 2001 Nematic-wetted colloids in the isotropic phase: Pairwise interaction biaxiality and defects *Phys. Rev. Lett.* **86** 3915–8

[124] Tkalec U, Škarabot M and Muševič I 2008 Interactions of micro-rods in a thin layer of a nematic liquid crystal *Soft Matter* **4** 2402–9

[125] Liu I B, Gharbi M A, Ngo V L, Kamien R D, Yang S and Stebe K J 2015 Elastocapillary interactions on nematic films *Proc. Natl Acad. Sci. USA* **112** 6336–40

[126] Jeridi H, Gharbi M A, Othman T and Blanc C 2015 Capillary-induced giant elastic dipoles in thin nematic films *Proc. Natl Acad. Sci. USA* **112** 14771–6

[127] Kalashnikova I, Bizot H, Bertoncini P, Cathala B and Capron I 2013 Cellulosic nanorods of various aspect ratios for oil in water pickering emulsions *Soft Matter* **9** 952–9

[128] Dugyala V R, Daware S V and Basavaraj M G 2013 Shape anisotropic colloids: synthesis, packing behavior, evaporation driven assembly, and their application in emulsion stabilization *Soft Matter* **9** 6711–25

[129] Guzowski J, Tasinkevych M and Dietrich S 2011 Capillary interactions in pickering emulsions *Phys. Rev.* E **84** 031401

[130] Lee D and Weitz D A 2009 Nonspherical colloidosomes with multiple compartments from double emulsions *Small* **5** 1932–5

[131] Aveyard R 2012 Can Janus particles give thermodynamically stable pickering emulsions? *Soft Matter* **8** 5233–40

[132] Madivala B, Vandebril S, Fransaer J and Vermant J 2009 Exploiting particle shape in solid stabilized emulsions *Soft Matter* **5** 1717–27

[133] Dinsmore A, Hsu M F, Nikolaides M, Marquez M, Bausch A and Weitz D 2002 Colloidosomes: selectively permeable capsules composed of colloidal particles *Science* **298** 1006–9

[134] Deegan R D, Bakajin O, Dupont T F, Huber G, Nagel S R and Witten T A 1997 Capillary flow as the cause of ring stains from dried liquid drops *Nature* **389** 827–9

[135] Yunker P J, Still T, Lohr M A and Yodh A 2011 Suppression of the coffee-ring effect by shape-dependent capillary interactions *Nature* **476** 308–11

[136] Dippenaar A 1982 The destabilization of froth by solids. II. The rate-determining step *Int. J. Miner. Process.* **9** 15–22

[137] Barnoud J, Rossi G and Monticelli L 2014 Lipid membranes as solvents for carbon nanoparticles *Phys. Rev. Lett.* **112** 068102

[138] Yang K and Ma Y-Q 2010 Computer simulation of the translocation of nanoparticles with different shapes across a lipid bilayer *Nat. Nanotechnol.* **5** 579–83

[139] Dasgupta S, Auth T and Gompper G 2013 Wrapping of ellipsoidal nano-particles by fluid membranes *Soft Matter* **9** 5473–82

[140] Reynwar B J, Illya G, Harmandaris V A, Müller M M, Kremer K and Deserno M 2007 Aggregation and vesiculation of membrane proteins by curvature-mediated interactions *Nature* **447** 461–4

[141] Florez L, Herrmann C, Cramer J M, Hauser C P, Koynov K, Landfester K, Crespy D and Mailänder V 2012 How shape influences uptake: interactions of anisotropic polymer nanoparticles and human mesenchymal stem cells *Small* **8** 2222–30

[142] Rossi G and Monticelli L 2014 Modeling the effect of nano-sized polymer particles on the properties of lipid membranes *J. Phys.: Condens. Matter* **26** 503101

[143] Pogodin S and Baulin V A 2010 Can a carbon nanotube pierce through a phospholipid bilayer? *ACS Nano* **4** 5293–300

[144] Vacha R, Martinez-Veracoechea F J and Frenkel D 2012 Intracellular release of endocytosed nanoparticles upon a change of ligand–receptor interaction *ACS Nano* **6** 10598–605

[145] Tian F, Zhang X and Dong W 2014 How hydrophobic nanoparticles aggregate in the interior of membranes: a computer simulation *Phys. Rev.* E **90** 052701

[146] Guo Y, Terazzi E, Seemann R, Fleury J B and Baulin V A 2016 Direct proof of spontaneous translocation of lipid-covered hydrophobic nanoparticles through a phospholipid bilayer *Sci. Adv.* **2** e1600261

[147] Hoffmann I, Michel R, Sharp M, Holderer O, Appavou M-S, Polzer F, Farago B and Gradzielski M 2014 Softening of phospholipid membranes by the adhesion of silica nanoparticles—as seen by neutron spin-echo (NSE) *Nanoscale* **6** 6945–52

[148] Van Lehn R C, Ricci M, Silva P H, Andreozzi P, Reguera J, Vo K, Stellacci F and Alexander-Katz A 2014 Lipid tail protrusions mediate the insertion of nanoparticles into model cell membranes *Nat. Commun.* **5** 1

[149] Deserno M 2004 Elastic deformation of a fluid membrane upon colloid binding *Phys. Rev.* E **69** 031903

[150] Smith A-S, Sackmann E and Seifert U 2003 Effects of a pulling force on the shape of a bound vesicle *Europhys. Lett.* **64** 281

[151] Seifert U and Lipowsky R 1990 Adhesion of vesicles *Phys. Rev.* A **42** 4768

[152] Helm C A, Israelachvili J N and McGuiggan M P 1989 Molecular mechanisms and forces involved in the adhesion and fusion of amphiphilic bilayers *Science* **17** 919–22

[153] Fošnarič M, Iglič A, Kroll D M and May S 2009 Monte Carlo simulations of complex formation between a mixed fluid vesicle and a charged colloid *J. Chem. Phys.* **131** 105103

[154] Gao H, Shi W and Freund L B 2005 Mechanics of receptor-mediated endocytosis *Proc. Natl Acad. Sci. USA* **102** 9469–74

[155] Chaudhuri A, Battaglia G and Golestanian R 2011 The effect of interactions on the cellular uptake of nanoparticles *Phys. Biol.* **8** 046002

[156] Decuzzi P and Ferrari M 2008 The receptor-mediated endocytosis of nonspherical particles *Biophys. J.* **94** 3790–7

[157] Smith A-S, Sengupta K, Goennenwein S, Seifert U and Sackmann E 2008 Force-induced growth of adhesion domains is controlled by receptor mobility *Proc. Natl Acad. Sci. USA* **105** 6906–11

[158] Fenz S F, Smith A-S, Merkel R and Sengupta K 2011 Inter-membrane adhesion mediated by mobile linkers: effect of receptor shortage *Soft Matter* **7** 952–62

[159] Tzlil S, Deserno M, Gelbart W M and Ben-Shaul A 2004 A statistical-thermodynamic model of viral budding *Biophys. J.* **86** 2037–48

[160] Yi X and Gao H 2017 Kinetics of receptor-mediated endocytosis of elastic nanoparticles *Nanoscale* **9** 454–63

[161] Müller J, Bauer K N, Prozeller D, Simon J, Mailänder V, Wurm F R, Winzen S and Landfester K 2017 Coating nanoparticles with tunable surfactants facilitates control over the protein corona *Biomaterials* **115** 1–8

[162] Lopez H and Lobaskin V 2015 Coarse-grained model of adsorption of blood plasma proteins onto nanoparticles *J. Chem. Phys.* **143** 243138

[163] Lundqvist M, Stigler J, Elia G, Lynch I, Cedervall T and Dawson K A 2008 Nanoparticle size and surface properties determine the protein corona with possible implications for biological impacts *Proc. Natl Acad. Sci. USA* **105** 14265–70

[164] Monopoli M P, Åberg C, Salvati A and Dawson K A 2012 Biomolecular coronas provide the biological identity of nanosized materials *Nat. Nanotechnol.* **7** 779–86

[165] Salvati A, Pitek A S, Monopoli M P, Prapainop K, Bombelli F B, Hristov D R, Kelly P M, Åberg C, Mahon E and Dawson K A 2013 Transferrin-functionalized nanoparticles lose their targeting capabilities when a biomolecule corona adsorbs on the surface *Nat. Nanotechnol.* **8** 137–43

[166] Churchman A H, Wallace R, Milne S J, Brown A P, Brydson R and Beales P A 2013 Serum albumin enhances the membrane activity of zno nanoparticles *Chem. Commun.* **49** 4172–4

[167] Morris C and Homann U 2001 Cell surface area regulation and membrane tension *J. Membr. Biol.* **179** 79–102

[168] Deserno M and Bickel T 2003 Wrapping of a spherical colloid by a fluid membrane *Europhys. Lett.* **62** 767

[169] Weikl T, Kozlov M and Helfrich W 1998 Interaction of conical membrane inclusions: effect of lateral tension *Phys. Rev.* E **57** 6988

[170] Auth T and Gompper G 2009 Budding and vesiculation induced by conical membrane inclusions *Phys. Rev.* E **80** 031901

[171] Breidenich M, Netz R and Lipowsky R 2000 The shape of polymer-decorated membranes *Europhys. Lett.* **49** 431

[172] Bickel T, Marques C and Jeppesen C 2000 Pressure patches for membranes: The induced pinch of a grafted polymer *Phys. Rev.* E **62** 1124

[173] Hiergeist C and Lipowsky R 1996 Elastic properties of polymer-decorated membranes *J. Phys.* II (France) **6** 1465–81

[174] Auth T and Gompper G 2003 Self-avoiding linear and star polymers anchored to membranes *Phys. Rev.* E **68** 051801

[175] Deserno M 2004 When do fluid membranes engulf sticky colloids? *J. Phys.: Condens. Matter* **16** S2061

[176] Dasgupta S, Auth T and Gompper G 2014 Shape and orientation matter for the cellular uptake of nonspherical particles *Nano Lett.* **14** 687–93

[177] Angelikopoulos P, Sarkisov L, Cournia Z and Gkeka P 2017 Self-assembly of anionic, ligand-coated nanoparticles in lipid membranes *Nanoscale* **9** 1040–8

[178] Kahraman O, Koch P D, Klug W S and Haselwandter C A 2016 Bilayer-thickness-mediated interactions between integral membrane proteins *Phys. Rev.* E **93** 042410

[179] Jafarinia H, Khoshnood A and Jalali M A 2016 Rigidity of transmembrane proteins determines their cluster shape *Phys. Rev.* E **93** 012403

[180] Khoshnood A, Noguchi H and Gompper G 2010 Lipid membranes with transmembrane proteins in shear flow *J. Chem. Phys.* **132** 025101

[181] Brannigan G and Brown F L 2007 Contributions of gaussian curvature and nonconstant lipid volume to protein deformation of lipid bilayers *Biophys. J.* **92** 864–76

[182] Dan N, Berman A, Pincus P and Safran S 1994 Membrane-induced interactions between inclusions *J. Phys.* II (France) **4** 1713–25

[183] Bahrami A H, Lipowsky R and Weikl T R 2016 The role of membrane curvature for the wrapping of nanoparticles *Soft Matter* **12** 581–7

[184] Agudo-Canalejo J and Lipowsky R 2015 Adhesive nanoparticles as local probes of membrane curvature *Nano Lett.* **15** 7168–73

[185] Dasgupta S, Auth T and Gompper G 2015 Correction: wrapping of ellipsoidal nano-particles by fluid membranes *Soft Matter* **11** 7441–4

[186] Huang C, Zhang Y, Yuan H, Gao H and Zhang S 2013 Role of nanoparticle geometry in endocytosis: laying down to stand up *Nano Lett.* **13** 4546–50

[187] Auth T and Gov N S 2009 Diffusion in a fluid membrane with a flexible cortical cytoskeleton *Biophys. J.* **96** 818–30

[188] Sheetz M 1983 Membrane skeletal dynamics: role in modulation of red cell deformability, mobility of transmembrane proteins and shape *Semin. Hematol.* **20** 175–88

[189] Kusumi A, Sako Y, Fujiwara T and Tomishige M 1997 Application of laser tweezers to studies of the fences and tethers of the membrane skeleton that regulate the movements of plasma membrane proteins *Methods Cell Biol.* **55** 173–94

[190] Almeida P F and Vaz W L 1995 Lateral diffusion in membranes *Handbook of Biological Physics* Chapter 6 305–57

[191] Auth T, Safran S and Gov N S 2007 Filament networks attached to membranes: cytoskeletal pressure and local bilayer deformation *New J. Phys.* **9** 430

[192] Gov N and Safran S 2005 Red blood cell membrane fluctuations and shape controlled by atp-induced cytoskeletal defects *Biophys. J.* **88** 1859–74

[193] Park Y, Best C A, Auth T, Gov N S, Safran S A, Popescu G, Suresh S and Feld M S 2010 Metabolic remodeling of the human red blood cell membrane *Proc. Natl Acad. Sci.* **107** 1289–94

[194] Turlier H, Fedosov D, Audoly B, Auth T, Gov N, Sykes C, Joanny J-F, Gompper G and Betz T 2016 Equilibrium physics breakdown reveals the active nature of red blood cell flickering *Nat. Phys.* **12** 513–19

[195] Vácha R, Martinez-Veracoechea F J and Frenkel D 2011 Receptor-mediated endocytosis of nanoparticles of various shapes *Nano Lett.* **11** 5391–5

[196] Gao Y and Yu Y 2013 How half-coated janus particles enter cells *J. Am. Chem. Soc.* **135** 19091–4

[197] Agudo-Canalejo J and Lipowsky R 2017 Uniform and janus-like nanoparticles in contact with vesicles: energy landscapes and curvature-induced forces *Soft Matter* **13** 2155–73

[198] Fabry B, Maksym G N, Butler J P, Glogauer M, Navajas D and Fredberg J J 2001 Scaling the microrheology of living cells *Phys. Rev. Lett.* **87** 148102

[199] Chen L, Maybeck V, Offenhäusser A and Krause H-J 2016 Implementation and application of a novel 2d magnetic twisting cytometry based on multi-pole electromagnet *Rev. Sci. Instrum.* **87** 064301

[200] Puig-de Morales-Marinkovic M, Turner K T, Butler J P, Fredberg J J and Suresh S 2007 Viscoelasticity of the human red blood cell *Am. J. Physiol. Cell Physiol.* **293** C597–605

[201] Puig-de Morales M, Millet E, Fabry B, Navajas D, Wang N, Butler J P and Fredberg J J 2004 Cytoskeletal mechanics in adherent human airway smooth muscle cells: probe specificity and scaling of protein-protein dynamics *Am. J. Physiol. Cell Physiol.* **287** C643–54

[202] Auth T, Safran S and Gov N S 2007 Fluctuations of coupled fluid and solid membranes with application to red blood cells *Phys. Rev.* E **76** 051910

[203] Šarić A and Cacciuto A 2012 Fluid membranes can drive linear aggregation of adsorbed spherical nanoparticles *Phys. Rev. Lett.* **108** 118101

[204] Goulian M, Bruinsma R and Pincus P 1993 Long-range forces in heterogeneous fluid membranes *Europhys. Lett.* **22** 145

[205] Dommersnes P and Fournier J-B 1999 Casimir and mean-field interactions between membrane inclusions subject to external torques *Europhys. Lett.* **46** 256

[206] Pezeshkian W *et al* 2016 Mechanism of Shiga Toxin clustering on membranes *ACS Nano* **11** 314–24

[207] Rawicz W, Olbrich K, McIntosh T, Needham D and Evans E 2000 Effect of chain length and unsaturation on elasticity of lipid bilayers *Biophys. J.* **79** 328–39

[208] Weikl T R 2003 Indirect interactions of membrane-adsorbed cylinders *Eur. Phys. J.* E **12** 265–73

[209] Mkrtchyan S, Ing C and Chen J Z 2010 Adhesion of cylindrical colloids to the surface of a membrane *Phys. Rev.* E **81** 011904

[210] Brakke K A 1992 The surface evolver *Exp. Math.* **1** 141–65

[211] Gompper G and Kroll D M 2004 Triangulated surface models of fluctuating membranes *Statistical Mechanics of Membranes and Surfaces* ed D R Nelson *et al* (Singapore: World Scientific)

[212] Gompper G and Kroll D 1997 Network models of fluid, hexatic and polymerized membranes *J. Phys.: Condens. Matter* **9** 8795

[213] Kroll D and Gompper G 1992 The conformation of fluid membranes: Monte Carlo simulations *Science* **255** 968

[214] Raatz M, Lipowsky R and Weikl T R 2014 Cooperative wrapping of nanoparticles by membrane tubes *Soft Matter* **10** 3570–7

[215] Kim K, Neu J and Oster G 1999 Many-body forces between membrane inclusions: A new pattern-formation mechanism *Europhys. Lett.* **48** 99

[216] Atilgan E and Sun S X 2007 Shape transitions in lipid membranes and protein mediated vesicle fusion and fission *J. Chem. Phys.* **126** 095102

[217] Kim K, Neu J and Oster G 2000 Effect of protein shape on multibody interactions between membrane inclusions *Phys. Rev.* E **61** 4281

[218] Koltover I, Rädler J O and Safinya C R 1999 Membrane mediated attraction and ordered aggregation of colloidal particles bound to giant phospholipid vesicles *Phys. Rev. Lett.* **82** 1991

[219] Ewers H *et al* 2010 Gm1 structure determines sv40-induced membrane invagination and infection *Nat. Cell Biol.* **12** 11–8

[220] Prabha S, Zhou W-Z, Panyam J and Labhasetwar V 2002 Size-dependency of nanoparticle-mediated gene transfection: studies with fractionated nanoparticles *Int. J. Pharm.* **244** 105–15

[221] Desai M P, Labhasetwar V, Walter E, Levy R J and Amidon G L 1997 The mechanism of uptake of biodegradable microparticles in caco-2 cells is size dependent *Pharm. Res.* **14** 1568–73

[222] Müller K, Fedosov D A and Gompper G 2016 Understanding particle margination in blood flow–a step toward optimized drug delivery systems *Med. Eng. Phys.* **38** 2–10

[223] Lima-Tenório M K, Pineda E A G, Ahmad N M, Fessi H and Elaissari A 2015 Magnetic nanoparticles: *in vivo* cancer diagnosis and therapy *Int. J. Pharm.* **493** 313–27

[224] Truong N P, Whittaker M R, Mak C W and Davis T P 2015 The importance of nanoparticle shape in cancer drug delivery *Expert Opin. Drug Deliv.* **12** 129–42

[225] Müller K, Fedosov D A and Gompper G 2014 Margination of micro-and nano-particles in blood flow and its effect on drug delivery *Sci. Rep.* **4** 4871

[226] Brigger I, Dubernet C and Couvreur P 2002 Nanoparticles in cancer therapy and diagnosis *Adv. Drug Deliv. Rev.* **54** 631–51

[227] Hembury M *et al* 2015 Gold–silica quantum rattles for multimodal imaging and therapy *Proc. Natl Acad. Sci. USA* **112** 1959–64

[228] Fullstone G, Nyberg S, Tian X and Battaglia G 2016 Chapter two From the blood to the central nervous system: a nanoparticle's journey through the blood–brain barrier by transcytosis *Int. Rev. Neurobiol.* **130** 41–72

[229] Saraiva C, Praça C, Ferreira R, Santos T, Ferreira L and Bernardino L 2016 Nanoparticle-mediated brain drug delivery: overcoming blood–brain barrier to treat neurodegenerative diseases *J. Control. Release* **235** 34–47

[230] Richtering W, Potemkin I I, Rudov A A, Sellge G and Trautwein C 2016 Could multiresponsive hollow shell–shell nanocontainers offer an improved strategy for drug delivery? *Nanomedicine* **11** 2879–83

[231] Santoro F, Dasgupta S, Schnitker J, Auth T, Neumann E, Panaitov G, Gompper G and Offenh A 2014 Interfacing electrogenic cells with 3d nanoelectrodes: position, shape and size matter *ACS Nano* **8** 6713–23

[232] Blau A 2013 Cell adhesion promotion strategies for signal transduction enhancement in microelectrode array *in vitro* electrophysiology: an introductory overview and critical discussion *Curr. Opin. Colloid Interface Sci.* **18** 481–92

[233] Ojovan S M, Rabieh N, Shmoel N, Erez H, Maydan E, Cohen A and Spira M E 2015 A feasibility study of multi-site, intracellular recordings from mammalian neurons by extracellular gold mushroom-shaped microelectrodes *Sci. Rep.* **5** 14100

[234] Anderson Jr G W and Smith J F 1987 Immunoelectron microscopy of rift valley fever viral morphogenesis in primary rat hepatocytes *Virology* **161** 91–100

[235] Cureton D K, Massol R H, Whelan S P and Kirchhausen T 2010 The length of vesicular stomatitis virus particles dictates a need for actin assembly during clathrin-dependent endocytosis *PLoS Pathog.* **6** e1001127

[236] Herant M, Heinrich V and Dembo M 2006 Mechanics of neutrophil phagocytosis: experiments and quantitative models *J. Cell Sci.* **119** 1903–13

[237] Richards D M and Endres R G 2014 The mechanism of phagocytosis: two stages of engulfment *Biophys. J.* **107** 1542–53

[238] Champion J A and Mitragotri S 2006 Role of target geometry in phagocytosis *Proc. Natl Acad. Sci. USA* **103** 4930–4

[239] Richards D M and Endres R G 2016 Target shape dependence in a simple model of receptor-mediated endocytosis and phagocytosis *Proc. Natl Acad. Sci. USA* **113** 6113–8

[240] Tollis S, Dart A E, Tzircotis G and Endres R G 2010 The zipper mechanism in phagocytosis: energetic requirements and variability in phagocytic cup shape *BMC Syst. Biol.* **4** 149

[241] Masters T A, Pontes B, Viasnoff V, Li Y and Gauthier N C 2013 Plasma membrane tension orchestrates membrane trafficking, cytoskeletal remodeling and biochemical signaling during phagocytosis *Proc. Natl Acad. Sci. USA* **110** 11875–80

[242] Joshi D, Bargteil D, Caciagli A, Burelbach J, Xing Z, Nunes A S, Pinto D E, Araújo N A, Bruijc J and Eiser E 2016 Kinetic control of the coverage of oil droplets

by dna-functionalised colloids *Sci. Adv.* **2** e1600881

[243] Rose S, Prevoteau A, Elzière P, Hourdet D, Marcellan A and Leibler L 2014 Nanoparticle solutions as adhesives for gels and biological tissues *Nature* **505** 382–5

[244] Saunders B R and Vincent B 1999 Microgel particles as model colloids: theory, properties and applications *Adv. Colloid Interface Sci.* **80** 1–25

[245] Mehrabian H, Harting J and Snoeijer J H 2016 Soft particles at a fluid interface *Soft Matter* **12** 1062–73

[246] Scheidegger L, Fernandez-Rodriguez M A, Geisel K, Zanini M, Elnathan R, Richtering W and Isa L 2017 Compression and deposition of microgel monolayers from fluid interfaces: particle size effects on interface microstructure and nanolithography *Phys. Chem. Chem. Phys.* **19** 8671–80

[247] Yi X and Gao H 2017 Budding of an adhesive elastic particle out of a lipid vesicle *ACS Biomater. Sci. Eng.* (https://doi.org/10.1021/acsbiomaterials.6b00815)

[248] Yi X, Shi X and Gao H 2011 Cellular uptake of elastic nanoparticles *Phys. Rev. Lett.* **107** 098101

[249] Wang Z, Tiruppathi C, Minshall R D and Malik A B 2009 Size and dynamics of caveolae studied using nanoparticles in living endothelial cells *ACS Nano* **3** 4110

[250] Shang L, Gao P, Wang H, Popescu R, Gerthsen D and Nienhaus G U 2017 Protein-based fluorescent nanoparticles for super-resolution sted imaging of live cells *Chem. Sci.* **8** 2396–400

[251] van der Zwaag D, Vanparijs N, Wijnands S, De Rycke R, De Geest B G and Albertazzi L 2016 Super resolution imaging of nanoparticles cellular uptake and trafficking *ACS Appl. Mater. Interfaces* **8** 6391–9